TECHNISCHE
UNIVERSITÄT
DRESDEN

Leibniz Institute
for Solid State and
Materials Research
Dresden

Electronic correlations and nematicity in 122 and 1111 Fe-based superconductors

Dissertation
zur Erlangung des akademischen Grades
Doctor rerum naturalium
(Dr. rer. nat.)

vorgelegt der

Fakultät Mathematik und Naturwissenschaften
der Technischen Universität Dresden

von

Francesco Scaravaggi
geboren am 21. Juni 1988 in Crema, Italy

Eingereicht am 09.07.2021
Verteidigt am 15.12.2021

1. Gutachter: Prof. Dr. Bernd Büchner
2. Gutachter: Prof. Dr. Rüdiger Klingeler

Diese Dissertation wurde in der Zeit von August 2016 bis Januar 2021 am Institut für Festkörperforschung des Instituts für Festkörper- und Werkstoffforschung, Leibniz IFW Dresden in der Arbeitsgruppe von Dr. Anja Wolter-Giraud angefertigt.

Abstract

This work gives insight in some key aspects for the understanding of the origin of high-temperature superconductivity in the newly discovered class of iron-based materials. In particular, thermodynamic methods, such as SQUID magnetometry, specific heat and dilatometry were used, in order to (i) assess the evolution of electronic correlations in a series of transition metal substitutions of the well-known $BaFe_2As_2$ as a function of $3d$ band filling and (ii) to re-investigate the phase diagram of Co-doped LaFeAsO on single crystals, with particular interest in the interplay between the nematic/magnetic phase of the parent compound and superconductivity induced by in-plane electron doping.

In the first part of this work, the Sommerfeld coefficient (γ_{exp}) was extracted from the low temperature specific heat data and compared with the theoretical values obtained by band theory calculations (γ_{th}), in order to obtain the mass enhancement (m^*/m_b) in the series BaT_2As_2 (T = Cr, Mn, Fe, Co, Ni, Cu). The results clearly show an overall decrease of the electronic correlations while departing from the half-filled ($3d^5$) to the fully filled configuration ($3d^{10}$), thus suggesting a highly correlated $3d^5$ state. The evolution of electronic correlations as a function of $3d$ band filling for $n > 5$ is in agreement with previous theoretical calculations, underlining the importance of Hund's coupling (J_{H}) in describing the normal-state properties of iron-based superconductors. In addition, it was found that the decrease in m^*/m_b for $n > 5$ follows an increase of the crystal field splitting (Δ), determined by the progressive distortion of the As-T-As angle (α_{bond}) from the ideal tetrahedral environment. This study reveals a complex interplay between electronic correlations, band filling and crystal structure in determining the physical properties of 122 systems.

In the second part, the phase diagram of Co-doped LaFeAsO was re-investigated using single crystals by thermodynamic methods. From magnetic susceptibility studies we track the doping evolution of the antiferromagnetic phase, revealing a continuous decrease of T_{N} up to 5% Co doping. In order to study the evolution of the so-called nematic phase, the temperature dependence of the length changes along the a and b orthorhombic directions, $\Delta L/L_0$, was determined by high-resolution capacitance dilatometry. The results clearly show a gradual reduction of the orthorhombic distortion δ and of T_{S} with increasing Co content up to 4.5%, while it is completely suppressed for 7.5% Co. Bulk superconductivity with $T_{\mathrm{c}} = 10.5$ K was found in a small doping region around 6% Co content, while both T_{c} and the superconducting volume fraction rapidly drop in the neighbouring doping regime. Ultimately, no microscopic coexistence between the superconducting and magnetic phases can be assessed within our resolution limit, in sharp contrast with other iron-pnictide families, e.g., electron- and hole-doped $BaFe_2As_2$.

Contents

1. Introduction **1**

I. Theoretical Background 5

2. Thermodynamic properties **7**
- 2.1. Thermodynamic quantities 7
- 2.2. Low temperature contributions to C_p and α 9
- 2.3. Phase transitions 12
  - 2.3.1. Clausius-Clapeyron and Ehrenfest relations 13
  - 2.3.2. Landau theory of second-order phase transitions 14
- 2.4. Superconductivity 16
  - 2.4.1. BCS theory of superconductivity 16
  - 2.4.2. Unconventional superconductivity 18

II. Experimental methods 21

3. Thermodynamic probes **23**
- 3.1. SQUID magnetometry 23
  - 3.1.1. Experimental setup 23
  - 3.1.2. SQUID detection 25
- 3.2. Heat capacity 27
  - 3.2.1. Measurement principle 27
  - 3.2.2. Experimental setup 29
- 3.3. Capacitance dilatometry 30
  - 3.3.1. Measurement principle 31
  - 3.3.2. Background subtraction 32
  - 3.3.3. Experimental setup 34
  - 3.3.4. Pressure estimation 35

III. Thermodynamic properties of Iron-based superconductors 37

4. Iron-based superconductors 39
4.1. Introduction 39
4.2. Crystal and electronic structure 40
4.3. Electronic correlations in IBS 42
4.4. General phase diagrams of IBSs 43

5. Electronic correlations and structural changes in the series BaT_2As$_2$ (T = Cr, Mn, Fe, Co, Ni, Cu) 47
5.1. Electronic correlations in multiorbital systems (Hund's metals) 47
5.2. Previous studies on 122 FeAs compounds 53
5.3. The substitution series BaT_2As$_2$ (T = Cr, Mn, Fe, Co, Ni, Cu) 58
  5.3.1. Structural properties 59
  5.3.2. Magnetic properties 59
  5.3.3. Optical conductivity 63
  5.3.4. Specific heat capacity 65
  5.3.5. Quasiparticle mass enhancement 69
  5.3.6. Discussion 71

6. Revisiting the phase diagram of electron doped LaFeAsO single crystals 73
6.1. The nematic phase in Fe-based superconductors 73
6.2. The phase diagram of 1111 systems 78
6.3. Revisiting the phase diagram of LaFe$_{1-x}$Co$_x$AsO on single crystals 82
  6.3.1. LaFe$_{1-x}$Co$_x$AsO single crystals 83
  6.3.2. Detwinning of single crystals 84
  6.3.3. Long range magnetic ordering (T_N) and superconductivity (T_c) . . . 85
  6.3.4. Orthorhombic lattice distortion (T_S) 89
  6.3.5. Pressure dependence of T_S and T_N 91
  6.3.6. Phase diagram 94

7. Summary 99

Bibliography 115

1. Introduction

Despite its discovery by H. Kammerlingh Onnes (1) dating back to more than one century ago (1911), superconductivity is still regarded as one of the major research treads as well as key technological challenges in modern days. In fact, the importance of this class of materials spans from high magnetic field generation, through persistent self-sustaining currents, which are widely used in research on quantum magnetism and are a key element of many designs for the next generation power plants based on nuclear fusion (as the ITER project (2)), to their implementation in electronic devices, such as high resolution magnetic field sensors, as well as new generation qubits, as one of the prominent architectures used for quantum computation. (3) The main technological challenge for large scale applications is to find materials, which could preserve the superconducting properties as close as possible to room temperature, thus minimizing the energy cost for cooling, which represents a limiting factor for many technologies. In this context, while the transition temperatures (T_c) of conventional superconductors, whose behavior is well predicted by the BCS theory, are intrinsically limited to low energy scales, the so-called unconventional superconductors can reach much higher critical temperatures. In recent years, the highest critical temperatures at athmospheric pressure were probed in CuO-based materials (i.e. cuprates), yielding a maximum T_c of 135 K. (4) Notably, temperatures as high as $T_\mathrm{c} > 200\ K$ could recently be reached in sulfur hydride compounds by the application of very high pressures ($p > 200\ GPa$). (5) The improvement of T_c requires a precise fundamental understanding of the mechanism behind unconventional superconductivity, for which a comprehensive theoretical description is still not unanimously established within the scientific community.

The discovery of superconductivity in Fe-based materials by Kamihara *et al.* in 2008 on F-doped LaFeAsO at $T_\mathrm{c} = 26$ K renewed the interest in this field. These compounds, similarly to cuprates, are quasi 2D materials, all characterized by the presence of Fe-pnictogen/chalcogen (Fe-Pn/Ch) layers, but the variety of newly discovered compositions and combinations of doping elements for this class of materials suggested the possibility to find a common origin for high-temperature superconductivity. In order to understand the basic mechanism for unconventional Cooper pairing, it is of primary importance to study, not only the superconducting state, but also the physical properties of the neighboring phases as well as their interplay with superconductivity. For Fe-based materials, superconductivity occurs in close proximity to a spin density wave phase (SDW) as well as to a so-called electronic nematic phase, characterized by the concomitant presence of different anisotropic quantities in the system that break the C_4 symmetry in the Fe-Pn/Ch planes, which generally need to be suppressed by electron or hole doping in order to observe bulk superconductivity. The competitive or cooperative nature of such phases as well as the main driving mechanism of nematicity are still open questions in the field for many classes of Fe-based materials. In particular, the driving force of the nematic order is widely regarded as the most probable bonding interaction for Cooper pairing (i.e. mediated by spin or orbital fluctuations). A common feature with other classes of unconventional superconductors is the presence of a non-negligible degree of electronic correlations and it is regarded as one of the key features for high-temperature superconductivity. In Fe-based compounds, unlike insulating cuprates, the Fermi surface is characterized by the presence of multiple electron- and hole-like bands crossing the Fermi energy, therefore the Coulomb potential (U), which tends to drive the system to a Mott-insulating state, is not enough to correctly describe the electronic correlations in these systems. Instead, Hund's coupling (J_H) between electrons in different bands has to be taken into account. The interplay between U and J_H ultimately determines the physical properties of these compounds and can lead to the selective localization of some bands, while others maintain their itinerant character, i.e. give rise to an orbital selective Mott-transition (OSMT). Therefore, the individual filling of the Fe-3d bands plays an important role in determining the electronic correlations in the system.

In the present PhD dissertation, the two key aspects in the field of Fe-based superconductors, presented in the last paragraph, are assessed with respect to different Fe-pnictide families. In particular, the first part of the work examines the evolution of electronic correlations in such multiorbital systems as a function of 3d band filling in 122 compounds, i.e. named after their stoichiometry; the analysis of the data and the comparison with structural parameters suggest that a complex interplay between Coulomb potential, Hund's coupling and crystal field splitting ultimately determines the physical properties of these systems. The second part is focused on the study of the neighbouring phases precursing/competing with superconductivity in electron-doped LaFeAsO systems, with particular attention to the nature of the interplay between the nematic-magnetic and the superconducting phases. The work is structured as follows.

In Part I, selected basic theoretical concepts on thermodynamic properties, phase transition and superconductivity are introduced and discussed. The chapter deals with the definition and explanation of thermodynamic quantities and relations that will prove useful for the general understanding of the topics and experimental results presented within this dissertation.

The main experimental methods and techniques used for this work are introduced in Part II. The chapter introduces the measurement principles and experimental setup of SQUID magnetometry, heat capacity measurements through the relaxation method and capacitance dilatometry. In particular, for the thermal expansion measurements performed in this work, a particular configuration was used in order to lift the structural twinning of the samples, through the application of a uniaxial strain, and assess the length changes in different crystallographic directions within the *ab* plane.

In Part III, the experimental results of this thesis are presented and discussed in the broader framework of high-temperature superconductivity. At first, an introduction to iron-based superconductors, their general structural features and their phase diagrams, with particular attention to the important parameters in order to achieve the superconducting state is presented in Chapter 4. Chapter 5 discusses the evolution of electronic correlations in the series $\mathrm{Ba}T_2\mathrm{As}_2$ (T = Cr, Mn, Fe, Co, Ni, Cu) of single crystals, i.e. a series of stoichiometric compounds with a large variety of $3d$ states. The results are compared with the relevant structural parameters for the different compositions and are discussed within the general framework of Hund's metals theory, for which the filling of the $3d$ bands can be used as a tuning parameter together with structural modifications within the T-As planes. In Chapter 6, the phase diagram of LaFeAsO as a function of Co-doping was investigated on single crystals by means of thermodynamic methods, which allow to probe magnetic, structural and superconducting transition temperatures as a function of temperature and doping. Differently from previous studies on the same compound, the use of sizable faceted single crystals allowed to assess anisotropic quantities within the *ab* plane, characterizing the nematic phase in IBSs. In particular, thermal expansion measurements were used to probe the small structural distortion (δ) in different crystallographic directions, which signals the onset of the nematic phase in Fe-based superconductors. In order to get better insight in the behavior of this material, the results are then compared with other bulk as well as microscopic techniques and the phase diagram of $\mathrm{LaFe}_{1-x}\mathrm{Co}_x\mathrm{AsO}$ is constructed and discussed with respect to other Fe-based materials, such as 122 and 11 compounds.

Finally, the main results and conclusions of this thesis are summarized and an outlook for future studies is presented in Chapter 7.

Part I.

Theoretical Background

2. Thermodynamic properties

This Chapter will briefly introduce some fundamental theoretical concepts that are useful for the understanding of this PhD thesis. In particular, general thermodynamic quantities as well as the main relations between them will be defined in section 2.1. The main contributions to the thermal expansion coefficient and the heat capacity of a crystalline material (thermodynamic probes widely used throughout this work) are introduced and briefly discussed in sections 2.2 and 2.3, as well as the thermodynamic classification of phase transitions and pressure dependence of the transition temperatures. A brief introduction to the Landau theory for second-order phase transitions -important for the thermodynamic description of the nematic phase of iron-based superconductors-, is also included. In Section 2.4, conventional superconductors will be introduced, as well as a concise microscopic description through BCS theory. The main aspects of unconventional Cooper pairing will be discussed, particularly referring to the most studied cuprate materials.

2.1. Thermodynamic quantities

A thermodynamic approach allows to assess relevant macroscopic physical quantities, regardless the specific microscopic configuration of a system. In order to derive such quantities it is necessary to know the external conditions of the system in terms of the state variables, e.g. temperature (T), pressure (P), entropy (S). The functional forms relating such variables to each other are given by the thermodynamic potentials. The choice of the relevant potential is taken based on the external conditions of the system and its knowledge allows to derive all the relevant thermodynamic quantities. In fact, the free energy (F) describes a thermodynamic system as a function of the temperature (T) and the volume (V) and it can be defined in its differential form as

$$dF = -SdT - pdV \tag{2.1.1}$$

where S is the entropy and p is the pressure applied to the system. The Gibbs free energy (G) describes the system as a function of pressure and temperature (T) and can be defined as

$$dG = -SdT + Vdp. \tag{2.1.2}$$

The state variables of the system can be derived from the thermodynamic potentials. In particular, following from the Gibbs potential differential expression, S and V can be defined as

$$S = -\left.\frac{\partial G}{\partial T}\right|_p \tag{2.1.3}$$

$$V = \left.\frac{\partial G}{\partial p}\right|_T. \tag{2.1.4}$$

On the other hand, the specific heat of a thermodynamic system is defined as the quantity of heat necessary for a sample to increase its temperature by one unit, according to the general formula

$$C = \frac{\delta Q}{dT} \tag{2.1.5}$$

where δQ is the infinitesimal heat quantity correlated to the temperature increase dT. The thermodynamic expression of specific heat strongly differs depending on the process by which the heat is provided to the system. Therefore, we can define specific heat quantities at constant volume (C_{V}) or at constant pressure (C_{p}):

$$C_{\mathrm{V}} = \left.\frac{\delta Q}{dT}\right|_V = T\left.\frac{\partial S}{\partial T}\right|_V = -T\left.\frac{\partial^2 F}{\partial T^2}\right|_V \tag{2.1.6}$$

$$C_{\mathrm{p}} = \left.\frac{\delta Q}{dT}\right|_p = T\left.\frac{\partial S}{\partial T}\right|_p = -T\left.\frac{\partial^2 G}{\partial T^2}\right|_p. \tag{2.1.7}$$

From these expressions, it can be noticed that the specific heat is proportional to the temperature derivative (at constant volume or pressure) of the entropy of the system. In our case, the measurement technique used in this work probes the specific heat at constant pressure (C_{p}). (see section 3.2.1)

In a similar way, the change in the volume of a solid sample as a function of temperature can be derived from the Gibbs potential. Therefore, the linear coefficient of volume thermal expansion (α_{V}) can be expressed as

$$\alpha_{\mathrm{V}} = \frac{1}{V}\left.\frac{\partial V}{\partial T}\right|_p = -\frac{1}{V}\left.\frac{\partial S}{\partial p}\right|_T = \frac{1}{V}\frac{\partial^2 G}{\partial p \partial T} \tag{2.1.8}$$

where V is the volume of the solid. The volume thermal expansion is proportional to the pressure derivative of the entropy of the system, in a similar way as the specific heat is related to the entropy variation with temperature. It is important to notice that the thermal expansion can be expressed in a single direction (in our case represented by one of the crystallographic axes of a crystalline material) as

$$\alpha_\mathrm{i} = \frac{1}{L_\mathrm{i}} \frac{\partial L_\mathrm{i}}{\partial T} \qquad (i = x, y, z) \tag{2.1.9}$$

where L_i is the length of the sample in the i direction.

For systems in which the effects of an applied magnetic field are relevant, the Gibbs free energy can be written in the form

$$dG = -SdT + Vdp + \mu_0 VMdH \tag{2.1.10}$$

where H represents the external applied magnetic field, μ_0 the magnetic permeability of vacuum and M the magnetization per unit volume of the system. In analogy with equations 2.1.3 and 2.1.4, the magnetization for unit volume can be written as

$$M_\mathrm{i} = \frac{1}{\mu_0 V} \frac{\partial G}{\partial H_i}\bigg|_{p,T} \qquad (i = x, y, z). \tag{2.1.11}$$

Furthermore, the magnetic susceptibility describes the linear response function of the material to an applied external magnetic field and is described by the tensor

$$\chi_\mathrm{i,j} = \frac{\partial M_\mathrm{i}}{\partial H_\mathrm{j}}\bigg|_{p,T} = \frac{1}{\mu_0 V} \frac{\partial^2 G}{\partial H_\mathrm{j}^2}\bigg|_{p,T} \qquad (i,j = x, y, z). \tag{2.1.12}$$

where the indices i and j account for magnetization measured in a different direction with respect to the applied magnetic field. In the measurement setup used for this work (see Section 3.1.1), the magnetic susceptibility is always measured in the same direction of the applied magnetic field, i.e. considering the diagonal terms of the susceptibility tensor only.

In summary, all the state variables can be expressed as first derivatives of the thermodynamic potentials, while the response functions are given by their second derivatives. This is particularly important in the detection of phase transitions, as explained in Section 2.3.

2.2. Low temperature contributions to C_p and α

To a first approximation, the thermodynamic potentials can be generally written as the sum of distinct components (12), e.g. in the case of F it can be expressed as

$$F = \sum_{k=1}^{n} F_k \tag{2.2.1}$$

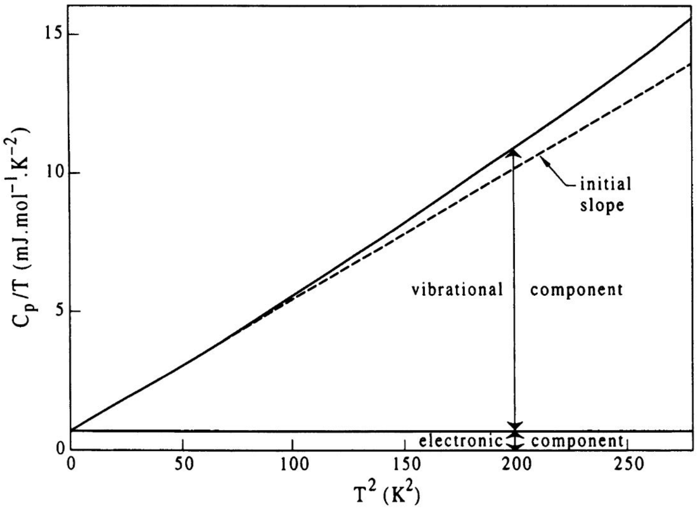

Figure 2.2.1.: Schematic representation of the different C_p components as a function of temperature. The dashed line represents the low temperature linear fit of $C_\mathrm{p} \sim \gamma_\mathrm{n} + \beta\, T^2$, where the intercept is the Sommerfeld coefficient (γ_n). As typical of many materials the experimental fit deviates from the linear approximation around $T \sim 10$ K. Taken from Ref. (12).

where the F_k terms represent the contributions to the free energy from different parts of the system. In the case of solid state systems, it can be conveniently expressed as

$$F = F_\mathrm{el} + F_\mathrm{ph} + ... \qquad (2.2.2)$$

where F_el and F_ph are the free energies associated to the free electron and the phononic terms, respectively. From equation 2.2.2 directly follows that all the derivatives of the thermodynamic potential can be written in the same way. In particular, the entropy of the sample is given by

$$S = S_\mathrm{el} + S_\mathrm{ph} + S_\mathrm{mag} + ... \qquad (2.2.3)$$

and by considering equations 2.1.7 and 2.1.8 it gives

$$C_p = C_\mathrm{el} + C_\mathrm{ph} + C_\mathrm{mag} + ... \qquad (2.2.4)$$

$$\alpha = \alpha_\mathrm{el} + \alpha_\mathrm{ph} + \alpha_\mathrm{mag} + ... \qquad (2.2.5)$$

that imply that, for real materials, the different contributions to C_p and α can be modeled and disentangled from each other from the total signal of the sample. In addition to the electronic and phononic term, other phenomena can contribute to these quantities, such as e.g. magnetic or structural transitions. Such anomalies can be isolated and analyzed by carefully subtracting the background signal (C_el+C_ph).

In particular, as shown in Fig. 2.2.1, the electronic and phononic components of specific heat can be distinguished by considering the low temperature range. The electronic specific heat contribution in a crystalline solid can be derived from the Drude model as

$$C_\mathrm{el} = \gamma_0 T = \frac{\pi^2}{3}\rho(E_F)k_B^2 T \tag{2.2.6}$$

where γ_0 is the Sommerfeld coefficient and k_B the Boltzmann constant. As it is clear from the equation 2.2.6, the electronic specific heat is linear in temperature and the Sommerfeld coefficient is proportional to the density of states at the Fermi level (E_F), $\rho(E_F)$, and, therefore, C_el represents the contribution to the specific heat given by the conduction electrons in a crystal. The Sommerfeld coefficient can also be expressed as a function of the electron mass as

$$\gamma_0 = \frac{k_B^2}{3\hbar^2} V k_F m_0 \tag{2.2.7}$$

where m_0 is the mass of the free electrons, k_F the Fermi velocity and V the volume of the sample. In the general case of a real material, the measured Sommerfeld coefficient (γ_n) is proportional to the effective mass of the electron in the lattice. The mass enhancement can be estimated by considering the ratio

$$\frac{\gamma_\mathrm{n}}{\gamma_0} = \frac{m^*}{m_0}. \tag{2.2.8}$$

which represents the mass enhancement above the value obtained from the free electron approximation. This ratio can differ significantly from $\frac{m^*}{m_0} \sim 1$, speaking for the presence of electronic correlations in the system. This relation will be widely used in Chapter 5 to estimate the degree of correlations in different transition metal-pnictides.

On the other hand, the energy contribution coming from the lattice vibrations of a material over a broad temperature range is successfully described by the Debye model (14), in which the relevant (quantized) wavelengths in the system are approximated as a continuum and, since the considered momentum range is within the Brillouin zone ($-\pi/a < k < \pi/a$), the model is restricted to the frequencies $\omega < \omega_\mathrm{D}$, where ω_D is called Debye frequency. Therefore, by defining the dimensionless variable $x = \hbar\omega/k_\mathrm{B}T$, the lattice specific heat can be calculated as

$$C_\mathrm{ph} = 9Rs\left(\frac{T}{\Theta_\mathrm{D}}\right)^3 \int_0^{x_\mathrm{D}} \frac{x^4 e^x}{(e^x-1)^2}dx \tag{2.2.9}$$

where $x_\mathrm{D} = \hbar\omega_\mathrm{D}/k_\mathrm{B}T$ is the x value associated with the Debye frequency ω_D and $\Theta_\mathrm{D} = \hbar\omega_\mathrm{D}/k_\mathrm{B}$ is the Debye temperature. In this context, the Debye temperature represents the energy scale within which this model is valid and above which the classical

Dulong-Petit description ($C_{\mathrm{ph}} = 3Rs$, where R is the gas constant and s the number of atoms per unit cell) can be adopted. At low temperature ($T \ll \Theta_{\mathrm{D}}$), the equation 2.2.9 can be approximated as

$$C_{\mathrm{ph}} = \frac{12\pi^4}{5}\left(\frac{Rs}{\Theta_{\mathrm{D}}^3}\right)T^3 = \beta T^3. \tag{2.2.10}$$

where β is the coefficient of the low-temperature phononic term. It should be considered that the Debye model with one Θ_{D} in many materials is not able to properly approximate the specific heat over the entire temperature range, since the density of phonon modes is not exactly proportional to ω^2. Therefore, a correct modeling of the phononic contribution often requires multiple components with different Θ_{D} values. In the experimental practice, a more accurate fitting of the experimental data is given by considering higher order odd terms, so the low temperature phononic specific heat becomes

$$C_{\mathrm{ph}} = \beta T^3 + \delta T^5 + \epsilon T^7 + h.o. \tag{2.2.11}$$

In order to extract the small electronic specific heat contribution (γ_{n}) from experimental data, the low-temperature region should be considered, for which the electronic contribution becomes comparable to the phononic one as shown in Fig. 2.2.1. Therefore, the total specific heat of the material in the low-temperature limit can be approximated as

$$\frac{C_{\mathrm{p}}}{T} = \gamma + \beta T^2 + \delta T^4 + h.o. \tag{2.2.12}$$

where γ and β can be extracted as the intercept and the slope of the linear component of $\frac{C_{\mathrm{p}}}{T}(T^2)$ (see Fig. 2.2.1). This procedure will be widely used in Chapter 5 in order to disentangle the different components of the experimental specific heat curves.

2.3. Phase transitions

Chapter 6 deals with the determination of the phase diagram of Co-doped La1111 systems, therefore it is important to give the thermodynamic classification of phase transitions. For all phase transitions, the Gibbs free energy (G) is continuous across the transition point, i.e. equal for both phases. Consequently, according to the classification proposed by Paul Ehrenfest in 1933, phase transitions are classified by the order of the first discontinuous derivative of the Gibbs free energy. Therefore, a phase transition is defined as n-th-order, when the $(n-1)$-th derivative of the thermodynamic potential is still continuous, while the n-th-order derivative has a jump. As discussed in section 2.1, thermodynamic response functions that can be directly measured through experiments (M, C_{p}, α), can be generally expressed as derivatives of the thermodynamic potentials.

In this context, a first-order phase transition is characterized by discontinuous first derivative of G, therefore state variables, e.g. S, V, present a jump at $T = T_\mathrm{c}$ and the response functions assume the shape of a δ-function. In particular, from the discontinuity of the entropy ΔS follows that a finite amount of heat δQ is released (or absorbed) at the transition temperature, according to the relation $\delta Q = TdS$, referred as the latent heat of a first-order transition. Second-order transitions are characterized by continuous first derivatives of the thermodynamic potentials, while the discontinuity can be seen in the second-order derivatives, such as C_p, α_V, α_i. They are often called λ-shaped transitions, referring to the shape of the peak-like anomaly that they induce in thermodynamic probes. Generally speaking, most of the observed transitions in nature are first-order, such as liquid to gas transitions or many structural transitions in solid state materials, while examples of second-order transitions can be found for magnetic or superconducting transitions.

2.3.1. Clausius-Clapeyron and Ehrenfest relations

As already mentioned, the continuity of the thermodynamic potential is granted across a phase transition happening at $T = T_\mathrm{c}$ between the phases 1 and 2. This condition for the Gibbs potential can be expressed as

$$\Delta G = G_1 - G_2 = 0 \tag{2.3.1}$$

and from equation 2.1.2 follows that

$$\Delta S dT_\mathrm{c} = \Delta V dp \tag{2.3.2}$$

such that, in the case of a first-order phase transition, ΔS and ΔV are expected to be different from zero, thus giving

$$\frac{dT_\mathrm{c}}{dp} = \frac{\Delta V}{\Delta S}. \tag{2.3.3}$$

Equation 2.3.3 is referred as the Clausius-Clapeyron relation, which allows to estimate the pressure dependence of transition temperatures in case of discontinuous phase transitions, where the volume and entropy changes associated with the transition can be derived from the thermal expansion coefficient and the heat capacity, respectively.

In the case of second-order phase transitions, the pressure dependence of the transition temperature can be related to the jumps in the derivatives of V and S, namely $\Delta\alpha$ and ΔC_p, according to the Ehrenfest relation, which can be derived from equations 2.1.7 and

2.1.8

$$\Delta\alpha_{\mathrm{V}} = \alpha_2 - \alpha_1 = \frac{1}{V}\left(\frac{\partial S_2}{\partial p} - \frac{\partial S_1}{\partial p}\right) = \frac{1}{V}\left(\frac{\partial S_2}{\partial T} - \frac{\partial S_1}{\partial T}\right)\frac{dT_{\mathrm{c}}}{dp} = \frac{1}{VT}\Delta C_p \frac{dT_{\mathrm{c}}}{dp} \tag{2.3.4}$$

which gives the expression for the pressure dependence as

$$\frac{dT_{\mathrm{c}}}{dp} = V_{\mathrm{m}} T_{\mathrm{c}} \frac{\Delta\alpha_{\mathrm{V}}}{\Delta C_p} \tag{2.3.5}$$

where V_{m} is the molar volume of the sample and $\Delta\alpha_{\mathrm{V}}$ is the change of the volume thermal expansion across the transition. From these equations, the uniaxial pressure dependence of a transition at $T = T_{\mathrm{c}}$ can be obtained, for first- and second-order transitions respectively, by

$$\frac{dT_{\mathrm{c}}}{dp_i} = \frac{\Delta L_i}{\Delta S} \tag{2.3.6}$$

and

$$\frac{dT_{\mathrm{c}}}{dp_i} = V_{\mathrm{m}} T_{\mathrm{c}} \frac{\Delta\alpha_i}{\Delta C_p} \tag{2.3.7}$$

where i is the crystallographic direction in which the uniaxial pressure is applied, while ΔL_i and $\Delta\alpha_i$ are the length change and the amplitude of the thermal expansion signal associated to the phase transition, respectively. In particular, equation 2.3.7 will be used to qualitatively estimate the pressure dependence of the magnetic transition temperature in LaFeAsO single crystals (see Chapter 6).

2.3.2. Landau theory of second-order phase transitions

The Landau theory of phase transitions represents a very general approach to describe phase transitions and make predictions on the behaviour of physical systems starting from symmetry considerations. This theory introduces the concept of order parameter ψ, which is a thermodynamic variable such that assumes a non-zero value in the ordered state, while it is equal to zero for other values of the independent variable, e.g. T, p, H (see Fig. 2.3.1 (a)). The approach is based on a mean-field approximation, in which fluctuations of the order parameter are neglected. The free energy of the system can be expressed by expanding its unknown functional form as a function of the order parameter as

$$F(\psi,T) = F_0 + \alpha|\psi|^2 + \frac{\beta}{2}|\psi|^4 + O(|\psi|^6) \tag{2.3.8}$$

where α and β are coefficients of the even powers of the order parameter and F_0 is the initial value of F that does not depend on ψ. Here, for simplicity, F is written as a

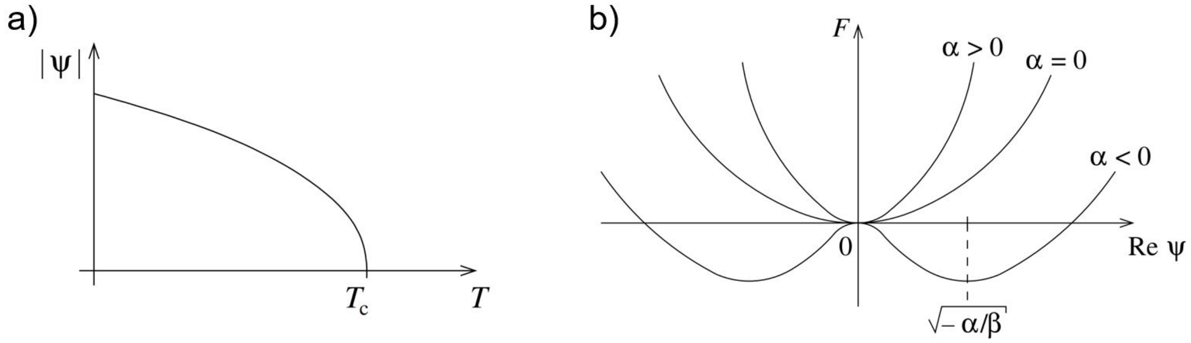

Figure 2.3.1.: (a) Temperature dependence of the order parameter of the Landau theory $|\psi|$ with transition temperature $T = T_c$. (b) Free energy (F) as a function of the real part of the order parameter. The graph distinguishes between different values of the parameter α, from which it is clearly seen that F has minima for $|\psi| \neq 0$ only if $\alpha < 0$. Taken from Ref. (15).

function of temperature and other possible variables, such as pressure and magnetic field, are not considered. The order parameter is considered in its absolute value $|\psi|$ in order to guarantee that F is a real function, while only even powers of ψ are utilized in order to grant their differentiability for any ψ values. By minimizing the Free energy with respect to the order parameter as

$$\frac{\partial F}{\partial \psi} = 2\alpha|\psi| + 2\beta|\psi|^3 = 0 \tag{2.3.9}$$

the following solutions are obtained

$$\psi = \left(0, \pm\sqrt{-\frac{\alpha}{\beta}}\right). \tag{2.3.10}$$

Therefore, in order to obtain a finite value of ψ, the coefficients should satisfy the condition $\frac{\alpha}{\beta} < 0$. The condition $\beta > 0$ is imposed in order to stabilize the potential F. Fig. 2.3.1 (b) shows the evolution of the Free energy as a function of ψ for different values of the parameter α. It is clear that a minimum of F for a finite value of the order parameter is only possible for $\alpha < 0$, while $\alpha \geq 0$ only allows $\psi = 0$. According to the aforementioned conditions α can be written as

$$\alpha = \alpha_0(T - T_c) \tag{2.3.11}$$

with $\alpha_0 > 0$. Thus, the order parameter for $T < T_c$ can be written as

$$|\psi| = \sqrt{-\frac{\alpha_0(T - T_c)}{\beta}} = \sqrt{\frac{\alpha_0}{\beta}}\sqrt{T - T_c}. \tag{2.3.12}$$

It is worth to notice that this expression has the same temperature dependence as predicted by mean field theory.

2.4. Superconductivity

Superconductivity is a collective quantum phenomenon of matter that results in a number of peculiar physical properties at the macroscopic scale. The superconducting phase can be achieved when the material is driven below a certain critical temperature (T_c). It is mainly characterized by a negligible value of electrical resistivity ($\rho \approx 0$), in which the charges are transported without scattering throughout the material. Another important property of the superconducting state is the Meissner-Ochsenfeld effect, i.e. the expulsion of the magnetic flux ($\mathbf{B}$) from the material, also referred as perfect diamagnetism, described as $\chi = \frac{dM}{dH} = -1$. Superconducting materials are classified based on their magnetic behaviour into type I and type II materials, as shown in Fig. 2.4.1. In fact, for type I superconductors the ($\mathbf{B}$) field inside the material is constant and equal to zero until a certain critical magnetic field (H_c) is exceeded and superconductivity is lost. In consequence, also when a critical current value (I_c) is exceeded the superconducting state is disrupted and the material behaves like a normal metal. For many materials, called type II superconductors, the condition of perfect diamagnetism is maintained below the critical lower critical field (H_c1), while, by further increasing the field, the magnetic flux progressively penetrates into the material ($\mathbf{B} \neq 0$) until superconductivity is fully suppressed by the upper critical field (H_c2). The phase for $H_\mathrm{c1} < H < H_\mathrm{c2}$ is called mixed phase and it is characterized by the penetration of the magnetic field in the form of vortices of circulating supercurrent around a core, which then behaves like a normal metal and allows a finite magnetic flux. This phenomenon was explained by A. Abrikosov, finding that the vortices form a regular lattice within the material and the flux contained in each of the vortices assumes discrete values given by $\Phi_0 = \frac{h}{2e}$.

2.4.1. BCS theory of superconductivity

The first microscopic theory of superconductivity was formulated in 1957 by J. Bardeen, L. N. Cooper and J. R. Schrieffer under the name of BCS theory after their initials. (16) This theory was able to describe the behavior of conventional superconductors, thus fixing important key concepts for these materials. In fact, the BCS theory came to the result that the interaction potential (V_eff) between electrons in a crystalline material can become attractive. This counterintuitive result is due to the coupling between the electrons and the phonons in the lattice, whose interaction, for pairs of electrons in proximity to the

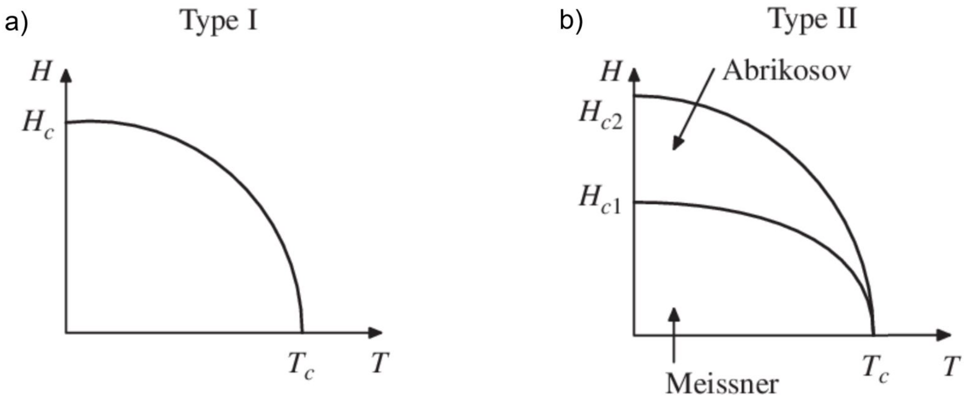

Figure 2.4.1.: $H - T$ phase diagram of a type I (a) and type II (b) superconductor. For type II superconductors the different phases are highlighted as the mixed phase (Abrikosov) for $H_{\text{c}1} < H < H_{\text{c}2}$ and the Meissner phase for $H < H_{\text{c}1}$. Taken from Ref. (10).

Fermi level, can give rise to bound states, that go under the name of Cooper pairs. The energy necessary to break a Cooper pair is found to be equal to 2Δ, which corresponds to the energy gap that opens up in the superconducting state for $T < T_{\text{c}}$.

The emergence of an attractive term can be understood by considering that a single electron, by moving in a metallic system, is able to attract the positively charged ions of the lattice, thus creating an attracting potential for the other electrons within the Fermi sea, therefore effectively coupling the electronic system with the crystal lattice.

The energy of the interacting electron system can be modeled by the general BCS Hamiltonian

$$\hat{H} = \sum_{\mathbf{k},\sigma} \epsilon_{\mathbf{k}} c^{\dagger}_{\mathbf{k},\sigma} c_{\mathbf{k},\sigma} + V_{\text{eff}} \sum_{\mathbf{k},\mathbf{k}'} c^{\dagger}_{\mathbf{k},\uparrow} c^{\dagger}_{-\mathbf{k},\downarrow} c_{-\mathbf{k}',\downarrow} c_{\mathbf{k}',\uparrow} \tag{2.4.1}$$

where $c^{\dagger}_{\mathbf{k},\sigma}$ and $c_{\mathbf{k},\sigma}$ are the creation and annihilation operators, respectively, associated with precise values of moment ($\mathbf{k}$) and spin (σ). In this formulation, equation 2.4.1 is composed by a first term accounting for the kinetic energy ($\epsilon_{\mathbf{k}}$) of the conduction electrons, while the second term, that is proportional to the electron-phonon interaction potential (V_{eff}), models the attractive interaction responsible for the formation of the Cooper pairs. The eigenvectors related to this Hamiltonian can be found as

$$|u_{\mathbf{k}}|^2 = \frac{1}{2}\left(1 + \frac{\epsilon_{\mathbf{k}} - \mu}{E_{\mathbf{k}}}\right) \quad ; \quad |v_{\mathbf{k}}|^2 = \frac{1}{2}\left(1 - \frac{\epsilon_{\mathbf{k}} - \mu}{E_{\mathbf{k}}}\right) \tag{2.4.2}$$

and the eigenvalues of the Hamiltonian can then be obtained as a dispersion relation as a function of $\mathbf{k}$

$$E_{\mathbf{k}} = \sqrt{(\epsilon_{\mathbf{k}} - \mu)^2 + |\Delta|^2} \tag{2.4.3}$$

where the single electron energy is expressed as relative to the chemical potential (μ) and the term $|\Delta|$ represents the energy gap that opens up below T_c, which determines the energy scale of the superconducting state. The explicit expression for the gap parameter can be derived as

$$|\Delta| = 2\hbar\omega_{\mathrm{D}} e^{-1/\lambda} \tag{2.4.4}$$

where ω_{D} is the Debye frequency and λ is the electron-phonon coupling constant. The λ constant is defined as

$$\lambda = |g_{\mathrm{eff}}|^2 \rho(E_{\mathrm{F}}) \tag{2.4.5}$$

which is proportional to the effective potential ($V_{\mathrm{eff}} \propto |g_{\mathrm{eff}}|^2$) and the density of states at the Fermi level, $\rho(E_{\mathrm{F}})$. As mentioned above, the value of the superconducting energy gap represents the energy associated to the bound state and therefore it can be related to the thermal energy necessary to disrupt this phase, which in turn relates to the critical temperature (T_{c}), according to the relation

$$\frac{2\Delta(0)}{k_{\mathrm{B}}T_{\mathrm{c}}} = 3.52 \tag{2.4.6}$$

where $\Delta(0)$ represents the value of the superconducting gap at zero temperature.

2.4.2. Unconventional superconductivity

Unconventional superconductors are defined as materials in which Cooper pairing occurs at a different symmetry than the ground state found for BCS theory. In fact, BCS theory extracts a single value of the superconducting gap Δ (see equation 2.4.4), but it can be more generally written as a function of $\mathbf{k}$, as $\Delta_{\mathbf{k}}$, where $\Delta_{\mathrm{k}} = \Delta_0$ represents the case of isotropic gap amplitude in the $\mathbf{k}$-space, referred as s-wave pairing, in full analogy with the symmetry of the spherical harmonic functions for atomic orbitals. Accordingly, other symmetries of the superconducting gap are possible, thus giving rise to more exotic pairing *p*- or *d*-wave superconductors. Examples of such pairing symmetries are Sr_2RuO_4 and $YBa_2Cu_3O_7$, respectively. In this context, the isotropic *s*-wave pairing is found in most cases for phonon-mediated superconductors (as described in the previous section). In order to establish the pairing symmetry, it is important to consider the band structure in proximity to the Fermi level. To illustrate this, Fig. 2.4.2 shows the Fermi surfaces for two of the most studied classes of high-temperature superconductors.

One important class of unconventional superconductors is given by CuO-based materials (i.e. cuprates), for which the occurrence of a $d_{x^2-y^2}$ pairing symmetry was established by many theoretical and experimental works. Such pairing allows the presence of zeroes (i.e.

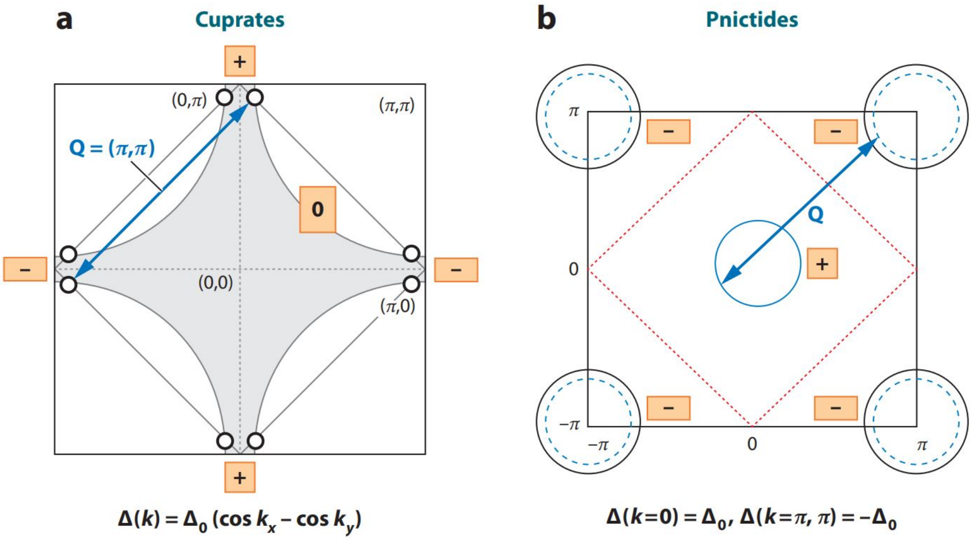

Figure 2.4.2.: Pairing state symmetries of Cooper pairs in the Fermi surface for (a) cuprate and (b) iron-based superconductors. In both graphs, the shown pairing refers to the spin-fluctuation based pairing, which will give a *d*-wave symmetry for cuprates and a nodeless s^{+-} symmetry for IBSs. Taken from Ref. (18).

nodes) in the superconducting gap function Δ_k. In cuprates, superconductivity emerges in close proximity to a Mott-insulating phase, characterized by a localized antiferromagnetic ground state. Therefore, spin fluctuations are considered as a prominent candidate for the pairing mechanism in this class of compounds. Such spin mediated interaction is described by screened Coulomb electron-electron potential, which then gives a positive (i.e. repulsive) term in the Hamiltonian. In order to have a stable bound state, the gap must change sign between different points of the Fermi surface and this condition is achieved between **k** and **k'** = **k** + **Q**, where **Q** = (π,π) is the momentum connected with the spin-fluctuations pairing interaction (see Fig. 2.4.2 (a)). (17)

Another prominent class of materials is composed by Fe-based superconductors (IBS), for which the Fermi surface is shown in Fig. 2.4.2 (b). IBSs are characterized by multiple bands crossing the Fermi energy, composed by electron and hole pockets located at the center (Γ-point) and at the corners of the Brillouin zone. A common feature between many IBS and cuprate compounds is the proximity between superconductivity and an antiferromagnetic phase, which would lead to think of a common origin of the superconducting pairing. In this case though, such phase is more complex and involves different ordering phenomena closely intertwined with each other in the so-called nematic phase and, although different theories are present, the pairing mechanism in this class of materials is still not established. The main considered scenarios are based on the fluctuations of the most prominent ordering of the nematic phase, i.e. spin- or orbital-fluctuations, as pairing glue for superconductivity. In particular, for the spin-nematic scenario, spin fluctuations are enhanced for an interaction potential $V_{eff} > 0$, therefore in order to have an attractive interaction, $\Delta_{\mathbf{k}}$ must change sign upon the momentum exchange, $\mathbf{Q} = (\pi,0)$ or $\mathbf{Q} = (0,\pi)$, thus reflecting the symmetry of the antiferromagnetic long range ordering. In this case, the most probable configuration corresponds to a s^{+-} gap, i.e. an s-wave gap which changes sign between different Fermi surface pockets ($\Delta_{\mathbf{k}} = \Delta_0$, $\Delta_{\mathbf{k}'} = -\Delta_0$). In the orbital-nematic scenario, instead, the inter-pocket interaction gives $V_{eff} < 0$, therefore the proposed configuration would be an s^{++} gap, formally equivalent to the s-wave gap described above ($\Delta_{\mathbf{k}} = \Delta_0$) (18). For this reason, it is important to determine the leading instability in the nematic phase, in order to gain insight into the pairing mechanism of IBSs.

Part II.

Experimental methods

3. Thermodynamic probes

In the previous Chapter, the main thermodynamic quantities and relations relevant for this PhD dissertation were introduced. In this Chapter, firstly, the measurement principles related to the main experimental techniques will be presented and then the specific features as well as limitations of the experimental setups used for this work will be discussed. In particular, for this experimental work the following physical quantities were used to characterize IBS samples: the magnetization (M), the heat capacity (C_p) and the linear thermal expansion coefficient (α), see Section 2.1. In order to probe phase transitions and relevant physical properties for solid state physics and for IBS in particular, it is fundamental to be able to reach low temperatures, through the use of cryogenic systems (e.g. LN_2, ^{4}He and ^{3}He), as well as to vary the external magnetic field applied to the sample. It has to be noted that the measurements that will be presented in this section are bulk techniques, i.e. they probe the overall physical response of the sample, and therefore do not give information about the spatial distribution of the signal itself.

3.1. SQUID magnetometry

The DC magnetization was measured as a function of temperature and magnetic field by means of a Superconducting QUantum Interference Device Vibrating Sample Magnetometer (SQUID-VSM) by Quantum Design. For temperature dependent experiments, in the cryostat used for this work the sample can be cooled down to a minimum temperature of 1.8 K and measured up to 400 K. An external magnetic field can be applied in the range ±7 T. Typically, the $M(T)$ curves are obtained by cooling in zero field and measuring upon warming from 1.8 to 300 K with the magnetic field applied within the ab-plane ($\mathbf{H} \parallel ab$).

3.1.1. Experimental setup

Fig. 3.1.1 shows a schematic representation of the measurement setup used for this dissertation work. (19) A uniform magnetic field is applied in the axial direction by a superconducting magnet, with a magnetic field range of ±7 T. The SQUID sensor is inductively connected to a second-derivative gradiometer, i.e. a pick-up coil system made of supercon-

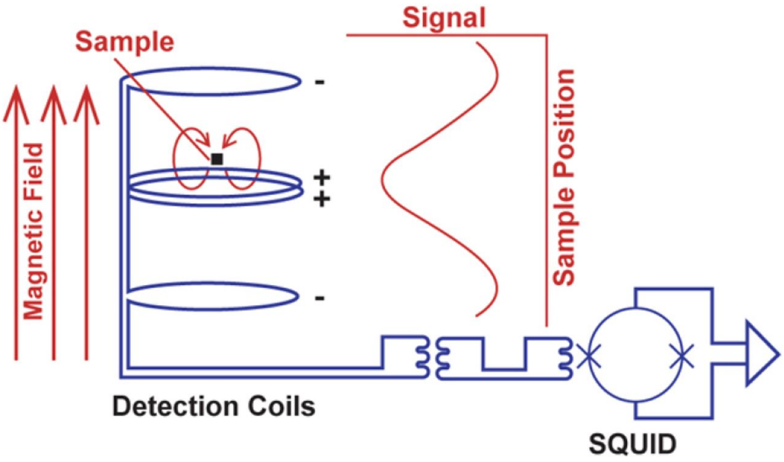

Figure 3.1.1.: Schematic representation of the detection system in the MPMS3 by Quantum Design connected to the SQUID sensor. The detection coils are marked as '+' or '-' to underline their opposite winding and the output voltage signal, obtained by moving the sample through all of the coils (i.e. corresponding to the DC mode described below), is shown aside. Taken from Ref. (19).

ducting materials composed of 4 windings (as shown in Fig. 3.1.1). By moving through the gradiometer the sample induces a current in the coils, through the stray field produced by its magnetization (M) in response to an applied external magnetic field H_{ext}. The particular configuration of the pick-up coils is intended to effectively cancel external sources of magnetic field (e.g. the applied external magnetic field or other signals coming from the environment) from the often smaller signal coming from the sample. In fact, the external signal can be approximated as a uniformly distributed field, which is effectively canceled out by having pick-up coils with opposite winding direction ('+' or '-' in Fig. 3.1.2 (b)). Such setup can be operated in two different modes, namely a DC-mode and a VSM-mode.

When performing a measurement in DC mode, the sample is moved through all the pick-up coils, thus producing a voltage signal as a function of the sample position (z). By fitting the $V(z)$ signal to a dipolar function the magnetic moment can be tracked. The procedure described so far is valid under the assumption of a perfect dipolar signal, i.e. the sample can be approximated as a point-like magnetic field source.

Notably, one of the main sources of uncertainty in the measurement is given by low frequency $1/f$ noise (20). For this thesis work, a vibrating sample magnetometry (VSM) technique was used, which grants a further improved resolution with respect to the measurements performed in DC mode. In this technique, the sample is oscillating in a smaller range around the center of the detection coils. Therefore, the resulting dipolar signal is modulated by a sinusoidal signal of fixed frequency, the resulting signal is then demodulated by a lock-in amplifier, thus cutting out the low frequency noise by a low pass filter,

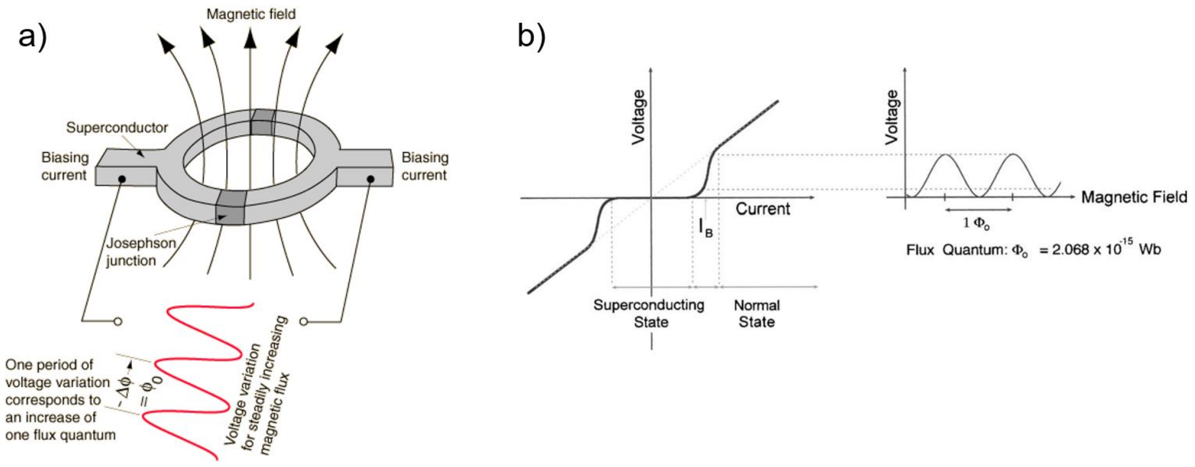
a)
Magnetic field
Superconductor
Biasing current
Biasing current
Josephson junction
One period of voltage variation corresponds to an increase of one flux quantum
$\Delta\Phi = \Phi_0$
Voltage variation for steadily increasing magnetic flux
b)
Voltage
Current
I_B
Superconducting State
Normal State
Voltage
Magnetic Field
1 Φ_0
Flux Quantum: $\Phi_0 = 2.068 \times 10^{-15}$ Wb

Figure 3.1.2.: Measurement principle of the SQUID detection: (a) schematic representation of the SQUID sensor; (b) voltage vs current characteristic for a single Josephson junction (left panel), where the applied bias current (I_B) is chosen to be lower than the critical current of the superconductors. Voltage output of the SQUID sensor as a function of the magnetic field through the ring. Taken from Ref. (20).

and the magnetic moment of the sample is recovered with increased resolution.

A careful calibration of the instrument with a standard reference material (in our case palladium) is needed in order to obtain reliable magnetization values. Geometric effects, stemming from differences in lateral dimensions of the sample with respect to calibration, also have to be taken into account and can lead to an under- or over-estimation of the absolute moment. For the purpose of this work, the samples were glued to a quartz rod (sample holder) by means of GE-Varnish. The use of a long rod of pure quartz assures that no additional magnetic contribution is added to the sample signal, nevertheless the small (mostly diamagnetic) signal (of the order of 10^{-7} emu) from the glue was separately measured as a function of temperature and field and subtracted from the magnetization curves when relevant (i.e. when the signal of the sample is comparable to the background, and therefore this latter cannot be neglected).

3.1.2. SQUID detection

The SQUID sensor is a quantum device which is able to precisely track small variations in the magnetic flux and it is commonly used to study the magnetization (M) of a material. Such device is composed by a superconducting ring typically containing two Josephson junctions (for which the physical principle will be explained below), that effectively allows to measure magnetic fields with high accuracy. In fact, the magnetic flux (Φ) measured through a SQUID sensor can only be probed in quantized values, i.e. integer multiples of a flux quantum (Φ_0), as

$$\Phi = n\Phi_0 \quad (n = 0, 1, 2, ...). \tag{3.1.1}$$

In such a way the resolution is then given by the flux quantum as $\Phi_0 = 2.068$ x 10^{-15} Tm^2 and, since a typical dimension of a SQUID sensor is ~1 cm^2, the field resolution can be estimated as $\Delta B \approx 2$ x 10^{-11} T. (20) In commercially available devices, the magnetization detection is based on the Josephson effect (10; 21), in which Cooper pair tunnelling is observed between two superconductors separated by a thin insulating layer. The superconducting tunneling current between the left (L) and the right (R) side of the junction is then described as

$$I = I_\mathrm{c} sin(\theta_\mathrm{L} - \theta_\mathrm{R}) = I_\mathrm{c} sin(\Delta\theta) \tag{3.1.2}$$

where I_c is the critical current of the Josephson junction, θ_L and θ_R are the phases of the many-body wave functions on either side of the junction. In fact, the amplitudes of the tunneling processes in both directions are $I_{\mathrm{L}\rightarrow\mathrm{R}} \propto e^{i(\theta_\mathrm{L}-\theta_\mathrm{R})}$ and $I_{\mathrm{R}\rightarrow\mathrm{L}} \propto e^{i(\theta_\mathrm{R}-\theta_\mathrm{L})}$, such that the sum of the contributions is proportional to $sin(\theta_\mathrm{L} - \theta_\mathrm{R})$. Fig. 3.1.2 (a) shows a schematic representation of a SQUID sensor, which is composed of a superconducting ring with two Josephson junctions on opposites sides. When a small external current ($I < I_\mathrm{c}$) is applied to the ring, then a steady current flow is expected (given that I_c has the same value for both junctions) and the phase differences across the two junctions are equal to each other ($\Delta\theta_1 = \Delta\theta_2 = \Delta\theta$). When a magnetic flux is present within the ring the phase differences have different values and the total current is then given by

$$I(\Phi) = I_\mathrm{c} sin(\Delta\theta) cos\left(\frac{\pi\Phi}{\Phi_0}\right) \tag{3.1.3}$$

and, therefore, the critical current can be written as

$$I_\mathrm{c}(\Phi) = I_0 \left| cos\left(\frac{\pi\Phi}{\Phi_0}\right)\right|. \tag{3.1.4}$$

From Equation 3.1.4 it is clear that the critical current is modulated by the magnetic flux sinusoidally with a periodicity of $\Phi_0 = h/2e$, where e is the electron charge and h the Planck constant. When the material is in the superconducting state, i.e. below the critical current, the magnetic flux is expelled from the ring. Therefore, the flux within the ring can be increased only for $\Phi = n\Phi_0$ (with $n = 0$, 1, 2,...). Considering that a non-zero voltage across the SQUID sensor can be probed when the critical current is exceeded, the measured voltage also oscillates in the external field with periodicity of the order of the flux quanta (Φ_0) inside the ring so that the flux can be obtained by counting the number of voltage maxima (n).

3.2. Heat capacity

As discussed in Section 2.1, studying the specific heat of materials can give important information about the temperature evolution of the entropy of the system, therefore it is particularly sensitive to probe phase transitions where entropy changes appear. Specific heat (C_p) measurements were performed by the relaxation method using a Physical Property Measurement System (PPMS) from Quantum Design.

3.2.1. Measurement principle

The measurement technique (23) used in this work uses a relaxation method to obtain the heat capacity of a sample. Fig. 3.2.1 (a) and (c) shows a schematic representation of this technique: the sample is placed on top of a highly thermally conductive sapphire platform and a good thermal contact is assured by a thermal grease (Apiezon). A heat pulse of constant power of amplitude P_0 is applied at the base of the platform for a finite time t_0, after which the power is set to zero. The heat produced is then transferred to the sample, that increases its temperature at a rate that depends on its C_p. The system is kept in vacuum ($p < 10^{-4}$ torr), such that when the heater is switched off, the excess heat in the sample can only be transferred by the connecting wires, which are in thermal contact with the cryostat at the temperature T_b. This process can be modeled by the differential equation

$$C_\mathrm{total}\frac{dT}{dt} = -K_w(T - T_b) + P(t) \tag{3.2.1}$$

where C_total represents the total specific heat of the system, K_w the thermal conductance of the wires and $P(t)$ is the time evolution of the applied thermal power, shown in the upper graph of Fig. 3.2.1 (a) and given by

$$P(t) = \begin{cases} P_0 & for\ 0 < t < t_0 \\ 0 & for\ t > t_0. \end{cases} \tag{3.2.2}$$

The measured quantity is then represented by the time evolution of the sample temperature, $T(t)$, recorded by a thermometer placed in contact with the sapphire platform. The temperature is given by the solution of equation 3.2.1, expressed as

$$T(t) = \begin{cases} \frac{P_0\tau}{C_\mathrm{total}}(1 - e^{-\frac{t}{\tau}}) + T_b & (0 < t < t_0) \\ \frac{P_0\tau}{C_\mathrm{total}}(1 - e^{-\frac{t_0}{\tau}})e^{-\frac{(t-t_0)}{\tau}} + T_b & (t > t_0) \end{cases} \tag{3.2.3}$$

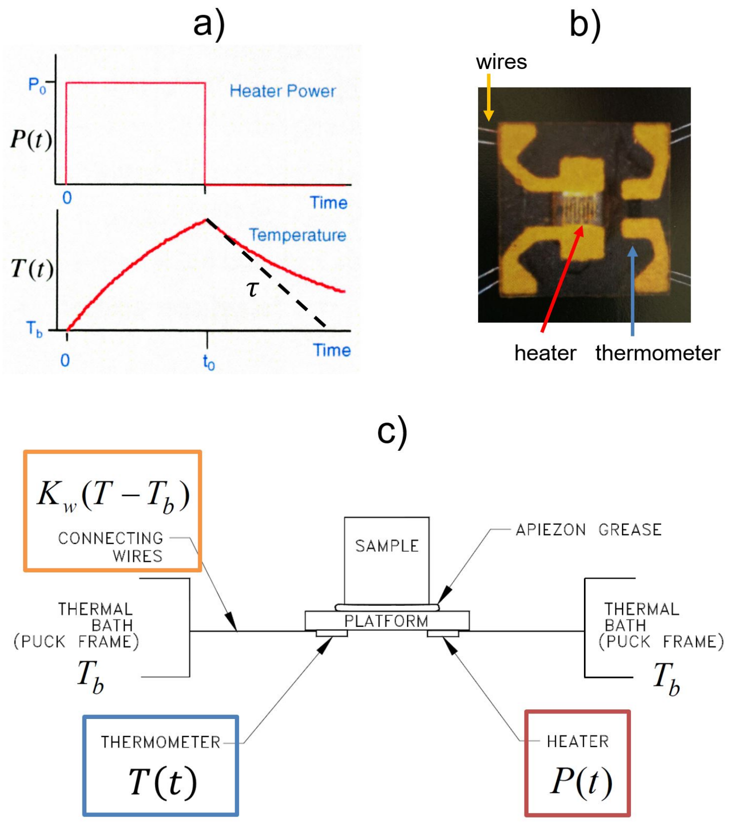
a)
P0
P(t)
Heater Power
0
Time
Temperature
T(t)
τ
Tb
0
t0
Time
b)
wires
heater
thermometer
c)
$K_w(T-T_b)$
CONNECTING WIRES
SAMPLE
APIEZON GREASE
THERMAL BATH (PUCK FRAME)
T_b
PLATFORM
THERMAL BATH (PUCK FRAME)
T_b
THERMOMETER
$T(t)$
HEATER
$P(t)$

Figure 3.2.1.: Measurement principle and schematic experimental setup for measuring heat capacity through the relaxation method: (a) time evolution of the heat pulse applied to the platform and the temperature measured by the platform thermometer. The time constant τ is proportional to the specific heat of the sample. (adapted from Ref. (23)); (b) schematic representation of the measurement setup used in this thesis, where the different terms in Eq. 3.2.1 are highlighted (adapted from Ref. (23)); (c) side view of the measurement platform from Quantum Design. The different components are marked with the same colors as in (b).

where the time constant of the exponential decay is then proportional to the total specific heat of the system ($\tau = C_{\text{total}}/K_{\text{w}}$). The temperature profile is fitted by this model both in the rising and in the decaying curve by the MultiVu software by Quantum Design. This assumption is valid when $T_{\text{sample}} \approx T_{\text{platform}}$ and thus if a good thermal contact can be assured between the platform and the sample itself, i.e. the thermal conductance between platform and sample is much higher than the wires ($K_{\text{sp}} \gg K_{\text{w}}$) and the system is correctly described by Eq. 3.2.3. If this condition cannot be fulfilled, the sample-platform temperature gradient (ΔT_{sp}) and the associated relaxation time (τ_{sp}) have to be taken into account in the so-called 2τ-model, which can give reliable specific heat measurements even for non-ideal thermal coupling, due to e.g. non-perfectly flat sample surfaces or low sample masses. Therefore the system can be described as

$$C_{\mathrm{addenda}}\frac{dT_{\mathrm{platform}}}{dt} = P(t) - K_{\mathrm{sp}}(T_{\mathrm{platform}} - T_{\mathrm{sample}}) - K_{\mathrm{w}}(T_{\mathrm{platform}} - T_{\mathrm{b}}) \tag{3.2.4}$$

$$C_{\mathrm{sample}}\frac{dT_{\mathrm{sample}}}{dt} = -K_{\mathrm{sp}}(T_{\mathrm{sample}} - T_{\mathrm{platform}}) \tag{3.2.5}$$

where for $K_{\mathrm{sp}} \gg K_{\mathrm{w}}$ the one tau model of Eq. 3.2.1 is recovered. Note that the measured quantity is $C_{\mathrm{total}} = C_{\mathrm{sample}} + C_{\mathrm{addenda}}$, where C_{sample} is the heat capacity of the sample, while C_{addenda} accounts for additional contributions, coming from the specific heat of the platform/heater/thermometer assembly as well as from the applied thermal grease. Therefore, the different contributions have to be measured separately and subtracted from the measured C_{total}.

As mentioned above, specific heat allows to effectively detect phase transitions in materials, through their associated entropy changes with temperature and magnetic field. The relaxation method allows to probe second order phase transitions on an absolute scale and important properties can be quantitatively assessed from their associated entropy changes. On the other hand, although first-order phase transitions are generally detectable by this relaxation method, therefore a quantitative analysis of such transitions is not possible from the model described above, due to the changes in the heat capacity happening in a temperature range (ΔT), which is smaller than the one generated by a single heat pulse (P_0).

3.2.2. Experimental setup

For this work, specific heat measurements are performed in a PPMS cryostat, that has a temperature range of T = 1.8 - 400 K with a superconducting magnet generating fields of $\mu_0 H = \pm\, 9\, T$. The PPMS system used for this work also allows to measure specific heat down to ^{3}He temperatures, through a dedicated ^{3}He probe and refrigerator by Quantum Design allowing to achieve a base temperature below ~0.4 K.

Fig. 3.2.2 shows a schematic drawing of the specific heat puck. The sample platform described in the previous section is inserted into a puck frame protecting the wires. As already mentioned, for a reliable measurement of the heat capacity the excess heat should be ideally exchanged mostly through the connecting wires and, for this reason, a thermal radiation shield is used to prevent heat exchange through irradiation from the sample. Heat exchange through convection is prevented by keeping the sample space in vacuum through the combination of a turbopump and a sorption pump (charcoal), positioned in close proximity to the puck. The puck frame is thermally and electrically connected to a

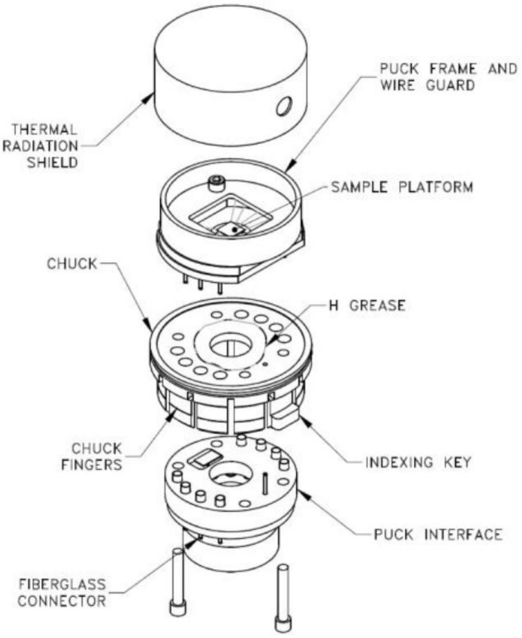

Figure 3.2.2.: Expanded view of the different components of the specific heat measurement puck for the PPMS and its connection to the Model 6000 electronics. Taken form ref. (23).

chuck, which is thermally connected to the ^{4}He cryostat through contact fingers, which then assures thermal connection between the cryostat and the wires. The chuck has connections to the PPMS Model 6000 controller electronics at the bottom of the cryostat.

3.3. Capacitance dilatometry

The thermal expansion of solids gives very important information about changes in the crystal structure of materials. As discussed in section 2.1, it is closely connected with the pressure dependency of entropy (see section 2.1) and it is influenced by electronic, phononic and magnetic properties. In addition, according to the Grüneisen formalism, it allows important statements about pressure dependencies of phase transitions in the system, by comparing it with heat capacity measurements (see section 2.3.1). The thermal expansion of solids (defined in section 2.1) can be most commonly determined by means of X-ray diffractometry (XRD), i.e. by deriving it from the measured lattice parameters as a function of temperature. As a 'microscopic' technique, it has the main advantage to be able to determine length changes in different crystallographic directions on polycrystalline samples and can reach a relative sensitivity of $\Delta L/L \sim 10^{-5}$. Optical methods, mainly based on interferometry, are also able to precisely determine the change in the lateral size of a sample, as a 'macroscopic' technique, reaching a resolution of $\Delta L/L \sim 10^{-7}$. In

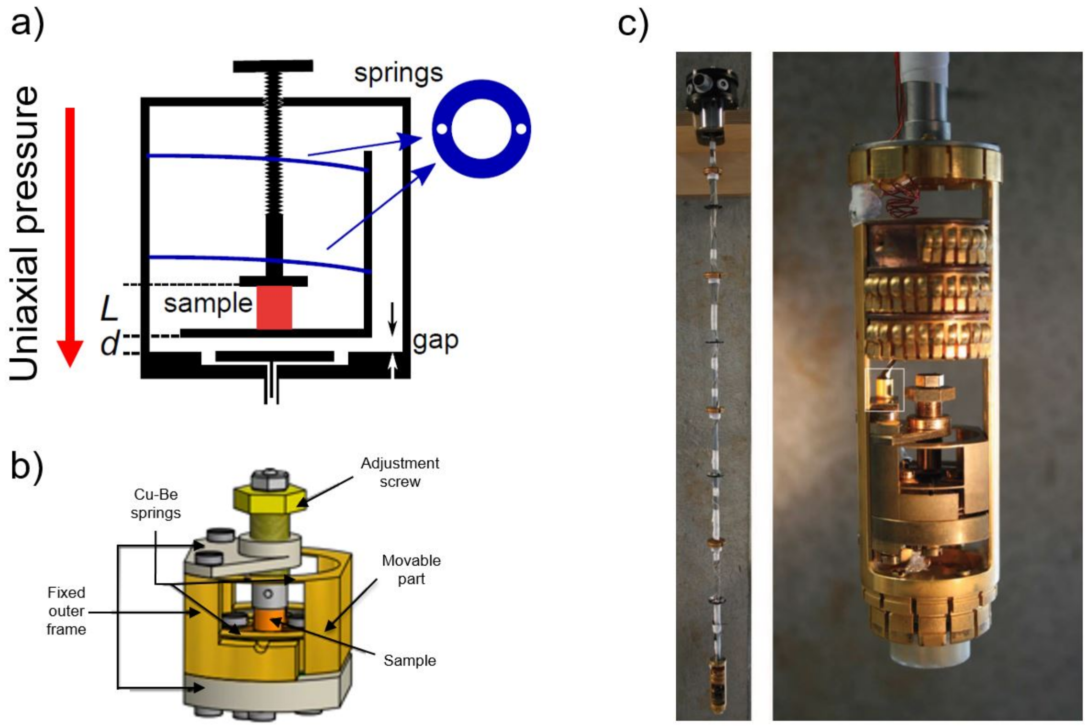

Figure 3.3.1.: Experimental setup of the capacitance dilatometer used in this work: (a) schematic representation of the dilatometry cell, in which the applied uniaxial pressure necessary to fix the sample to the movable part of the device is highlighted (adapted from Ref. (27)); (b) 3D model of the dilatometer (Küchler - Innovative Measurement Technology) showing the different components corresponding to the upper scheme (adapted from Ref. (28)); (c) insert adapted for the dilatometer for the use in the PPMS cryostat by Quantum Design (taken from Ref. (28)).

this context, capacitance dilatometry assures a very high level of experimental flexibility together with the currently highest possible measurement accuracy of up to a theoretical value of $\Delta L/L \sim 10^{-10}$. For this PhD work, capacitance dilatometry was used to probe the temperature evolution of lattice parameters throughout the Co doped La1111 series by orienting the samples along different crystallographic axes. This technique is able to precisely resolve changes in the sample length, $L(T,H)$, by measuring the change in the capacitance between two capacitor's plates (ΔC) with which the sample is in contact, as a function of temperature or applied magnetic field.

3.3.1. Measurement principle

Fig. 3.3.1 (a) shows a schematic representation of the dilatometer cell. The sample is positioned on top of a movable plate, while the second plate is fixed to the dilatometer's frame. In order to assure that the sample is always in contact with the capacitor, it is fixed from the top by a piston and a couple of circular springs, in order to hold the sample in position both during its expansion and shrinking, respectively. In this way, any change in the sample length (ΔL) directly translates into a change in the capacitor's gap distance (Δd), that can be detected as a change in the capacitance according to the formula

$$\Delta L = -\Delta d = \epsilon_0 \epsilon_\mathrm{r} \pi r^2 \frac{C - C_0}{C \cdot C_0} \tag{3.3.1}$$

where ϵ_0 is the dielectric constant in vacuum, ϵ_r is the dielectric constant in the medium, r is the radius of the circular capacitance plates and C_0 is the initial capacitance value (in our case this is taken as the capacitance at 300 K). It has to be noted that the measurement is taken in a ^4He atmosphere in order assure a good thermalization of the cell at the cryostat temperature. The gas is kept at a small pressure of $p \sim 3$ torr, so that the dielectric function can be approximated as $\epsilon_\mathrm{r} \approx 1$. In addition, in order to account for non-idealities in the measurement different corrections can be applied to Eq. 3.3.1. (29) For this work, the most relevant correction applied accounts for the non-perfectly parallel plates (28), that can be expressed as

$$\Delta L \simeq \epsilon_0 \pi r^2 \frac{C - C_0}{C \cdot C_0} \left(1 - \frac{C \cdot C_0}{C_{max}^2}\right) \tag{3.3.2}$$

where C_max represents the maximum capacity that can be reached before the plates get electrically in contact with each other, i.e. the capacitance drops to zero. In our case, $C_\mathrm{max} = 150$ pF and a typical measurement capacitance at 300 K after mounting accounts to $C_0 = 15$ pF, which gives a relative error of $\sim 1\%$ with respect to the ideal case. Ultimately, the corrected Eq. 3.3.2 was used to analyze the experimental data for this work.

3.3.2. Background subtraction

The measured length change, derived in Eqs. 3.3.1 and 3.3.2, intrinsically include the contribution given by the thermal expansion of the cell body (in our case made of Cu:Be), that directly modifies the capacitance plates gap distance (Δd) as a function of temperature or applied magnetic field. Therefore, the measured signal needs to be corrected by a reference sample of similar length as the sample and preferably of the same material of the cell itself. In this case, a good compromise is to use a high purity Cu sample, because it has an almost equal thermal expansion coefficient as Cu:Be. The signal should be subtracted from the measured sample length change ($\Delta L_\mathrm{total}^{meas}$) (28), such that the pure cell effect can then be obtained by adding back the well known $\Delta L/L_0$ of Cu from literature normalized

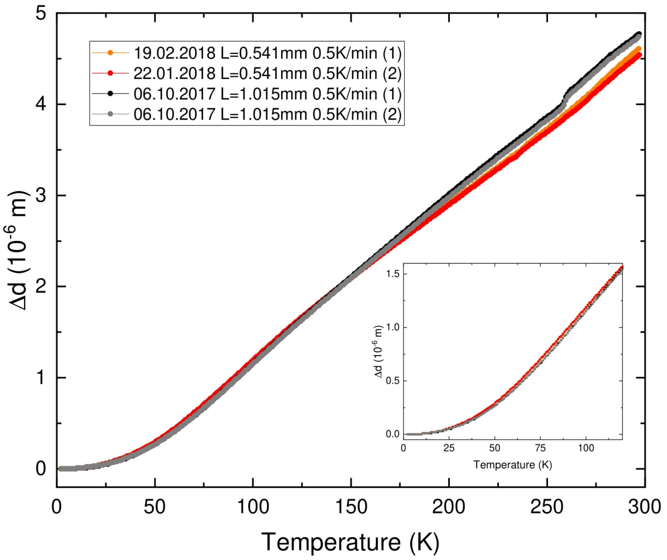

Figure 3.3.2.: Displacement of the movable capacitance plate (Δd) of the reference Cu sample as a function of temperature used to estimate the cell expansion background. The graph compares different Cu samples used for this work ($L\ = 1.015$ mm and $L\ = 0.541$ mm). The curves for each length are on top of each other and a feature is visible at $T = 250$ K, higher than the relevant temperature range for the measured samples ($T\ < 200$ K).

to the sample length, according to the formula

$$\Delta L^{meas}_{\text{sample}} = \Delta L^{meas}_{\text{total}} - \Delta L^{meas}_{\text{Cu}} + \left(\frac{\Delta L}{L_0}\right)^{lit}_{\text{Cu}} \cdot L^{300K}_{\text{sample}} \tag{3.3.3}$$

from which the the relative length's change can be obtained as

$$\left(\frac{\Delta L}{L^{300\text{K}}}\right)_{\text{sample}} = \frac{\Delta L^{meas}_{\text{total}} - \Delta L^{meas}_{\text{Cu}}}{L^{300K}_{\text{sample}}} + \left(\frac{\Delta L}{L_0}\right)^{lit}_{\text{Cu}} \tag{3.3.4}$$

where the literature values for pure Cu is taken from Refs. (30; 31), L^{300K}_{sample} is the sample length at 300 K. Fig. 3.3.2 shows Δd as a function of temperature for Cu reference samples of different lengths, namely $L\ = 1.015$ mm and $L\ = 0.541$ mm for repeated measurements upon warming for $T\ = 1.8$ - 300 K. The curves show good reproducibility between the same sample length within ~2%. The main difference in the cell effect between different Cu length is visible above 150 K. The curves show a measurement artifact at around $T\ = 250$ K, this feature is roughly corresponding to the one reported by Küchler (28) and for which the most probable explanation was found as a partial oxidation of the Cu of the cell, which has magnetic and structural transitions in this temperature range. The non-reproducibility of the anomaly hinders a correct subtraction from the measurement,

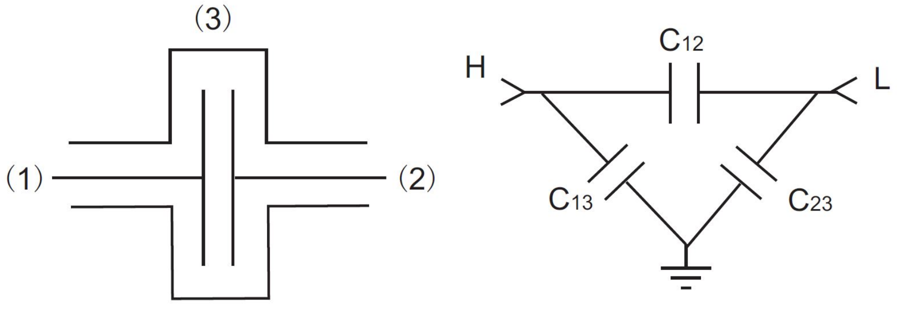

Figure 3.3.3.: Schematic representation of the three terminal capacitance measurement circuit: representation of the configuration (left panel) and equivalent circuit (right panel) of the three capacitors. Taken from Ref. (32; 33).

as previously reported by Küchler. It has to be noted that the overall curves do not show features for $T < 200$ K, which is the relevant temperature region for LaFeAsO studies in this work.

3.3.3. Experimental setup

A commercially available cell, designed by R. Küchler (28), was adapted to be used with the PPMS cryostat by Quantum Design in order to sweep temperature (1.8-300 K) and magnetic field (0-9 T). A schematic representation of the dilatometer cell as well as a picture of the insert adapted for the PPMS are shown in Figs. 3.3.1 (b) and (c), respectively. For this work, the sample was slowly cooled down to 1.8 K and measured in zero field and upon sweeping temperature to 250 K at 0.2 K/min. The use of a slow temperature sweep rate is important to assure good thermalization of the cell and sample during the measurements. In addition, a slow cooling rate from room temperature to the base temperature prior to the actual measurement is preferable to avoid the formation of unwanted mechanical stress in the body of the cell.

The capacitance signal was detected by means of a three-terminal capacitance bridge (32), shown in Fig. 3.3.3. In this configuration, the capacitor composed by the fixed (1) and movable (2) plates is surrounded by a shielding case (3), see Fig. 3.3.3 (a). The measured physical quantity in this technique is C_{12}, which may be superimposed to undesired stray capacitances, while C_{13} and C_{23} are the capacitances between each of the plates and the surrounding elements of the system, such as the capacitor case and the ground. In this way, the resulting stray capacitance is fixed and mainly dependent on geometrical factors of the cell. (33; 34) In this work, the use of a three-terminal configuration in a *Andeen-Hagerling* AH2500A capacitance bridge allowed to reach a resolution of 10^{-5} pF.

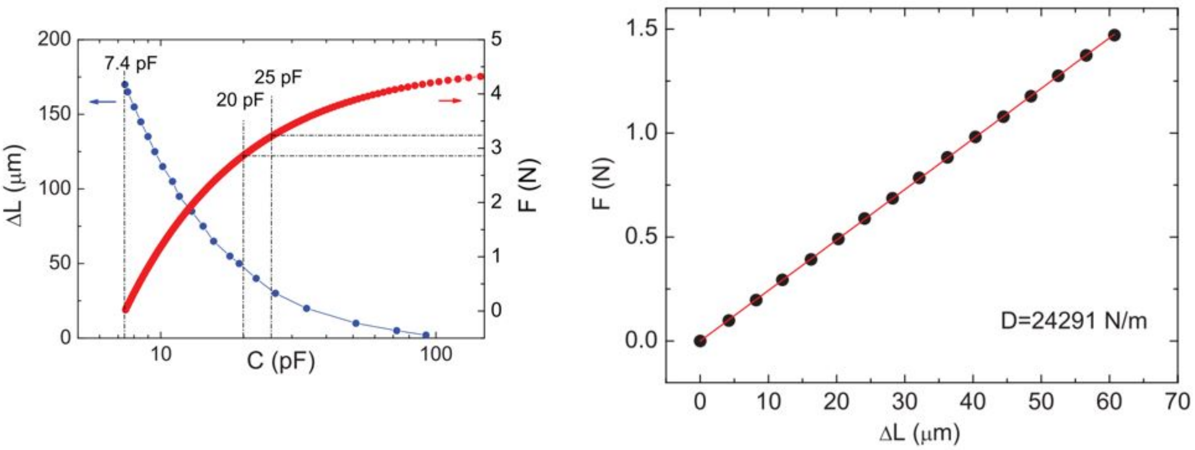

Figure 3.3.4.: Effect of varying the pressure exerted to the sample by the dilatometer: (a) displacement of the movable capacitance plate and applied force as a function of the measured external capacitance; (b) Force applied to the sample as a function of the displacement from which the overall spring constant was estimated as $D = 24291$ N/m. Taken from Ref. (28).

In order to minimize unwanted mechanical stress within different parts of the cell during temperature or field sweeps, it is important that all its components are constructed with the same material. In this case the chosen material is a Cu-Be alloy. In fact, it simultaneously allows good thermal conductance, assuring a fast and homogeneous thermalization of the cell to the cryostat temperature, but also good mechanical properties, that ensure the stability of the frame as well as good elasticity for the circular springs.

3.3.4. Pressure estimation

An important factor that has to be carefully taken into account when measuring the thermal expansion coefficient with this method is the pressure applied to the sample for fixation. Ideally, the length's change determined by equation 3.3.4 represents the zero-pressure limit ($p \to 0$). In the practice of dilatometry, in order to fix the sample as well as to increase the resolution in ΔC, a small external uniaxial pressure is always applied by the piston. Fig. 3.3.4 (a), (b) shows the force exerted on the sample as a function of the inital capacitance, from which the spring constant of the cell was estimated as $D = 24291$ N/m, and the length change as a function of the measured capacitance. The applied force F per unit area can be estimated as

$$p = \frac{F}{A} = \frac{1}{A}(-D \cdot \Delta d) \tag{3.3.5}$$

where A is the lateral size of the sample. In this case, $\Delta d > 0$ represents the displacement of the capacitor's plates upon mounting the sample and is given by

$$\Delta d = \epsilon_0 \epsilon_{\mathrm{r}} \pi r^2 \frac{C_0 - C_{\mathrm{empty}}}{C_0 \cdot C_{\mathrm{empty}}} \tag{3.3.6}$$

where C_0 is the capacitance measured after sample mounting, while C_{empty} is the empty cell capacitance (i.e. measured when no sample is mounted). Note that in this approach a precise determination of the lateral area of the sample represents the biggest source of uncertainty for the pressure estimation. Thus, a quantitative analysis of the pressure dependence of α by this method appears difficult and would require more dedicated setups, as reported in (35; 36), but it still allows to draw qualitative conclusions about the pressure dependence of the studied system.

Part III.

Thermodynamic properties of Iron-based superconductors

4. Iron-based superconductors

4.1. Introduction

Since the discovery of high-temperature superconductivity in F-doped LaFeAsO by Kamihara *et al.* (38) in 2008, iron-based superconductors (IBS) imposed themselves as a new promising class of high-temperature superconductors (HTS). Since then extensive studies were done and new families were soon discovered and successfully synthesized. Fig. 4.1.1 shows the critical temperatures for the main families of superconducting materials during the years. As evidenced in the graph, since their first report, IBS had a rapid increase in the critical temperatures due to intensive studies on newly discovered classes of materials and the highest T_c in bulk materials was reported for (Sr,Sm)FeFAs at $\sim$ 56 K (39). An important breakthrough for this class of compounds was reached for FeSe monolayers on a $SrTiO_3$ substrate, allowing to reach a record temperature above 100 K at the interface between the two materials (40; 41; 42). Therefore, by comparing these materials with other classes of HTS, it is clear that the fast improvement of T_c in IBS over the years is promising for obtaining better performing materials for applications (43; 44). This necessarily requires a deep understanding of the nature of the superconducting pairing in this as well as in other classes of HTS. In this respect, Fe-based compounds immediately attracted the attention of the scientific community due to common traits and differences with the main and most studied class of type II superconductors, i.e. cuprates. Such comparison appeared promising in finding a common origin of high temperature superconductivity. In fact, in both classes the superconducting state is reached by charge doping in close proximity to an antiferromagnetic phase, in presence of strong electronic correlations. One key difference is that, while for cuprates the parent compound is represented by a Mott-insulator, surprisingly for IBS its ground state is generally metallic (45; 46; 47). In this chapter, some general features about IBS, that will be relevant for the topics of this dissertation, will be presented, while, in the following ones, specific topics will be introduced in more detail.

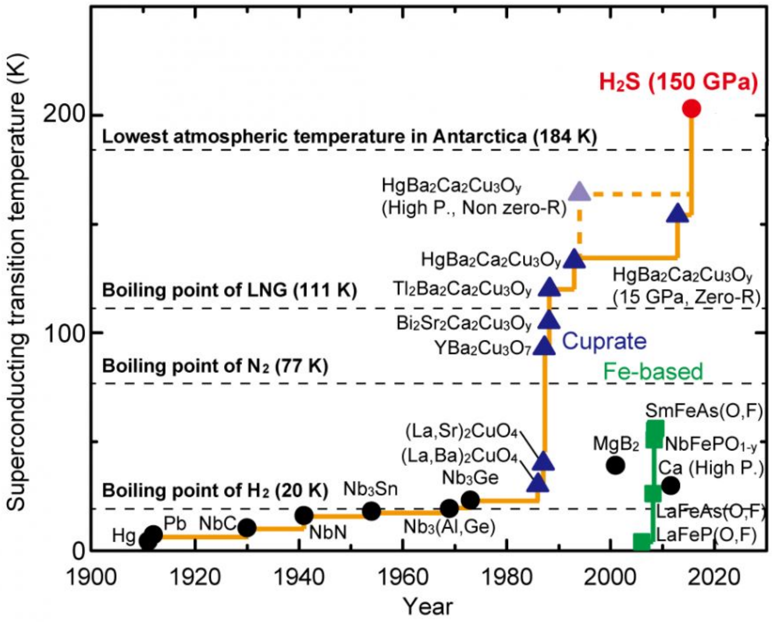

Figure 4.1.1.: Evolution of the maximum critical temperatures (T_c) reached over the years for the main families of superconductors. Taken from Ref. (37).

4.2. Crystal and electronic structure

Fig. 4.2.1 (a) shows the typical crystal structures of some of the most studied IBS systems. The different compounds are classified by their stoichiometry, such that the most prominent families are denoted as 1111 (e.g., LaFeAsO (38)), 11 (e.g., FeSe (50)), 122 (e.g., $BaFe_2As_2$ (51)) and 111 (e.g., LiFeAs (52; 53)). As can be easily noticed from the figure, all the crystal structures have common building blocks, which are constituted by the iron-pnictogen/chalcogen (FePn/Ch) layers, while the other elements are positioned between these layers. At high temperature the general unit cell of IBSs has tetragonal symmetry, while such structure is typically distorted into an orthorhombic configuration at low temperatures. Within the layers, the Fe atoms form a square sublattice, while the Pn/Ch atoms are positioned alternating above and below the Fe-Fe plane. Similarly to cuprate superconductors, IBS are considered as quasi-two-dimensional compounds and the common FePn/Ch structure is responsible for most of their physical properties. Fig 4.2.2 (b) shows the general bandstructure common to many FePn compounds (e.g. $BaFe_2As_2$, LaFeAsO), while for FeCh the number of hole bands can change for different compounds (45). Similar to other known high-temperature superconductors, e.g. MgB_2 (54), IBS are multiband systems, characterized by the presence of many electron- and hole-like bands crossing the Fermi level (E_F), while they only show a rather weak dependence on k_z. (55) In a typical electronic structure of IBSs, represented in the k_x-k_y plane, electron pockets are placed at the corners of the Brillouin zone (M points), while hole pockets lie at the center (Γ-point).

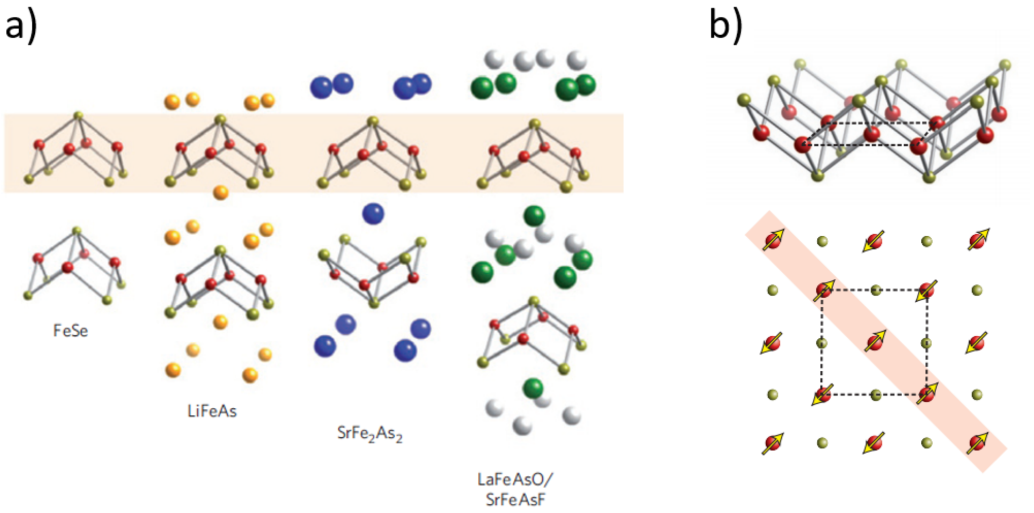

Figure 4.2.1.: (a) Crystal structures of the main families of IBS in the tetragonal unit cell. (b) The main building block is constituted by the FePn/Ch layers, denoted in red-green and red-yellow, respectively. The FePn/Ch layer is depicted from the side (upper panel) and from the top (lower panel) and the unit cell in the ab plane is delimited by the dashes line. The spin arrangement in the SDW phase is indicated in the lower panel, highlighting the anisotropy of the spin system. Taken from Ref. (48).

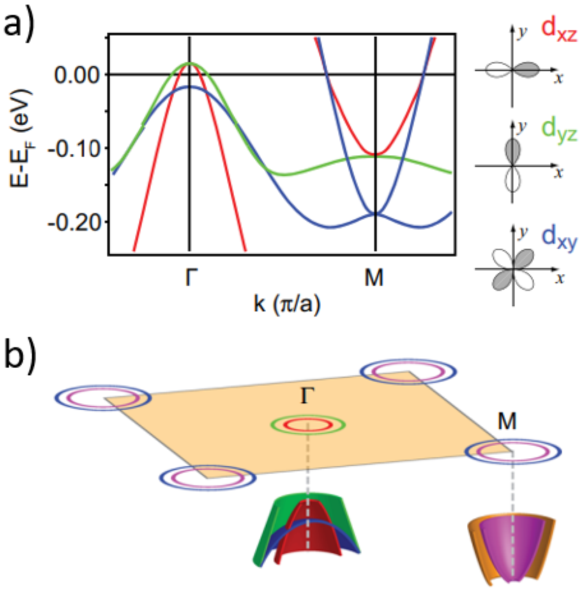

Figure 4.2.2.: (a) Band dispersion along the Γ-M direction in the Brillouin zone calculated by LDA approximation for NaFeAs. The right panel illustrates the main orbital characters of the bands crossing the Fermi level. (b) General Fermi surface topology of iron-based compounds. A schematic 3D representation of the main bands involved is shown in the lower panel. Taken from Ref. (49).

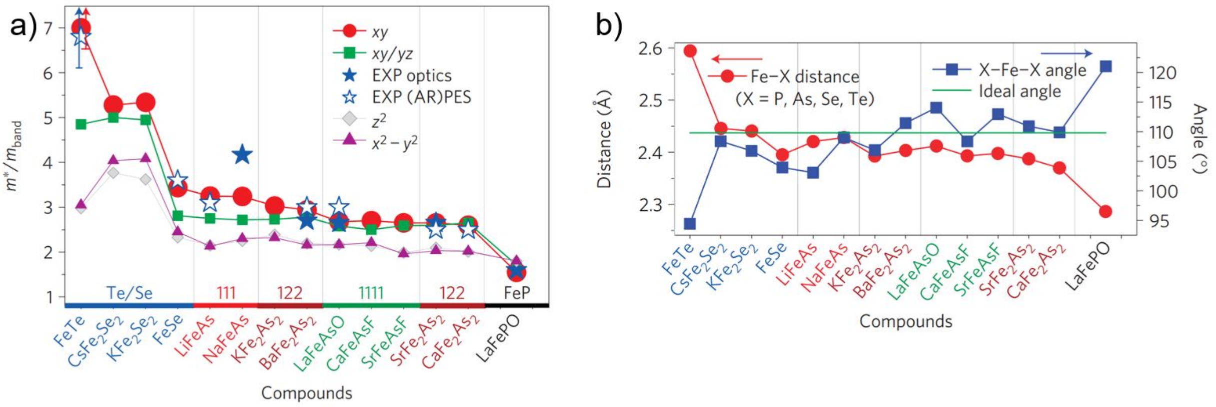

Figure 4.3.1.: (a) Mass enhancement $\frac{m^*}{m_b}$ of the iron $3d$ orbitals in the paramagnetic state calculated by DFT+DMFT calculations. For comparison, the low-energy effective mass enhancement obtained from optical spectroscopy experiments and angle-resolved photoemission spectroscopy experiments are added to the plot. (b) Relevant in-plane structural parameters for different iron-pnictides/chalcogenides. The green line denotes the angle corresponding to an ideal (undistorted) tetrahedral configuration. Taken from Ref. (56).

For the undoped parent compounds, the hole pockets at Γ and electron pockets at M are of similar sizes, thus suggesting that the magnetic spin-density wave (SDW) ordering is given by nesting between electron and hole bands. For hole(electron)-doped compounds, the hole pockets at Γ enlarge(shrink), while the electron pockets shrink(enlarge) and the nesting condition would be progressively lost following the suppression of the SDW phase with doping. Nevertheless, it is still under debate whether the SDW is originated from this mechanism (implying a purely itinerant description of the electron system) or other models should be used, e.g. super-exchange interaction of local moments. (49) Such bands, constituted predominantly by the Fe $3d$ orbitals (see Fig. 4.2.2 (a)), are substantially changed by electron and hole doping or stoichiometric substitution. In fact, for different doping levels and structural changes, the overall or relative positions of the hole and electrons bands may be shifted in energy, leading to different Fermi surface topologies with varying number of hole pockets and electron pockets. This demonstrates the importance of the electron filling in these bands in order to tune the physical properties of such compounds (see Chapter 5).

4.3. Electronic correlations in IBS

A common trait of many high-temperature superconductors is the vicinity of a highly correlated parent compound, therefore electronic correlations are believed to be an essential ingredient for superconductivity in these compounds. Various experimental as well as theoretical studies revealed different degrees of correlations among the different families of IBS (summarized in Fig. 4.3.1), ranging from the almost uncorrelated LaFePO to moderate correlated 1111 and 122 compounds ($m^*/m_\mathrm{b} \sim$ 2-3), until the highest values found for $A\mathrm{Fe_2Se_2}$ (A = Cs, K) or FeTe, that reach values similar to heavy-fermion compounds ($m^*/m_\mathrm{b} \sim$ 5-7). (56) Along with the increase of electronic correlations we can see a progressive differentiation between the $3d$ orbitals, in particular, a wider energy gap between t_{2g} and e_g levels. This behavior signals the vicinity of the system to an orbitally-selective Mott transition (OSMT), in which some orbitals can individually be localized, in virtue of their higher degree of correlations, while others are still in a metallic state. This phenomenon can be related to different physical properties in the system. In particular, by comparing Fig. 4.3.1 (a) and (b), the degree of correlations in Fe-based systems seems to be directly related to the Fe-Pn/Ch bond length, as would be expected from a weaker hybridization between Fe3d and As4p orbitals, resulting in a higher degree of localization. Also, the mass enhancement appears to be roughly inversely correlated to the Pn/Ch-Fe-Pn/Ch bond angle, and in particular to its deviation from the ideal tetrahedral angle (109.5°), which is closely connected to the crystal electric field, thus possibly influencing the average occupation of the $3d$ orbitals. This topic will be discussed in detail in Chapter 5.

4.4. General phase diagrams of IBSs

This relatively new class of unconventional superconductors has attracted a great interest during the last decades due to its rich phase diagrams, giving rise to a complex interplay between the different phases. As mentioned in the first paragraph, IBS are characterized by their metallic ground state, despite a non-negligible degree of electronic correlations. Typically, the parent compounds of IBS are characterized by itinerant antiferromagnetic ground states setting in at T_N. In particular, they tend to form spin density wave states, predominantly of stripe-type order, while they become paramagnetic for $T > T_\mathrm{N}$. The system also tends to spontaneously reduce its symmetry from a C_4 (tetragonal) to C_2 (orthorhombic) phase at $T = T_\mathrm{S}$. The lattice symmetry breaking is closely connected to other anisotropic physical quantities, such as its in-plane magnetization, and signals the onset of the so called nematic phase. This phase will be introduced and discussed in more detail in Section 6.1. Typically, superconductivity can be induced by changing some tuning parameter, such as external applied pressure, but also chemically by isovalent substitution (chemical pressure) or electron/hole doping and this is a common feature with cuprate superconductors. This is the case for many 122 and 1111 compounds. Conversely, some of the most studied Fe-based compounds, e.g. FeSe and LiFeAs, are stoichiometric

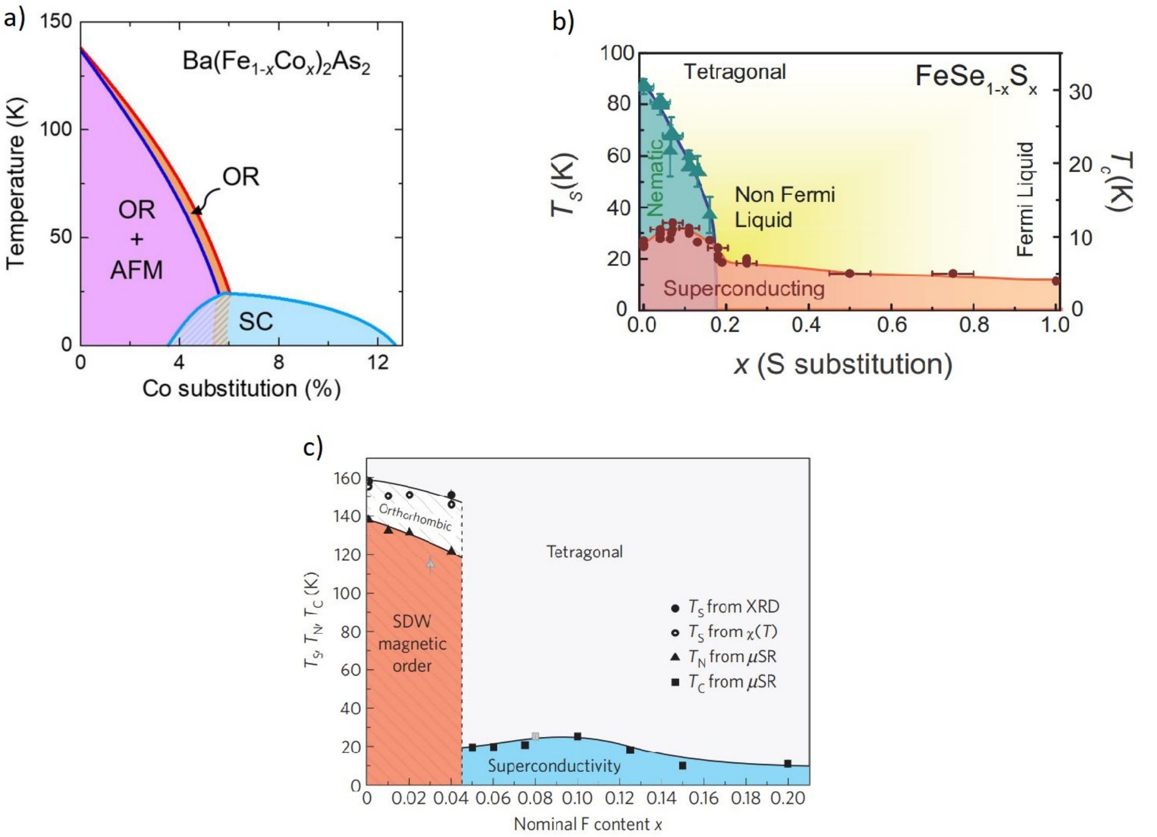

Figure 4.4.1.: Phase diagrams of exemplary compositions of 122, 11 and 1111 compounds. (a) Co-doped $BaFe_2As_2$ shows gradual suppression of the orthorhombic/SDW phase and microscopic coexistence between such phase and superconductivity. Taken from Ref. (60). (b) In S-doped FeSe upon the suppression of the nematic phase T_c is lowered accordingly, suggesting a cooperative interplay between the two phases. Taken from Ref. (60). (c) Phase diagram of the F-doped LaFeAsO showing a sudden transition between the nematic/SDW and SC phase, giving rise to a broad superconducting dome. Taken from Ref. (61).

superconductors, i.e. their parent compounds already show superconductivity without electron doping, and therefore their T_cs can be tuned by electron or hole doping. In addition, novel electronic phases, such as charge density waves (CDW), were found in close proximity to Fe-based pnictide superconductors in both stoichiometric and doped substitutions, such as $Ba(Ni_{1-x}Co_x)_2As_2$, $LaFe_{1-x}Mn_xAsO$ and $Na_{1-x}Li_xFeAs$. (57; 58; 59)

Fig. 4.4.1 shows a summary of the general phase diagrams for the 122, 11 and 1111 families. One of the most studied families of IBSs is the 122 family, with $BaFe_2As_2$ as the most prominent compound, that is not superconducting, as already stated above, and has nearly concomitant structural and magnetic transitions at ∼136 K, which are suppressed and tend to be separated in temperature by electron- and hole- doping. The 1111 compounds, e.g. LaFeAsO, are also characterized by the presence of structural and magnetic orderings, although in this case they generally appear to be well separated in temperature (e.g. $T_{\mathrm{S}} = 148$ K, $T_{\mathrm{N}} = 128$ K for LaFeAsO). From early studies on polycrystalline F-doped compositions, their doping dependence appears to be substantially different from the 122 compounds, with a first-order like suppression of the structural/magnetic phase in favor of superconductivity. Nevertheless, the general phase diagram for this family of IBSs appears not to be settled yet. This issue will be extensively discussed in Chapter 6. Notable exceptions are represented by FeSe and LiFeAs, which as stated above are stoichiometric superconductors but also show nematic ordering in absence of long-range magnetism, which can then be induced by the application of hydrostatic pressure to the systems. In many respects, the phase interplay between the magnetic and nematic phases with superconductivity is still regarded as an open question for Fe-based compounds.

5. Electronic correlations and structural changes in the series BaT_2As$_2$ (*T* = Cr, Mn, Fe, Co, Ni, Cu)

5.1. Electronic correlations in multiorbital systems (Hund's metals)

The presence of electronic correlations is an important aspect that characterizes many crystalline materials, such as heavy fermions, and is also believed to be a crucial element in the achievement of high temperature superconductivity. Electronic correlations are parametrized by the quasiparticle weight (Z), which is defined as

$$Z^{-1} = \frac{1}{N} \sum_{n=1}^{N} \left(\frac{m^*}{m_b} \right)_n \tag{5.1.1}$$

where the sum over the index n generalizes the formula for multi-orbital systems. By this definition, Z is inversely proportional to the mass enhancement, thus, the free electron model is recollected for Z=1, while the system becomes increasingly more correlated for Z → 0. As shown in Fig. 4.3.1, iron-based superconductors are spread through a wide range of correlation degrees, as seen by the formation of heavier quasiparticles with enhanced effective masses with respect to the free electron model ($\frac{m^*}{m_b}$). Generally speaking, in a correlated system the Coulomb repulsion between the electrons in the valence shells in many notable cases cannot be neglected (i.e. cannot be considered to be negligible in average due to to the effective screening of neighbouring electrons in the Fermi sea, as it happens in most of the common metallic materials) and their average interaction is represented by the effective Coulomb potential (U). Correlated electronic systems can be adequately described by the Hubbard model

$$H = \sum_{<i,j>=1}^{N} t_{i,j} + U_{i,j} \tag{5.1.2}$$

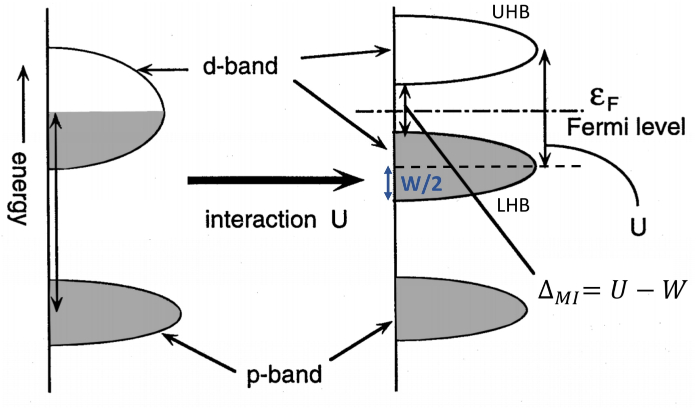

Figure 5.1.1.: Schematic representation of the energy levels involved in the formation of a Mott-insulator from a single-band metallic system. Adapted from Ref. (62).

where i and j are the indices of the single lattice sites, $t_{i,j}$ the hopping integral between adjacent sites i,j and $U_{i,j}$ the Coulomb potential. Such model is particularly useful for describing correlated systems, because it can simultaneously take into account both the itinerant and the localized components of the outer shells electrons. (6)

In systems for which the physical properties are mainly determined by one single active half-filled band at the Fermi level (E_F), the presence of a sizable degree of correlations tends to form a Mott-insulating state. In such a state, when the electron coupling exceeds a critical value (U_C), an energy gap (Δ_{MI}) opens up and two different bands are formed (see Fig. 5.1.1): one completely filled band which lies lower in energy, the lower Hubbard band (LHB), and one empty band higher in energy, the upper Hubbard band (UHB), thus giving rise to a metal to insulator transition (MIT). Since each of the Hubbard bands are broadened by a quantity W/2, the value of the energy gap can be estimated as $\Delta_{MI} = U - W$, therefore the critical Coulomb term required for the band localization (U_C) is obtained by imposing $\Delta_{MI} = 0$, thus giving U_C=W. This case is realized in cuprate superconductors, where the half-filled electronic configuration leads the system to a Mott insulating state, where the antiferromagnetic (AFM) order is progressively disrupted by dilution within the CuO planes and can be driven to the superconducting state both by electron and hole doping. (17) In such cases, the degree of electronic correlations is ultimately determined by the proximity to a Mott-insulating state, which depends exclusively on the magnitude of the Coulomb potential (U).

In multiorbital systems (such as Fe-based superconductors), thus characterized by the presence of multiple bands crossing the Fermi energy (E_F), such simple model is not sufficient anymore to describe their physical properties. It is therefore necessary to consider both inter- and intra-orbital Coulomb interactions, which will ultimately result in the

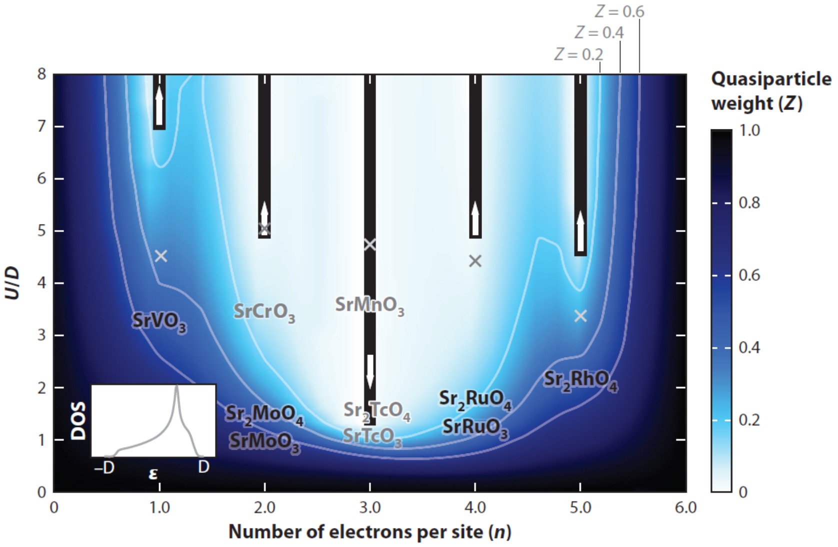

Figure 5.1.2.: Color coded plot of the quasiparticle weight Z in a model with 3 orbitals, for $J_{\mathrm{H}}/U = 0.15$, as a function of the Coulomb potential, U, and the number of electrons per site, i.e. empty ($n = 0$) to full orbitals ($n = 6$). Darker regions correspond to good metals and lighter regions to bad metals. The black bars signal the Mott-insulating phases for integer filling, while the white arrows denote the expected evolution of U_{C} upon increasing J_{H}. It has to be noted that for 2 electrons (2 holes) orbital filling a bad-metal behavior is present for a wide range of U/D values, i.e. high correlations while a rather metallic ground state is preserved. Specific materials are schematically placed on the diagram and signalled by gray crosses. Taken from Ref. (64).

introduction of the Hund's coupling (J_{H}). In this case, a simple interaction Hamiltonian that accounts for Hund's rules coupling can be expressed by

$$H_i = (U - 3J_{\mathrm{H}})\frac{N(N-1)}{2} - 2J_{\mathrm{H}}S^2 - \frac{1}{2}J_{\mathrm{H}}T^2 \tag{5.1.3}$$

where N denotes the total charge, S the spin and T the angular momentum operators. U is the intraorbital interaction and J_{H} is the Hund's rule coupling. (63) Many theoretical works showed that Hund's coupling plays an important role in iron-based superconductors and ultimately the physical properties of this family of compounds is determined by the interplay of the Coulomb potential, the Hund's coupling and the crystal field splitting (Δ). The main results of such studies are summarized in Fig. 5.1.2, where a color coding plot shows the degree of correlation (defined by the quasiparticle weight, Z) as a function of the average filling of the 3d bands (n) and the Coulomb potential normalized to the half-bandwidth (U/D) for a fixed value of J_{H} (the black columns representing the Mott-insulating state for integer values of filling). (64; 63) The calculation were performed on

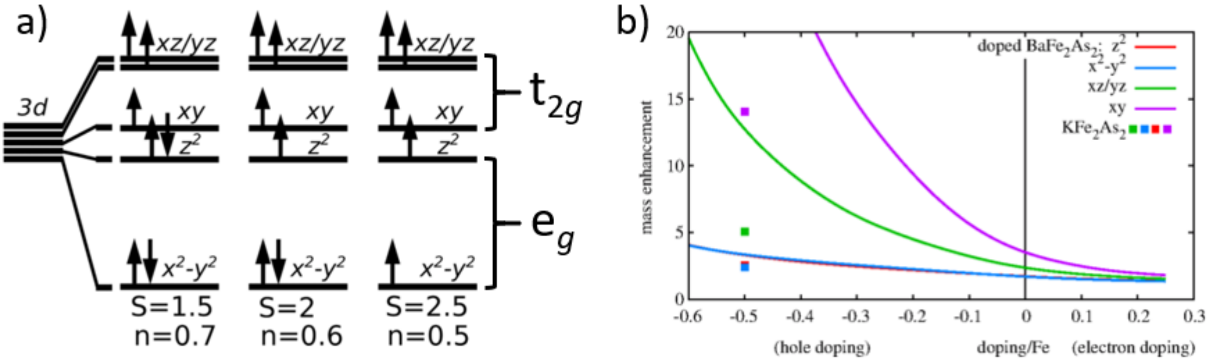

Figure 5.1.3.: (a) Sketch of some of the most probable configurations in electron- and hole- doping in 122 iron-pnictide systems. Here n indicates the electronic filling normalized to the total number of electrons in 3d orbitals and S is the total spin. (b) Mass enhancement values calculated for different orbitals as a function of 3d orbital fillings, where the 0 doping represents the 3d^6 configuration of BaFe$_2$As$_2$. Taken from Ref. (65) and (64), respectively.

a 3 orbital model (i.e. hosting 6 electrons), but the results can be extended to realistic 3d orbitals. (64) The graph illustrates that for the half-filled configuration ($n = 3$) the system can be easily driven to a Mott-insulating state in presence of moderate values of U, in agreement with what is expected for the previously discussed single band case, thus promoting an insulating ground state. Conversely, for other electron fillings the values of the critical Coulomb potential for which the metal to insulator transition lie at much higher energy, thus favouring an itinerant character of the charge carriers over a localized one. Another exception is given by single electron/hole fillings, for which the effect of increasing J_{H} is mostly to shift the critical Coulomb potential (U_{C}) to much higher energies accompanied by an overall decrease in correlations at a fixed value of U, thus promoting a good metallic regime.

The presence of a non negligible J_{H}/U ratio, has several important consequences that go beyond the tuning of the quasiparticle weight, although closely connected to it. As previously mentioned, away from half-filling, the behaviour of the system with increasing J_{H} can be described by apparently contrasting phenomena: on the one hand, a metallic behaviour is promoted and the minimum energy required to achieve band localization is consistently enhanced for increasing J_{H}, which tends to preserve an overall itinerant character (which in the single band limit is commonly associated with low electronic correlations); on the other hand, for wide range of constant U, correlations are enhanced (Z $\rightarrow$ 0) by increasing J_{H}, thus favoring high correlations also in systems with relatively modest U terms. Such competing effects ultimately are believed to be responsible for the peculiar behaviour of multiband compounds, thus giving rise to a relatively highly correlated bad-metallic

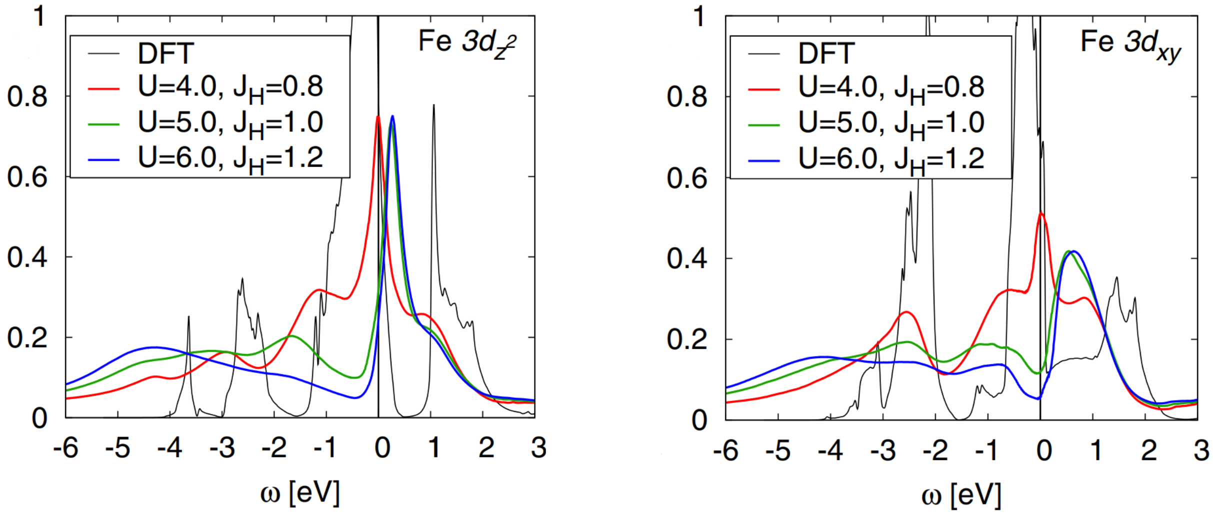

Figure 5.1.4.: The density of states for the Fe $3d_{z^2}$ (left) and $3d_{xy}$ (right) orbitals for the simulated $CsFe_2As_2$ compound with stretched a axis as a function of the on-site Coulomb repulsion U and Hund's coupling J_H. Taken from Ref. (65).

regime.

Moreover, theoretical calculations by de' Medici *et al.* (63; 64) showed that by increasing the magnitude of the Hund's coupling (J_H) the transition to a Mott-insulating state becomes more and more energetically favourable for the half-filled configuration, while it gets even higher in energy for all other orbital fillings (excluding the full and empty shell configurations). This model was able to explain some of the peculiar aspects of Iron-based superconductors, such as their overall itinerant character despite showing moderate to high values of carriers mass renormalization (accounting for electronic correlations), in some cases comparable to heavy fermion compounds (e.g. $CsFe_2Se_2$, FeTe). (56) Contrary to single band systems, the enhanced electronic correlations would then be ascribed mainly to the Hund's coupling rather than the Coulomb term.

It has been predicted that Hund's coupling actually acts as a band decoupler, such that charge carriers in different orbitals can have independent behaviour between each other. As discussed in Section 4.2, in the specific case of IBSs we are mainly interested in the occupation of the Fe $3d$ bands, which lie at the Fermi level. Fig. 5.1.3 (a) shows a scheme of the $3d$ levels for different electronic configurations and the associated total spin values, where $t_{2}g$ levels (i.e. $3d_{xy}$, $3d_{xz}$ and $3d_{yz}$) are higher in energy with respect to the e_g ones (i.e. $3d_{z^2}$ and $3d_{x^2-y^2}$). The simulated behavior of the different $3d$ bands in the vicinity of the $3d^6$ configuration (i.e. corresponding to Fe^{2+}) is shown in Fig. 5.1.3 (b), where we can see that different bands can independently assume different degrees of electronic correlations (i.e. mass enhancements), $3d_{xy}$ being the highest correlated, followed by $3d_{xz/yz}$,

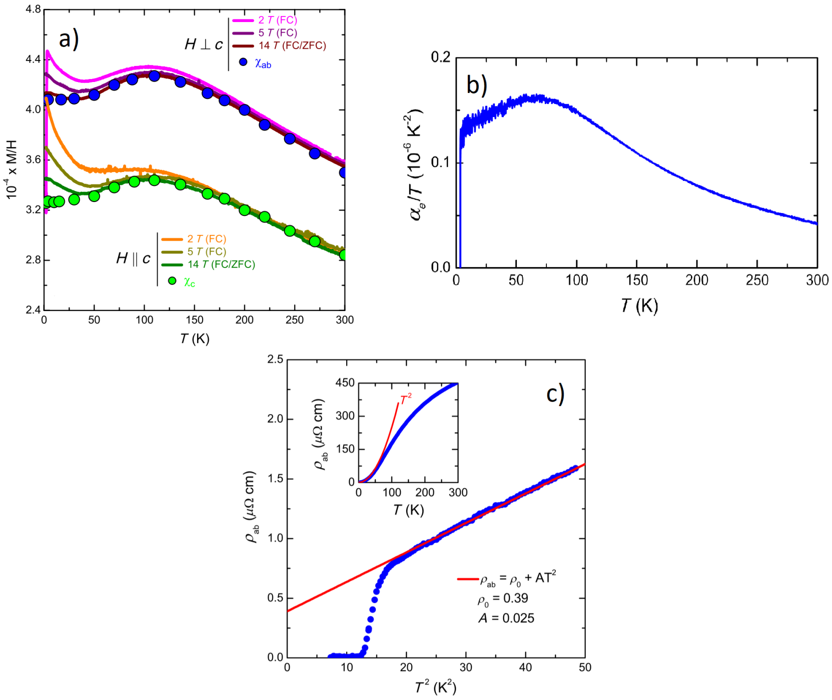

Figure 5.1.5.: Coherence to incoherence crossover anomaly at T* ∼ 120 K from different thermodynamic probes for the highly correlated KFe$_2$As$_2$ compound: (a) Magnetic susceptibility M/H measured for H⊥c and H∥c in different magnetic fields (solid lines). The symbols shows the temperature dependence of the intrinsic susceptibilities χ_c(T) and χ_{ab}(T) derived from magnetic isotherms (Honda-Owen analysis). (b) Temperature dependence of the electronic contribution of the linear thermal expansion coefficient ($\frac{\alpha_e}{T}$), showing a similar peaked feature. (c) Low-temperature in-plane electrical resistivity ρ_{ab} as a function of T^2. The solid line is a fit to a Fermi liquid behavior, $\rho_0 + AT^2$. The inset shows the temperature dependence of $\rho_{\text{ab}}(T)$ up to 300 K. Taken from Ref. (66).

while the e$_g$ levels are lowest and appear almost unaffected by doping. Fig. 5.1.4 shows the simulated local density of states for different combinations of U and J_{H} for $3d_{z^2}$ and $3d_{xy}$ for CsFe$_2$As$_2$, considered as one of the highest correlated Fe-based compounds. (65) By simultaneously increasing U and J_{H}, in fact, for $3d_{xy}$ orbitals the spectral weight is almost entirely transferred away from the Fermi level (mostly towards lower energies), with a continuous suppression of the quasiparticle peak, thus resembling the formation of Hubbard-like bands in a Mott-insulator. In contrast, for $3d_{z^2}$, the quasiparticle peak, though slightly shifted to higher energy, remains sharp with increasing interactions, thus maintaining a higher DOS at E$_{\text{F}}$. The pronounced difference for the two cases suggests the presence of differently correlated electronic populations, thus driving the system close to a so-called orbitally selective Mott-transition (OSMT).

As an effect of orbital selectivity, overall degree of correlations in the system (i.e. the itinerant/localized character of its electrons) can also vary as a function of temperature, i.e. allowing the occupation of higher energetic levels. As an example, this effect was experimentally measured by magnetic susceptibility (see Fig. 5.1.5 (a)) showing a maximum at around 120K, which was interpreted as a crossover between a low temperature coherent behaviour, characterized by a rather constant susceptibility typical of Pauli paramagnetism, and a high temperature incoherent state, with a localized Curie-Weiss like paramagnetic behavior. This feature seems to find correspondence to a similar peaked feature found in the electronic component of thermal expansion (see Fig. 5.1.5 (b)). This effect reflects also in transport properties, in fact, at low temperature the system is well described as a Fermi Liquid, as probed by a T^2-like dependence of the low T resistivity, while at higher temperatures a coherent quasiparticle description is no longer valid, giving rise to higher scattering rate and a bad-metal-like conduction, as can be seen from a peculiar linear increase of resistivity ($\rho(T) \propto T$), as shown in Fig. 5.1.5 (c). Such behaviour is typical of strongly correlated systems, e.g. heavy fermions, where such a crossover results from the interaction between different populations of localized and itinerant charges within the solid. In this case, even though we deal with a $3d$ system it was proposed that the close proximity to an orbitally selective Mott transition (OSMT), together with the pronounced orbital differentiation in terms of effective masses (m^*/m_b), can induce electron localization in some of the orbitals. (66)

In summary, within the orbitally selective Mott phase (OSMP), different orbitals can show different degrees of electronic correlations and the average occupation of the $3d$ orbitals play an important role in determining the physical properties of this class of compounds. In particular, in iron-based superconductors most of the physical properties derive from the $3d$ orbitals of Fe, which is typically Fe^{2+} with an average $3d^6$ configuration, and electron and hole doping around this value can induce superconductivity. While being away from half-filled configuration, the presence of the Hund's term prevents the system to become insulating as an effect of unscreened electron repulsion. Therefore, from the above discussion it appears evident that the filling of the $3d$ orbitals is considered to be a crucial parameter in order to tune electronic correlations in these materials.

5.2. Previous studies on 122 FeAs compounds

The evolution of electronic correlations with respect to electron filling of the $3d$ orbitals has been studied by different experimental probes, mainly for compositions in close proximity to the $3d^6$ configuration, corresponding to the oxidation state Fe^{2+}. The most studied family within the iron-pnictides is the so-called Ba122 family named due to their overall

BaT_2As$_2$ stoichiometry with T being a $3d$ transition metal from Cr-Cu (67; 68; 69; 70; 71) with BaFe$_2$As$_2$ and its doping variants as the best studied members.

Extensive studies of the evolution of the electronic correlations in both electron-doped Ba(Fe$_{1-x}$Co$_x$)$_2$As$_2$ and in hole-doped Ba$_{1-x}$K$_x$Fe$_2$As$_2$ were reported by Hardy *et al.* (72; 73) using thermal expansion and specific heat measurements. Fig. 5.2.1 shows the Sommerfeld coefficient (γ_n) extracted for various compositions as a function of electron counting in the vicinity of BaFe$_2$As$_2$, aiming at giving a detailed characterization in a small range of band filling (from $3d^{5.5}$ to $3d^{6.5}$) around this well known composition. As discussed in Section 2.2, γ represents the electronic contribution to the specific heat and is proportional to the density of states at the Fermi level, $\rho(\mathrm{E_F})$. In the doping region around the mother compound γ has a sharp decrease in absolute values at $x = 0.06$, corresponding to the maximal T_c in the superconducting dome. As discussed in Ref. (72), this corresponds to the insurgence of the itinerant antiferromagnetic phase and the progressive opening of a spin density wave (SDW) gap, contributing to lower gamma values. While, in the hole-doping region, after a rapid rise of gamma up to $x = 0.35$, due to the suppression of the SDW phase, it remains constant until $x = 0.7$ and rises again with decreasing band filling. The increase of correlation is accompanied for $3d^{5.5}$ compositions by the insurgence of a coherence to incoherence crossover at $\sim$ 100 K, probed by thermal expansion (73), as described in the previous section for KFe$_2$As$_2$. The presence of such a crossover is reminiscent of similar feature in heavy-fermion compounds, where conduction electrons screen local moments via the Kondo interaction, therefore further suggesting the presence of different populations of heavier and lighter (i.e. higher/lower correlated) conduction electrons in Fe-based compounds, as expected from theoretical predictions. Such effect, connected to orbital selectivity, appears to be enhanced by approaching the $3d^5$ half filling configuration and is accompanied by an overall increased γ. From Fig. 5.2.1 one can see that, by excluding the points in the SDW phase, the measured Sommerfeld coefficient is in overall good agreement with the trend predicted by theoretical calculations, thus confirming the correctness in modelling Fe pnictides as Hund's metals and demonstrating the relevance of J_H in these systems.

A recent work by de' Medici *et al.* (74) show a comparison between the experimental values for the mass enhancement ($\mathrm{m}^*/\mathrm{m}_b$) and theoretical calculations in the vicinity of the $3d^6$ configuration, where BaFe$_2$As$_2$ is doped both by electron and holes (shown in Fig. 5.2.2). The graph compares the values obtained by different experimental techniques, e.g. specific heat, optical conductivity, quantum oscillations and angle resolved photoemission spectroscopy (ARPES), in the doping range from $3d^{5.5}$ (KFe$_2$As$_2$) to $3d^{6.2}$ (Ba(Fe$_{1-x}$Co$_x$)$_2$As$_2$). The study finds an overall monotonic increase of the electronic correlations from the electron doped Ba(Fe$_{1-x}$Co$_x$)$_2$As$_2$ to the heavily hole doped KFe$_2$As$_2$,

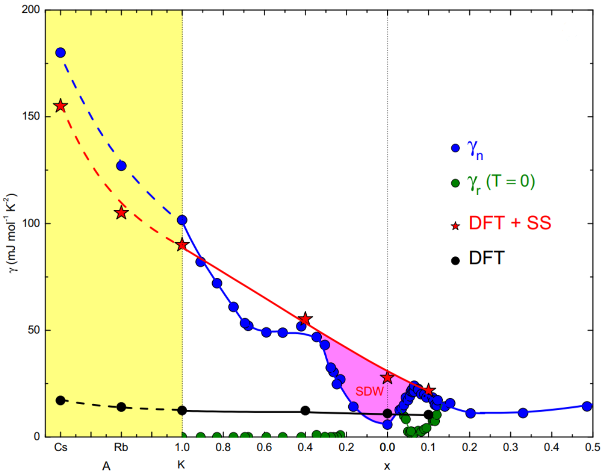

Figure 5.2.1.: Sommerfeld coefficient γ_n (blue symbols) and the residual electronic density of states, $\gamma_r = \lim_{T\to 0} \frac{C_e}{T}$, in the superconducting phase (green symbols) for $Ba_{1-x}K_xFe_2As_2$, $Ba(Fe_{1-x}Co_x)_2As_2$ and AFe_2As_2 (A = Rb and Cs). The red stars represent density functional theory+slave spin (DFT+SS) calculations for the tetragonal paramagnetic phase, while the black dots represent the DFT calculation only, which does not account for electronic correlations in the system. The magenta area indicates the loss of density of states due to the reconstruction of the Fermi surface in the SDW phase. Taken from Ref. (73).

hinting at a further increase towards the half-filled configuration and a decreasing trend for higher electron doping compositions. It has to be noted that by increasing hole doping the mass enhancement values extracted from specific heat and optical conductivity depart more and more from each other. This can be explained if we consider that bulk techniques actually probe a signal which is the average of the different orbitals in the system and that while the signal from specific heat studies is proportional to m^*/m_b, the value extracted by optical conductivity relates to its reciprocal, m_b/m^*. In this way, in the first case, by averaging, the heaviest bands would be weighted the most while in the second case the value is mainly given by the lightest ones. (74) In fact, it was predicted by theoretical calculations that by approaching the half-filled configuration, along with the enhancement of electronic correlations the orbital differentiation in terms of effective masses is also dramatically increased (see Section 5.1). This can be seen in m^*/m_b extracted by the band renormalization factor of the experimentally probed bands by ARPES with respect to DFT calculations (i.e. the latter do not include the effect of electronic correlations in the band structure), showing a factor ~5 between the lowest and the highest correlated bands for $3d^{5.5}$. The same behaviour is reported for quantum oscillation measurements (Fig. 5.2.2). To further support the scenario of high correlations in half-filled ($3d^5$) configuration, we can consider Mn-based pnictide materials, such as $BaMn_2As_2$ and LaMnAsO,

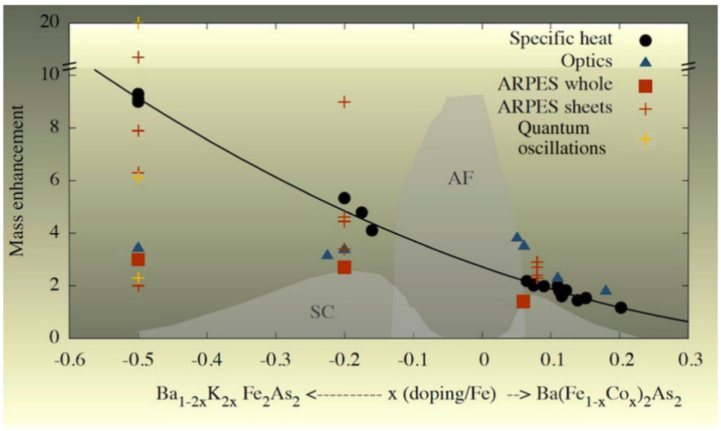

Figure 5.2.2.: Experimental values of mass enhancement in the vicinity of BaFe$_2$As$_2$ assessed by different techniques (72; 75; 76; 77; 78; 79; 80; 81; 82; 83; 84; 85; 86; 87; 88).The experimental phase diagram, including the antiferromagnetic metallic (AF) and the superconducting (SC) phases is shown as a background for comparison. The solid line is a fit of the mass enhancement determined by specific heat data. ARPES and quantum oscillation data corresponding to a given doping represent the values estimated for the different sheets of the Fermi surface, while the red squares labelled as "ARPES whole" represent the average value of the single bands (red crosses). It is clearly seen that electronic correlations increase monotonically as the filling is reduced towards the half-filled configuration and the values from different techniques spread more and more, stemming from an enhanced orbital differentiation (OSMT). Taken from Ref. (74).

for which electronic localization was found in different experimental probes, giving wise to a semiconducting ground state. (89; 90; 91; 92)

Optical spectroscopy measurements, reported by Nakajima *et al.* (93), were also used to probe the evolution of electronic correlations in an extended range of 3d occupations using stoichiometric compositions, namely from BaNi$_2$As$_2$ (3d^8) to KFe$_2$As$_2$ (3$d^{5.5}$) (shown in Fig. 5.2.3). It was found that electronic correlations are further progressively decreased by substituting Fe with Co/Ni, corresponding to 3d^7 and 3d^8 configurations respectively. In addition, by considering the isovalent substitution of As by P, the effect of chemical pressure within the ab-plane could be assessed. The results suggest that, in addition to to 3d band filling, electronic correlations are also sensitive to changes in the structure in the FeAs planes. In particular, the Fe-As-Fe bond angle (α_{bond}) weakens electronic correlations when departing from the ideal tetrahedral value of 109.5°, as suggested in a former theoretical work. (56) These observations further suggest a more complex interplay between electron counting and structural properties in determining the electronic correlations in these systems.

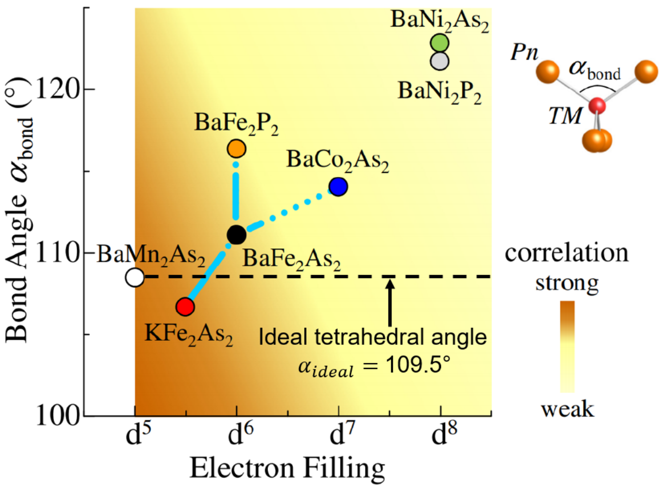

Figure 5.2.3.: Color coded map for the mass enhancement of T-pnictides as a function of Pn-T-Pn α_{bond} and electron filling of T d orbitals in the T^{2+} state. Blue lines indicate the doping compositions between two of the studied compounds: the solid lines denote the superconducting compositions while the dotted lines the non-superconducting ones. It is clearly seen that for BaMn$_2$As$_2$ ($3d^5$) α_{bond} is closest to the ideal tetrahedral angle of 109.5° and at the same time shows stronger electronic correlations, hinting at a non-negligible influence of the crystal structure in this respect. Correlation strength is schematically represented by the indicated color map. Taken from Ref. (93).

Although the evolution of electronic correlations in response to the $3d$ electron count has been studied in BaFe$_2$As$_2$ doping variants as outlined above, a systematic investigation, comparing electronic correlations in a series of high-quality stoichiometric crystals, where the average occupation of the $3d$ bands at the Fermi level (E$_\mathrm{F}$) is progressively changed from $3d^4$ to $3d^{10}$, is missing so far. In addition, such an approach with a full transition metal substitution would also avoid the additional presence of disorder coming from a random substitution of Fe or Ba by dopants always present in most of the already investigated series (e.g. Ba(Fe$_{1-x}$Co$_x$)$_2$As$_2$). Please note that changing the d elements also directly affects the structure, i.e. different atomic sizes of T may influence bond lengths and bond angles sterically while different inherent electron affinities of the $3d$ elements may cause changes in orbital hybridization and thus affect the bond nature in addition. As discussed in detail by Yin *et al.* (56), these changes of structural properties can be related to changes of electronic correlations. Accordingly, a detailed understanding and mapping of both the structural changes and the evolution of electronic correlations of this series of BaT_2As$_2$ is worthwhile to obtain more insight in the structure-property relationship in this class of materials.

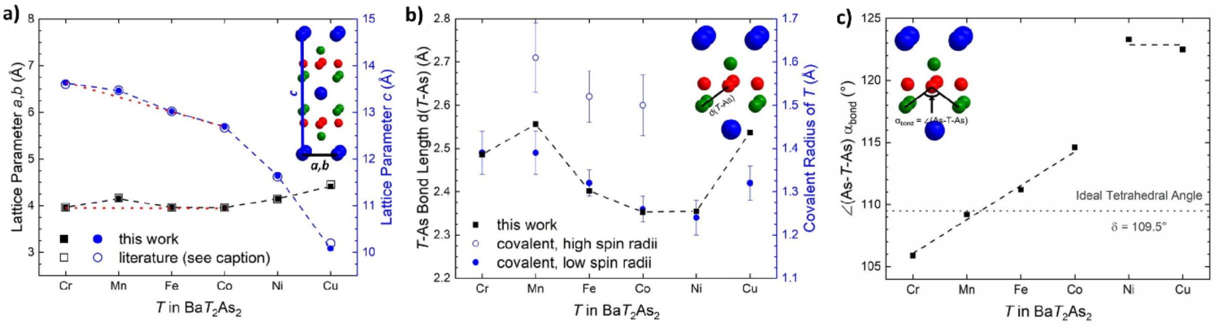

Figure 5.3.1.: Selected structural parameters as a function of the d-band filling in BaT_2As$_2$: (a) The lattice parameters a, b (left axis, black), and c (right axis, blue) for the tetragonal unit cell. (b) The bond distance between transition metal T and As d(T-As) (left axis, black). For comparison, the evolution of the covalent radius (94) (right axis, blue) as a function of T is shown. (c) The angle α_{bond} in As-T-As. In (a), black and blue dashed lines are guides to the eye. Red dotted lines in a and b indicate the linear trend observed for T = Cr, Fe, Co. The uncertainty of the experimental values is of the order of the size of the data points. Lattice parameters for T = Fe are adapted from Ref (95). For literature values, see T = Cr, Co (96), T = Mn (97), T = Ni (98) and T = Cu (99). Taken from Ref. (100) (own publication). (Measurements and analysis by S. Selter and S. Wurmehl)

5.3. The substitution series BaT_2As$_2$ (T = Cr, Mn, Fe, Co, Ni, Cu)

In the following chapters, a systematic investigation of the substitution series BaT_2As$_2$ (T = Cr, Mn, Fe, Co, Ni, Cu) via thermodynamic methods is presented. Magnetization measurements were performed in order to probe the magnetic ground state of the compounds as well as to verify the good quality of the single crystals. By analyzing the electronic part of the low temperature specific heat, the average mass enhancement (m^*/m_b) can be extracted and analyzed as a function of the 3d band filling (n). The mass enhancement data were then compared with structural parameters extracted from XRD diffraction, in order to explore the effects of structural changes on the electronic correlations. The study aims at providing a systematic investigation of the evolution of electronic correlations over a broad range of compositions using a series of single crystals with homogeneous growing conditions, in order to verify the theoretical predictions present in literature. (64)

5.3.1. Structural properties

Fig. 5.3.1 shows the evolution of some relevant lattice parameters throughout the substitution series from Ref. (100). The a parameter is substantially constant among the series, while upon substituting T the main effect lies in the shortening of the c axis. (see Fig. 5.3.1(a)) It has to be noted that, while only a moderate change can be seen for T = Cr-Co, Ni and Cu substitutions determine a faster decrease of c. The measured values are in good agreement with previous reports. (95; 96; 97; 98; 99) As shown in Fig. 5.3.1(b), the bond length of Cr, Fe, Ni, Co compounds change according to the increased ionic radius, but it appears elongated for Mn and Cu compounds. Therefore, the bonding character is different for the latter samples. Due to the hybridization between T 3d and As p orbitals, well known from previous works in literature (101; 102; 103; 104; 105), it is expected that the bonds would be mostly of covalent nature. In particular, for Mn122 the half-filled configuration of the 3d orbitals would lead to an elongation of the bond length, while for T = Cr, Fe, Co, Ni the bond length evolution follows almost exactly the one expected for covalent bonding. Comparing these parameters with T substitution of other IBS families,e.g. LiTAs and LaOTAs, this trend appears to have universal character for this class of compounds. (100) In the case of T = Cu, the completely filled d-shell configuration is energetically favored. Therefore, one of the two 4s electrons is transferred to the d shell of Cu resulting in a $3d^{10}4s^1$ electronic configuration, while the remaining single 4s electron is not sufficient to fill the bands of As. This actually destabilizes the uncollapsed structure and resulting in the so called "collapsed" structure, in which interlayer As-As bonds are formed, thus influencing the T-As distance.

The trend for the As-T-As bond angle α_{bond} shows two distinct regimes (Fig. 5.3.1(c)), where a monotonous linear increase is observed across T = Cr-Co and a jump to much higher α_{bond} values for T = Ni and Cu. A bond angle of $\alpha_{\mathrm{bond}} = 109.2°$ is found for T = Mn close to the ideal tetrahedral angle of 109.5°. (100)

5.3.2. Magnetic properties

In order to probe the magnetic properties of the series BaT_2As$_2$ (T = Cr, Mn, Fe, Co, Ni, Cu), the magnetization was measured as a function of magnetic field and temperature with the magnetic field applied within the ab-plane.

Fig. 5.3.2(a) shows $\chi(T)$ and M(H) for BaCr$_2$As$_2$ ($3d^4$). The susceptibility is rather temperature independent up to 400 K. However, a small upturn is visible at low temperature, which can be fitted by a Curie-Weiss law up to ~40 K consistent with the small curvature without hysteresis in the $M(H)$ curve at 2 K at low magnetic fields (inset of Fig. 5.3.2(a)). This most probably denotes the presence of paramagnetic impurities, estimated to be less

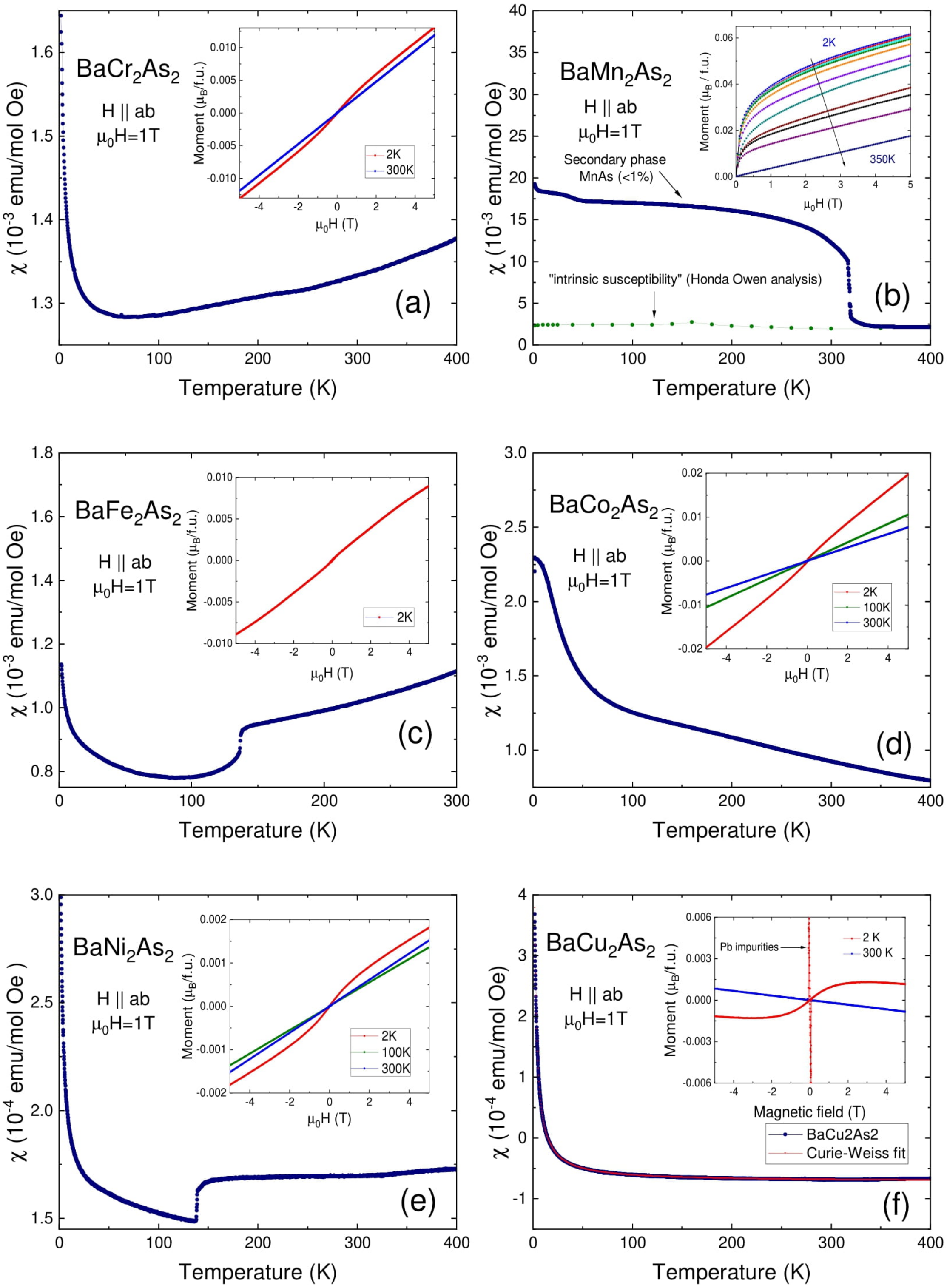

Figure 5.3.2.: Magnetic susceptibility as a function of temperature and magnetization as a function of the external magnetic field within the substitution series for BaCr$_2$As$_2$ (a), BaMn$_2$As$_2$ (b), BaFe$_2$As$_2$ (c), BaCo$_2$As$_2$ (d), BaNi$_2$As$_2$ (e) and BaCu$_2$As$_2$ (f). An external magnetic field of $\mu_0 H = 1$ T was applied within the ab plane for all the compositions. Taken from Ref. (100) (own publication).

than 0.1%. The overall increase of the magnetic susceptibility upon increasing temperature above about 100 K is compatible with an AFM ordering at higher temperature as reported by Filsinger *et al.* (71) who revealed an AFM transition at $T_{\mathrm{N}} = 580$ K.

Fig. 5.3.2(b) shows the magnetic susceptibility for BaMn$_2$As$_2$ ($3d^5$), which presents a clear ferromagnetic (FM) phase transition at about 320 K. However, as already reported by (89; 90), BaMn$_2$As$_2$ single crystals grown by the self flux method may suffer from inclusions of a FM secondary phase, ordering at ∼318 K, hinting at the presence of small residuals of MnAs from the growth. Thus, the observed transition probably corresponds to a small amount of such a secondary phase in our crystals. In order to extract the intrinsic magnetic susceptibility, a Honda-Owen analysis has been performed using isothermal $M(H)$ curves (106; 107) (inset of Fig. 5.3.2(b)). From the curves it is clear that the FM secondary phase is already saturated at 3 T and that this contribution is superimposed to a linear $M(H)$ behaviour. The slope then gives the intrinsic χ value for BaMn$_2$As$_2$. Considering the value of the intercept for $H \rightarrow 0$ of the linear high field region, the amount of the secondary phase inclusions can be estimated to be $< 1\%$. From the extracted intrinsic $\chi_i(T)$ curve (green curve in Fig. 5.3.2(b)), a nearly temperature independent χ_{ab} is observed, which coincides with the original curve for $T > T_{\mathrm{C,MnAs}}$. This is in agreement with previously published susceptibility data up to 800 K (89; 90), showing an AFM transition measured at higher temperature ($T_{\mathrm{N}} = 625$ K), which orders in a G-type AFM configuration.

BaFe$_2$As$_2$ is well known in literature to have a nearly concomitant structural and magnetic transition from a high temperature tetragonal/paramagnetic to a low temperature orthorhombic/itinerant antiferromagnetic phase. (108) The magnetization and specific heat curves (Figs. 5.3.2 (c) and 5.3.5 (a)) find such transition temperature at $T_{S,N} \sim 136$ K and the characteristic linear behaviour of the magnetic susceptibility in the high temperature region, in good agreement with literature values (109; 110). The small low temperature Curie tail, together with the absence of visible hysteresis in $M(H)$ at low temperature (inset of Fig. 5.3.2(c)) speak for the purity of the crystals, i.e. giving no clear indication for substantial paramagnetic and ferromagnetic impurities, respectively.

BaCo$_2$As$_2$ ($3d^7$), Fig. 5.3.2(d), shows a nearly temperature independent behaviour with a slightly negative slope at high temperatures and no phase transitions. An upturn below ∼50 K is clearly visible in the curve, but it is not well described by a Curie-Weiss law and tends to saturate at very low temperature. At high temperatures, $M(H)$ shows a linear behaviour while at 2 K an additional curvature is observed in the low-field region probably stemming from PM impurities present in the sample. The amount of paramagnetic impurities is estimated, as already shown for the Mn compound, to not exceed ∼1% of the sample mass. The overall behaviour of this compound was discussed in previous stud-

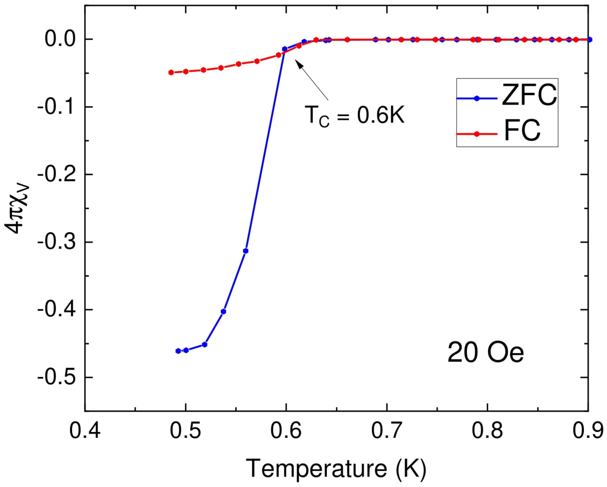

Figure 5.3.3.: Zero field cooled (ZFC) and field cooled (FC) measurements for BaNi$_2$As$_2$ at 20 Oe probed down to ^{3}He temperatures (0.48-1 K). A clear superconducting transition can be seen at $T_C = 0.6$ K. Taken from Ref. (100) (own publication).

ies (111; 112; 113) as a correlated itinerant paramagnetic system, which is most probably close to a FM instability, in which the low temperature behaviour of $\chi(T)$ in absence of sizable hysteresis can be explained by the presence of FM fluctuations in the system.

BaNi$_2$As$_2$ ($3d^8$), Fig. 5.3.2 (e), shows a constant $\chi(T)$ behaviour above 150 K with a step-like transition at $\sim$ 137 K, which is associated with a first-order structural transition, as reported in previous works (114). In this case, contrary to BaFe$_2$As$_2$, the structural transition is claimed not to be followed by a magnetic AFM ordering. In the low temperature region of the $\chi(T)$ curve a Curie-like upturn is visible. From a Curie-Weiss fit up to $\sim$ 40 K the Curie constant was extracted as $C_{\text{CW}} \sim 3.7 \text{ x } 10^{-4}$ emu K/mol Oe, indicating the presence of less then 0.5% paramagnetic impurities in the sample. M(H) curves were measured at 2, 100 and 300 K (inset of Fig. 5.3.2(e)), revealing an overall linear behaviour for higher temperatures, while the curvature at 2 K in low fields (< 2.5 T) indicates the presence of paramagnetic impurities already seen in $\chi(T)$. No appreciable hysteresis is visible in the curves. The sample was further measured at ^{3}He temperatures down to 480 mK with an applied field of 20 Oe (Fig. 5.3.3). It shows a clear superconducting transition, determined as $T_C = 0.6$ K by taking the bifurcation point of ZFC and FC measurements in good agreement with literature values. (114; 115)

Fig. 5.3.2 (f) shows the magnetic susceptibility as a function of temperature and field for BaCu$_2$As$_2$. The curves reveal an overall diamagnetic behaviour with a small paramagnetic impurity tail at low temperature. This scenario is supported by a modified Curie-Weiss fit for the full temperature regime

$$\chi(T) = \chi_0 + \frac{C_{\mathrm{CW}}}{T - \theta_{\mathrm{CW}}}, \tag{5.3.1}$$

where a diamagnetic component χ_0 was added and the overall modelling, resulting in $\chi_0 = -7.2 \times 10^{-5}$ emu/mol Oe, C_{CW} = 1.14 x 10^{-3} emu K/mol Oe, θ_{CW} = -0.7 K. In particular, we obtain a Curie-Weiss constant C_{CW} = 1.14 x 10^{-3} emu K/mol Oe, which is two orders of magnitude lower than the value expected for a Cu^{2+} $3d^9$ ($S = 1/2$) paramagnet. This confirms that the intrinsic magnetic ground state is diamagnetic ($3d^{10}$ configuration of Cu in BaCu$_2$As$_2$) and it is superimposed with a paramagnetic signal coming from a small amount of impurities (< 1%). The inset of Fig. 5.3.2 (f) shows the isothermal $M(H)$ curves at different temperatures. The curve at 2 K shows a sharp increase of the magnetization at very low fields and a broad maximum at ∼2 T followed by a decrease in the high-field region. The presence of a maximum can be explained by the saturation of paramagnetic impurities, dominating at low temperature and low fields, which restores the intrinsic negative slope at higher fields, corresponding to the diamagnetic behaviour found in $\chi(T)$ and in line with the negative slope of $M(H)$ at higher temperature (T = 300 K). The sharp peak in $M(H)$ at 2 K close to zero field is due to a superconducting signal, with a low critical field $H_{\mathrm{c}} \sim$ 750 Oe and a measured $T_{\mathrm{c}} \sim$ 7.2 K (not shown), which corresponds to the presence of a small amount of lead from the flux that was used to grow the Cu compound.

Overall, the magnetic behaviour is in agreement with the theoretical predictions for BaCu$_2$As$_2$ to be an *sp*-metal, having $3d$ bands lying far below E_F and, thus, yielding a Cu$^+$ state with fully filled $3d$ bands ($3d^{10}$). (116) This configuration was also confirmed experimentally by ARPES measurements on BaCu$_2$As$_2$ single crystals. (70) However, since BaCu$_2$As$_2$ is not well studied in literature, this result was corroborated by optical reflectivity measurements on crystals from the same batch as used for the thermodynamic studies in this thesis.

5.3.3. Optical conductivity

Fig. 5.3.4 shows the room temperature optical reflectivity of BaCu$_2$As$_2$ (measurements by M. Knupfer and M. Naumann). The data reveal a broad plasma edge around 0.4 eV and a high reflectivity value at low energies, which signals metallic behavior and no bandgap could be detected in the measured energy range. This finding is in agreement with theoretical predictions of an *sp*-metal (116) (see also Section 5.3.2). The reflectivity reaches a local minimum at around 0.65 eV and starts to increase towards higher energies. This

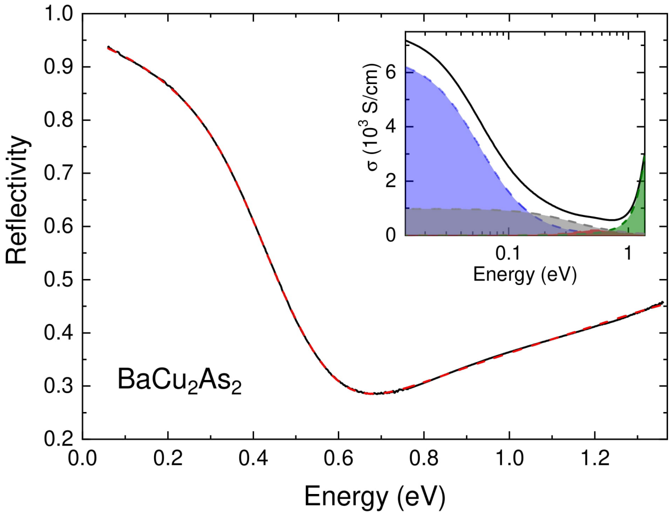

Figure 5.3.4.: Optical reflectivity of BaCu$_2$As$_2$ at room temperature taken in the *ab*-plane of the crystal. The solid black line represents the measured data. The result of the Drude-Lorentz fit is shown as dashed red line (for details of the fit see text). In the inset the optical conductivity is shown, which results from the fit of the reflectivity data. The individual components are depicted as dashed lines: narrow (Drude 1, striped blue) and broad (Drude 2, striped grey) Drude peaks; Lorentz peaks (Lorentz 1, striped red and Lorentz 2, striped green). Taken from Ref. (100) (own publication). (Measurements and analysis by M. Knupfer *et al.*)

value	Drude1	Drude2	Lorentz 1	Lorentz 2
ω_0	0	0	0.52	1.50
Γ	0.05	0.34	0.48	0.60
ω_p	1.66	1.59	0.81	4.01
ϵ_{inf}	9.39			

Table 5.3.1.: Summary of the fit parameters of the Drude-Lorentz fit to the reflectivity of BaCu$_2$As$_2$. Two Drude-components and two Lorentz-components as well as a dielectric background ϵ_{inf} are included into the fit model. The two Drude terms model the conduction electrons while the two Lorentz terms and the background dielectric constant, ϵ_{inf}, represent the contribution of inter-band transitions in the measured energy range. Each component is represented by its oscillator strength ω_p, its energy position ω_0 ($\omega_0 = 0$ for the Drude terms), and its spectral width Γ. See Ref. (117) for details. Taken from Ref. (100) (own publication). (Measurements and analysis by M. Knupfer and M. Naumann)

increase can be related to the contribution of interband-transitions in this energy range and above. In order to achieve more detailed insight, the reflectivity data were modeled using a Drude-Lorentz approach (see Ref. (117) for details). Please see table 5.3.1 for a summary of the fit parameters of our Drude-Lorentz fit.

In total, four different components allowed to describe the data almost perfectly. Two Drude terms model the conduction electrons while two Lorentz terms and the background dielectric constant, ϵ_{inf}, represent the contribution of inter-band transitions in the measured energy range. Each component is represented by its oscillator strength ω_p, its energy position ω_0 ($\omega_0 = 0$ for the Drude terms), and its spectral width Γ. With the help of this fit the optical conductivity of the sample was obtained which is shown in the inset of Fig. 5.3.4.

From the modeling of the spectrum with different components, the low energy part can be well reproduced by two Drude components, a narrow (Drude 1) and a broad one (Drude 2). This is in good agreement to previous optical investigations of related compounds. (93) As suggested by Nakajima *et al.* (93), the narrow Drude component represents the contribution from coherent charge carriers, as expected for a system of free charge carriers. In analogy with cuprate superconductors, the additional presence of a broad peak centered in the mid-infrared region was interpreted as a consequence of electronic correlations in the system. Therefore, the relative weight of the narrow Drude component $\omega^2_{(p1)}/(\omega^2_{(p1)} + \omega^2_{(p2)})$ can be used to estimate the importance of electronic correlations in a given material. For BaCu$_2$As$_2$ the extracted values is about 0.52, corresponding to a highly coherent metal and the electronic correlations are, thus, expected to be weak.

5.3.4. Specific heat capacity

The heat capacity of the Fe and Ni compounds was studied, up to high temperatures in order to probe structural and magnetic transitions already seen in the magnetization measurements (section 5.3.2). The specific heat data of BaFe$_2$As$_2$ and BaNi$_2$As$_2$ in the temperature range 2-160 K are shown in Fig. 5.3.5. The well known BaFe$_2$As$_2$ presents an anomaly at $\sim$136 K, commonly associated with the almost concomitant structural and magnetic transitions from the high-temperature tetragonal to the low-temperature spin density wave (SDW) orthorhombic phase. BaNi$_2$As$_2$ shows a clear anomaly at $\sim$137 K, which is in good agreement with previous reports (118; 119). This anomaly is believed to be exclusively related to a structural transition, but in this case from a tetragonal to a triclinic symmetry (114). It has been discussed by Chen *et al.* that the difference in the electronic configuration of Ni with respect to Fe would result in a change of the band structure, such that the nesting condition cannot be satisfied for the Ni compound,

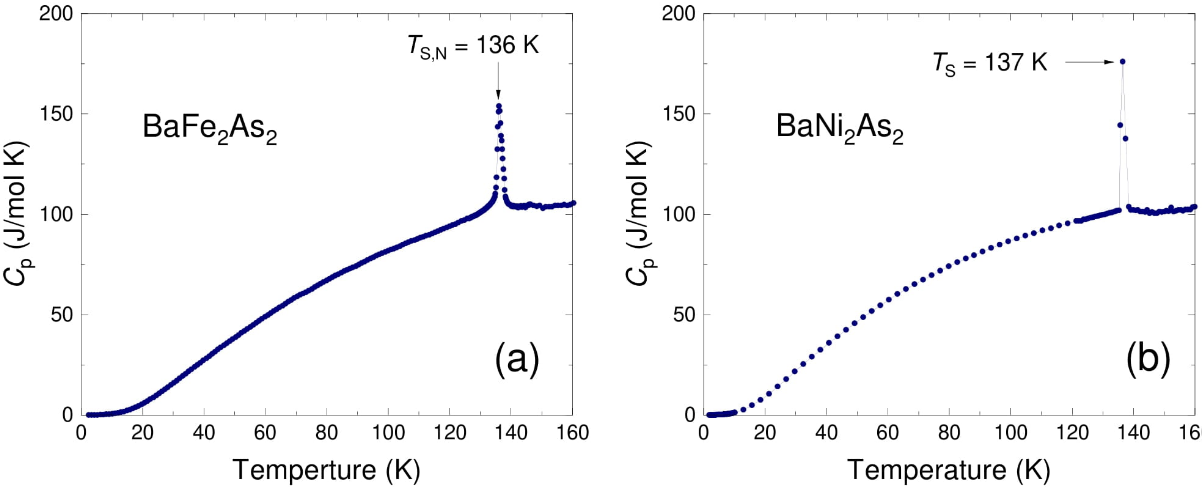

Figure 5.3.5.: Zero-field specific heat as a function of temperature for BaFe$_2$As$_2$ (a) and BaNi$_2$As$_2$ (b) single crystals in the temperature range 2-160 K. Taken from Ref. (100) (own publication).

resulting in the absence of antiferromagnetic order. (118)

The other members of this series do not show any anomaly in the magnetic susceptibility for 50 K $< T <$ 400 K, therefore $C_p(T)$ was measured in the low-temperature range (2-50 K) only. In the following, the used approach to extract the Sommerfeld coefficients γ_{exp} from the specific heat data will be explained in more detail.

As introduced and discussed in Section 2.2, the specific heat at low temperatures, i.e. for $T \ll \theta_D$, and in absence of other contributions (e.g., due to magnetic ordering or Cooper pairing), can be modeled as

$$C_\text{p}(T) = \gamma T + \beta T^3, \tag{5.3.2}$$

where γ is the Sommerfeld coefficient related to the electronic contribution to the specific heat, while βT^3 accounts for the lattice contributions within the low-temperature approximation of the phononic specific heat. We applied this approach to the specific heat data of each specific compound across the BaT_2As$_2$ series with T = Cr-Cu. Fig. 5.3.6 shows $\frac{C_p}{T}(T^2)$, while table 5.3.2 summarizes the resulting Sommerfeld coefficients, and Debye temperatures, together with the ground states and the transition temperatures for the different compounds of the series.

BaCr$_2$As$_2$ ($3d^4$) is an itinerant antiferromagnet (AFM) (120; 71) below T_N = 580 K, viz., the magnetic transition occurs much above the temperature range discussed in the work at hand. Hence, the magnetic entropy contribution associated with the magnetic transition at very high temperature can be neglected in the low temperature range and only a non-negligible electronic contribution to $C_p(T)$ at low temperature owing to the metallic

Compound	γ_{exp}	γ_{th}	Θ_D[K]	GS	Transitions
BaCr$_2$As$_2$	19.4(1)	9.3(120)	257	AFM(71)	T_N=580 K(71)
BaMn$_2$As$_2$	3.0(2)	-	261	AFM(90)	T_N=625K(90)
BaFe$_2$As$_2$	5.8(1)	7.6(3)(109; 110)	276	AFM(109)	$T_{S,N}$=136 K
BaCo$_2$As$_2$	44.2(2)	20.0(111)	287	PM	-
BaNi$_2$As$_2$	13.3(2)	9.37(111; 115)	239	SC	T_C=0.6 K, T_S=137 K
BaCu$_2$As$_2$	1.8(4)	2.96(116)	225	DM	-

Table 5.3.2.: Table 5.3.2 summarizes the experimental and theoretical Sommerfeld coefficients (γ_{exp} and γ_{th}, respectively) for each composition ($3d^4$ to $3d^{10}$), the Debye temperature (θ_D), the ground state (GS) and the experimental values for transition temperatures from magnetization and specific heat measurements. The magnetic ground state is indicated either as antiferromagnetic (AFM), paramagnetic (PM), superconducting (SC) or diamagnetic (DM). Taken from Ref. (100) (own publication).

character of the material needs to be considered in addition to the lattice contribution. A fit to the data between $T \sim$ 2-7 K yields $\gamma \sim$ 19.4(1) mJ/mol K^2, which is in good agreement with previous measurements (120; 71).

BaMn$_2$As$_2$ ($3d^5$) is reported to show a phase transition into an antiferromagnetic state at high temperature (T_N = 625 K), so that the magnetic contribution to C_p at low temperature can be neglected similar to BaCr$_2$As$_2$. A zero γ value would be expected from the semiconducting ground state probed by transport and ARPES measurements (89; 90; 121). However, we find a very small value $\gamma \sim$ 3.0(2) mJ/mol K^2 for BaMn$_2$As$_2$ in good agreement with previously reported measurements on this compound (89; 90), which probably originates from the presence of impurity states within the semiconducting gap. These impurity states may give rise to a small non-zero contribution to the electronic specific heat at very low temperatures rendering the observed non-vanishing γ to be most probably of parasitic origin.

BaFe$_2$As$_2$ ($3d^6$) is known to have an antiferromagnetic spin density wave (SDW) ground state with gapped spin excitations (Δ_SDW = 9.8(4) meV) (122), thus, in the fitted region (T $\sim$ 2-7 K), magnetic contributions to C_p can be neglected as well. From a linear fit of $\frac{C_p}{T}(T^2)$ we obtain $\gamma \sim$ 5.8(1) mJ/mol K^2 in good agreement with previous measurements. (109; 110).

BaCo$_2$As$_2$ ($3d^7$) shows a broad region of linearity characterized by a large electronic contribution, $\gamma \sim$ 44.2(2) mJ/mol K^2, which is in good agreement with literature values (111). From magnetization measurements (see Section 5.3.2) a rather constant susceptibility hints at an itinerant paramagnetic behaviour (111). Therefore, the low-temperature specific heat can be correctly approximated by Eq. 5.3.2. Note that a renormalized χ value above the

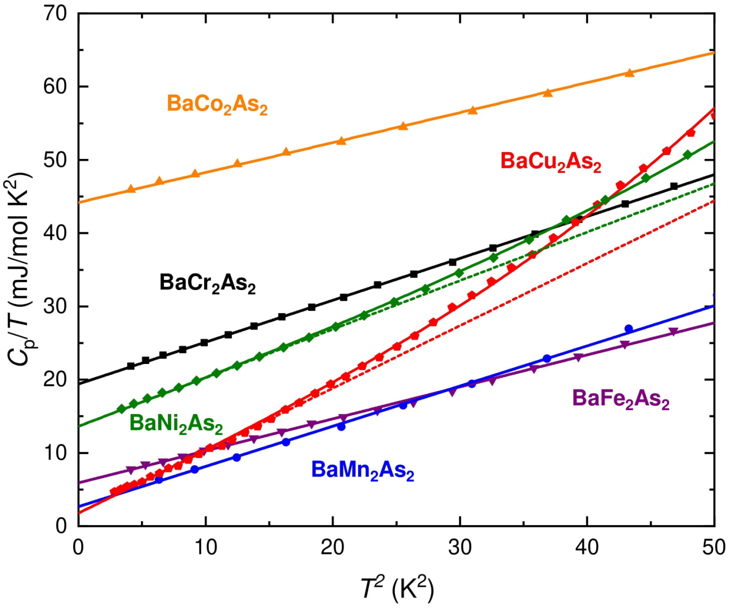

Figure 5.3.6.: Low temperature $\frac{C_p}{T}(T^2)$ for all compounds of the BaT_2As$_2$ (T = Cr, Mn, Fe, Co, Ni, Cu) series at zero external magnetic field (full symbols) together with the linear fits used to extract γ_{exp}. It has to be noted that the linearity region found for Ni and Cu compounds is reduced with respect to the other compositions, probably due to the smaller extracted Debye temperatures, θ_D. (see table 5.3.2) Therefore, for these compositions, the higher order term (δT^5) was added to the lattice contribution, thus giving a good modeling of the data up to higher temperatures. The linear contributions for these two compositions are signaled by dashed lines for comparison. Taken from Ref. (100) (own publication).

expected Pauli susceptibility suggests the presence of ferromagnetic fluctuations in the system (see Section 5.3.2), and may also influence the measured Sommerfeld coefficient.

BaNi$_2$As$_2$ ($3d^8$) undergoes a superconducting transition at T_c = 600 mK, far below the fitting region of our Cp data and has been shown to exhibit an overall itinerant paramagnetic behaviour in the normal state (see table 5.3.2), thus, not affecting the low-temperature analysis (T ~ 2-7 K) of $\frac{C_P}{T}$, which gives $\gamma \sim 13.3(2)$ mJ/mol K^2.

As previously discussed for our magnetization data in section 5.3.2, BaCu$_2$As$_2$ shows an overall diamagnetic behaviour, which would support the idea of a closed configuration of the $3d$ shells lying far below E$_F$, as supported by theory calculations (116) and ARPES measurements (70). Therefore, the low-temperature C_p can be correctly modeled by considering electronic and phononic contributions only, yielding a Sommerfeld coefficient $\gamma \sim 1.8(4)$ mJ/mol K^2. This value is very close to zero, but, since optical spectroscopy data clearly demonstrate the metallic nature of this compound (section 5.3.3), we can rule out an artificially lowered γ value due to the presence of a small bandgap down

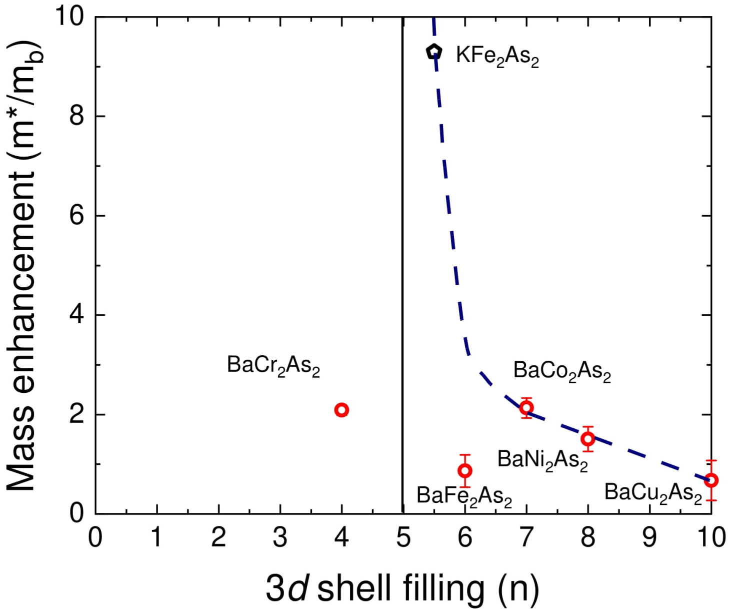

Figure 5.3.7.: Quasiparticle mass enhancement values extracted from specific heat measurements as function of the d-band filling n. The value for KFe_2As_2 from our previous work was added for comparison (79). The dashed line is a guide to the eye, which shows the general trend proposed in this work for $n > 5$. Taken from Ref. (100) (own publication).

to the resolution limit of $\sim$ 50 meV. Therefore, we conclude that the obtained value is representative of the electronic contribution of C_p.

5.3.5. Quasiparticle mass enhancement

As described in Section 2.2, the experimentally obtained Sommerfeld coefficient can be used to obtain the corresponding degree of electronic correlations by considering the proportionality to the density of states at E_F and to the effective mass of the quasiparticles, $\gamma \propto \rho(E_\mathrm{F}) \propto m^*$. The measured γ value renormalized with respect to the value from band theory calculations, obtained within the independent electron approximation, allows to estimate the presence of electronic correlations and their strength via

$$\frac{\gamma_{exp}}{\gamma_{th}} = \frac{m^*}{m_b}, \tag{5.3.3}$$

where γ_exp are the experimentally measured values, discussed in the previous section, and γ_th are the values calculated using band theory; m^* and m_b are the effective masses for the correlated system and for the free electron approximation, respectively. It has to be noted though, that in multi-band correlated $3d$ electron systems one deals with orbital-dependent effective masses, m^*. Therefore, as previously discussed in Section 5.2 and in Ref. (74), the renormalized mass enhancement extracted from specific heat ultimately represents an average over different bands of the Fermi surface (FS), only.

Fig. 5.3.7 summarizes the extracted quasiparticle mass enhancement values as a function of $3d$ band filling, while the dashed line highlights the trend proposed in the present work. For more than half-filled configurations ($3d^7$ to $3d^{10}$; viz., from BaCo$_2$As$_2$ to BaCu$_2$As$_2$) the data clearly show a monotonic decrease of the mass enhancement ($\frac{m^*}{m_b}$) upon $3d$ band filling towards the fully filled configuration realized for BaCu$_2$As$_2$ ($3d^{10}$), which shows a value close to unity reflecting a very weak degree of correlation in this compound. This is in agreement with the optical conductivity data (see Section 5.3.3). In fact, by modeling the spectra, the degree of coherence in BaCu$_2$As$_2$ appears to be further increased with respect to the coherence values reported in literature (93) for other members of the series. In order to get a more general picture of the mass enhancement in pnictides, we included the quasiparticle mass enhancement of the itinerant heavily hole-doped KFe$_2$As$_2$ with an average $3d^{5.5}$ filling, which is much higher than all other compositions of the BaT_2As$_2$ series.

It has to be noted that BaFe$_2$As$_2$ and BaMn$_2$As$_2$ significantly differ from the general trend of the mass enhancement across the series. As already discussed by Hardy *et al.* (72; 73), the opening of a spin-density wave (SDW) gap for BaFe$_2$As$_2$ decreases its DOS at the Fermi level. This results in a lowered value of the Sommerfeld coefficient ($\gamma \propto \rho(E_\mathrm{F})$), which is not taken into account in the calculated γ_th, resulting in an artificially diminished value of the mass enhancement. This is in line with our observations that BaFe$_2$As$_2$ does not follow the general trend of the series on an absolute scale. The other exception is BaMn$_2$As$_2$ due to its semiconducting ground state, rendering it impossible to extract the mass enhancement value for the $3d^5$ configuration and is thus not included in Fig. 5.3.7.

In particular, considering the (average) mass enhancement trend as visualized by the dashed line in Fig. 5.3.7, the overall monotonic increase of the electronic correlations while approaching the half-filled configuration ($3d^5$) is in agreement with the predictions by de' Medici *et al.* (63; 64), taking into account the effect of Hund's coupling in multi-band correlated electronic systems. In fact, for non negligible values of J_H, electronic correlations are expected to be maximal in close proximity to the half-filled configuration ($3d^5$) and progressively decreasing while departing from such value towards the fully filled and empty configurations for a broad region of possible U/D values (see Section 5.1). By comparing the obtained values with the quasiparticle mass enhancement of the itinerant heavily hole-doped KFe$_2$As$_2$ with an average $3d^{5.5}$ filling, it turns out that the mass enhancement is much higher in KFe$_2$As$_2$ than for all other compositions of the series BaT_2As$_2$ (T = Cr, Mn, Fe, Co, Ni, Cu), specifically ($\frac{m^*}{m_b} \sim 9.3$ (79; 74)). This may suggest that the electronic correlations could be even higher for the half-filling configuration that would be

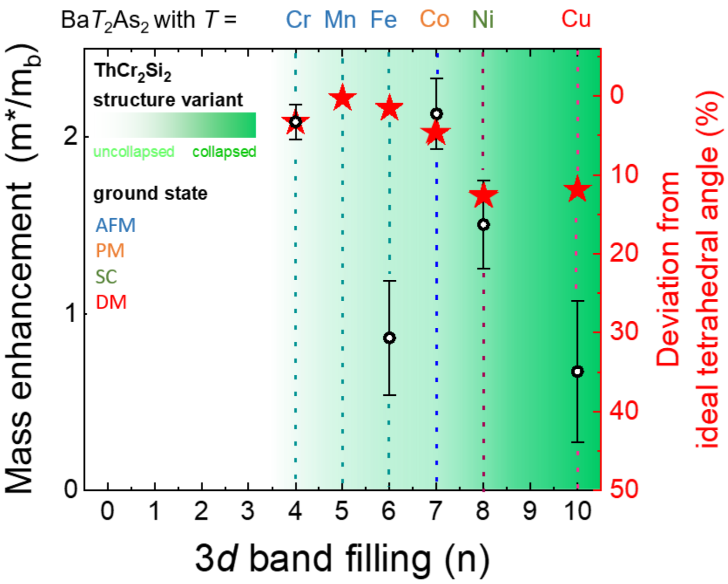

Figure 5.3.8.: Summary of the relevant parameters discussed in this work on the substitution series BaT_2As$_2$ (T = Cr, Mn, Fe, Ni, Co, Cu) as a function of the 3d band filling; for details see text and Figs. 5.3.1 and 5.3.7. Taken from Ref. (100) (own publication).

realized by BaMn$_2$As$_2$ ($3d^5$). A recent realization of the $3d^5$ configuration in a metallic material has been reported by Filsinger *et al.* for BaFeCrAs$_2$ with $\gamma \sim 65$ mJ/mol K^2 and $\frac{m^*}{m_b} \sim 5.5$ (71), supporting the prediction of strong electronic correlations in the iso-electronic BaMn$_2$As$_2$.

We observe that $\frac{m^*}{m_b} \sim 2.2$ for the $3d^4$ configuration (BaCr$_2$As$_2$), and which is of the same order of magnitude than the mass enhancement for compounds $n > 5$. According to the theoretical predictions (63; 64), electronic correlations are expected to have a rather symmetric behaviour with respect to the $3d^5$ configuration, thus decreasing from the $3d^5$ to the empty band configuration ($3d^0$). The present results from specific heat measurements, however, do not allow to unambiguously discuss the trend of the mass enhancement for less than half-filled configurations due to the limited number of compounds for $n < 5$. Therefore, other compositions in this region would be highly desirable in order to better understand the evolution of electronic correlations in multi-band 3d systems, as well as the role of the Hund's rule coupling term in iron-based superconductors.

5.3.6. Discussion

In this section, the evolution of the mass enhancement as a function of band filling ($3d^n$) will be related to the most relevant structural parameters (discussed in Section 5.3.1).

As previously discussed by Yin *et al.* (56), the mass enhancement can be related to the relevant geometrical parameters of the TAs$_4$ planes: in particular the bond angle α_{bond} and the bond length d(T-As). In fact, on the one hand, considering the Hubbard model (123), at constant values of the on-site Coulomb interaction, an increase (decrease) of the bond length reduces (increases) the hopping probability ($t_{i,j}$) between neighbouring sites, thus contributing to increase (decrease) the effective mass (m^*) of the charge carriers for a particular orbital. On the other hand, the bond angle, α_{bond}, parametrizes the shape of the tetrahedral coordination of the T atom, which determines the magnitude of the crystal field splitting (Δ) and, thus, the average occupation of the individual 3d orbitals. In fact, the crystal field is increased when α_{bond} deviates from the ideal tetrahedron (109.5°), thus determining a depopulation of the higher correlated t_{2g} orbitals in favor of the lesser correlated e_g levels.

Following from the above considerations, we will exclude the end member, BaCu$_2$As$_2$, from the rest of the discussion. In fact, given its $3d^{10}$ configuration (discussed in Sections 5.3.2, 5.3.3 and 5.3.4) the d electrons do not participate in the conductance, i.e., their effective masses are not affected by orbital overlapping or crystal field splitting.

Fig. 5.3.8 summarizes the evolution of the relevant parameters discussed in this work. As shown, the trend found for $\frac{m^*}{m_b}$ as a function of 3d filling can be traced also in the As-T-As bond angle, α_{bond}, by considering its relative difference from the ideal tetrahedral bond angle of 109.5°, proportional to the crystal field (Δ). While BaMn$_2$As$_2$ shows $\alpha_{\text{bond}} = 109.2°$, close to the ideal angle, the difference increases monotonously with 3d filling towards BaNi$_2$As$_2$ ($3d^8$), corresponding to decreasing correlations. The trends found from our data are in good qualitative agreement with the ones observed using optical spectroscopy by Yin *et al.* (56) for stoichiometric compositions of Fe-based compounds. Therefore, it is reasonable to think that the crystal field (Δ) also plays an important role in determining the magnitude of electronic correlations in this substitution series. Following from these observations, the further decrease of α_{bond} for BaCr$_2$As$_2$ ($3d^4$) can be a further hint at a decreasing trend in correlations for $n < 5$.

The bond angle close to the ideal tetrahedral angle (109.5°) for BaMn$_2$As$_2$ ($3d^5$) further supports the scenario of maximal electronic correlations for this compound. In addition, the T-As bond length shows significant changes over the substitution series. Nevertheless, for most of the compositions such difference can be reasonably explained by the progressive change in size of the transition metal, T. In fact, as previously discussed in Section 5.3.1, while for T = Cr, Fe, Co, Ni the T-As bond is comparable with the covalent radius associated with T, for T = Mn the bond length results significantly elongated. Thus, it is reasonable to think that the hopping probability between neighbouring orbitals along this bond is lower for BaMn$_2$As$_2$, leading to an increased localization and a higher effective mass of the charge carriers.

6. Revisiting the phase diagram of electron doped LaFeAsO single crystals

6.1. The nematic phase in Fe-based superconductors

As mentioned in Chapter 4, the study of the phase diagrams of different Fe-based superconductor family is important for the understanding of the interplay between the different phases. In particular, such analysis allows to understand which orderings can contribute to stabilize and which are detrimental to the superconducting phase. Fig. 6.1.1, shows a general phase diagram common to many IBS compounds. In this respect, the so called nematic phase is one of the most studied in this field, being common to the mother compounds of many families of iron-based superconductors. (124; 125; 126; 127; 128; 129)

The nematic order manifests itself as an overall breaking of the C_4 rotational symmetry within the FeAs planes, reducing to a C_2 symmetric configuration, while preserving the translational symmetry. The term "nematic" was chosen in analogy with the theory of liquid crystals, where the nematic order shows aligned the rod-like molecules along an axis called directrix, which constitutes the order parameter of such a phase. (124) Conversely, for the nematic phase in condensed matter different order parameters closely intertwined with each other have been found. Such orderings ultimately result in different anisotropic quantities in the ab plane (illustrated in Fig. 6.1.2): (i) a structural distortion from a tetragonal to an orthorhombic symmetry (134); (ii) an orbital ordering, in which the degeneracy between the d_{xz} and d_{yz} orbitals (135), lying in the ab plane is lifted, which results in e.g. anisotropic transport properties in the x and y directions (see Fig. 6.1.3); (iii) a magnetic ordering, through a stripe-type antiferromagnetic SDW phase, producing in-plane anisotropic magnetization values. (136) A phenomenological theoretical description of the nematic phase can be written through the free energy expression, using the Ginzburg-

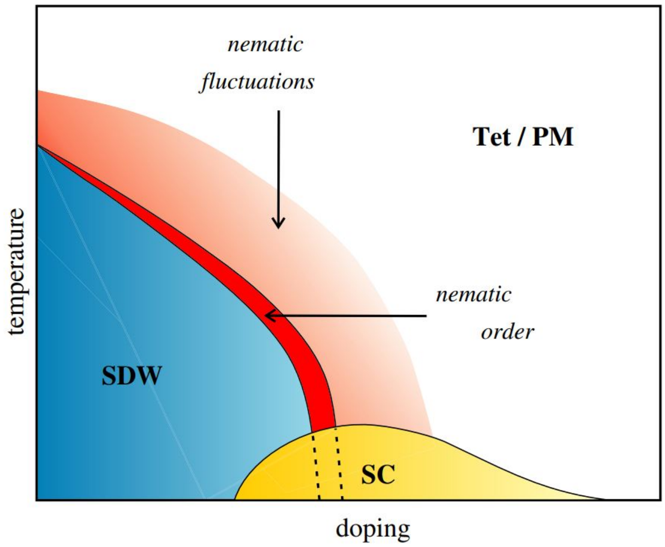

Figure 6.1.1.: Schematic phase diagram of electron doped $BaFe_2As_2$, exemplifying the different phases for iron-pnictides and emphasizing the role played by nematic order and nematic fluctuations. SDW denotes the spin-density wave state, SC the superconducting phase, PM the paramagnetic phase, and Tet the tetragonal phase. Tetragonal symmetry is only broken below the nematic/orthorhombic transition line, but nematic fluctuations remain at higher temperatures, as discussed at the end of this section, and can be probed by shear modulus (130; 131) and resistivity anisotropy (132; 133) measurements. Taken from Ref. (127).

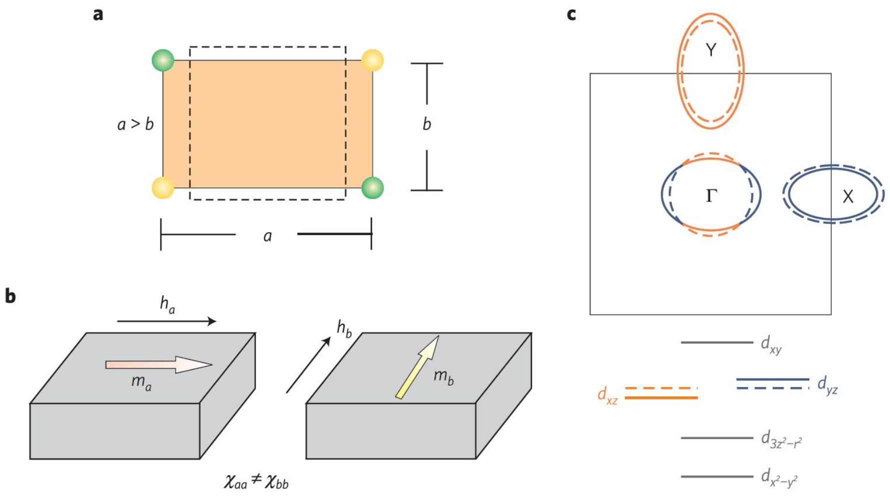

Figure 6.1.2.: Schematic representation of the different order parameters involved in the nematic phase of iron-based superconductors: (a) Orthorhombic distortion (solid line) within the *ab* plane from the high temperature tetragonal (dashed line) symmetry. (b) In-plane anisotropy in the magnetic susceptibility $\chi_{i,j} = m_i/h_j$where m_i denotes the magnetization along the i direction induced by a magnetic field h_j applied along the j direction. (c) Splitting between the d_{xz} and the d_{yz} orbitals (orange and blue lines, respectively) shown in the lower panel, corresponding to a distortion of the Fermi surface pockets. Taken from Ref. (125).

Landau approach for the order parameters (ψ_1, ψ_2, ψ_3), as

$$F[\psi_1,\psi_2,\psi_3] = \frac{1}{2}\chi_1^{-1}\psi_1^2 + \frac{b}{4}\psi_1^4 + \lambda_{1,2}\psi_1\psi_2 + \frac{1}{2}\chi_2^{-1}\psi_2^2 + \lambda_{1,3}\psi_1\psi_3 + \frac{1}{2}\chi_3^{-1}\psi_3^2 + h.o., \quad (6.1.1)$$

where the leading instability is signaled by the order parameter ψ_1, while the other ones (ψ_2, ψ_3) are coupled to the main one via the constants $\lambda_{\mathrm{i,j}}$, highlighting the interdependence of the order parameters that participate into the overall nematic phase. The inverse of the coefficients of the quadratic terms, χ_1, χ_2 and χ_3, containing the information of the temperature dependence in the Landau formula, represent the nematic susceptibility of the different orderings. (125) Presently, it is still unclear which of the order parameters is actually driving the nematic transition. Nevertheless, it appears clear that the extremely small values of the orthorhombic distortion ($\delta \sim 10^{-3}$) makes it unlikely to be the leading order for the transition. For this reason, it is often referred as electronic nematic phase. (124; 125) The electronic origin of the nematic phase was demonstrated by different experimental works. In particular, Chu *et al.* (132; 137) reported an anisotropic resistivity in strained $\mathrm{BaFe}_{1-x}\mathrm{Co}_x\mathrm{As}_2$ single crystals, showing a divergent behavior of the susceptibility of an electronic nematic order parameter at the strucural transition, proving that it is able to drive T_{S} (see Fig. 6.1.3 (a)). It is important to notice that the symmetry

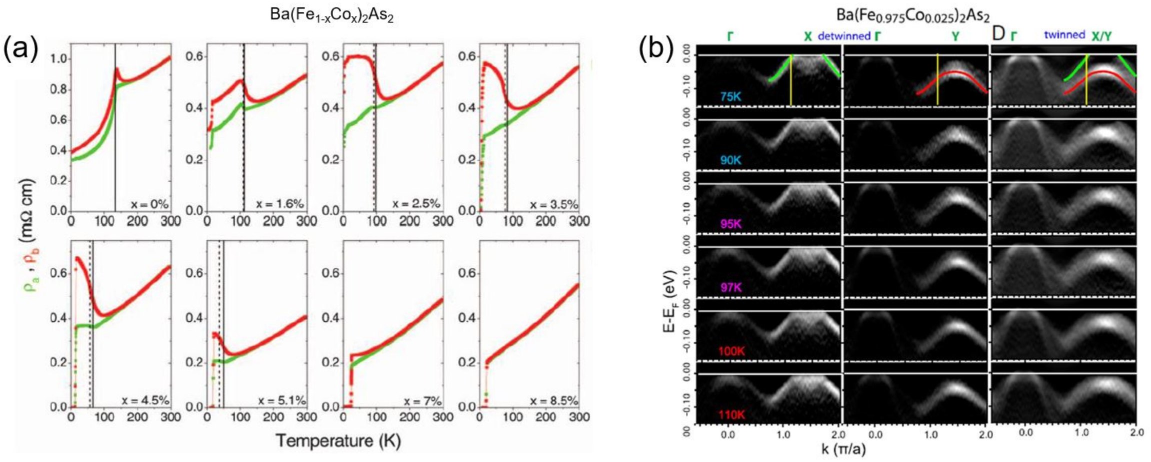

Figure 6.1.3.: Manifestations of orbital anisotropy in the nematic phase for $\mathrm{Ba(Fe_{1-x}Co_x)_2As_2}$ by the application of uniaxial strain in the ab plane: (a) resisitivity anisotropy between the a and the b axes as a function of Co doping; (b) anisotropic band splitting between the d_{xz} and d_{yz} bands in twinned sample of $\mathrm{Ba(Fe_{0.975}Co_{0.025})_2As_2}$ in the nematic phase obtained by ARPES measurements, while in the detwinned sample only one band is present for Γ-X/Y cuts of the Brillouin zone. Taken from Ref. (136) for (a) and Ref. (132) for (b).

of all order parameters is broken at the nematic transition temperature ($T_{\mathrm{nem}} \equiv T_{\mathrm{S}}$) (125), even if long-range ordering is reached at a different temperature. As an example, this happens for the magnetic instability, for which the symmetry of the spin fluctuations is already broken at T_{S}, while long-range magnetic ordering generally happens at lower temperature T_{N}. This makes more difficult to disentangle the different effects and find the leading instability in the system, while at the same time it does not allow to exclude magnetism as the main order parameter, despite $T_{\mathrm{N}} \leq T_{\mathrm{S}}$ in many systems. Therefore, two different scenarios were proposed, namely: (i) a spin-nematic scenario, which considers that anisotropic spin fluctuations associated to (and often precursing) a SDW ordering can induce nematicity; (ii) an orbital-nematic scenario, in which orbital imbalance is leading lattice and spin anisotropies. (124)

Early theoretical studies pointed out that the conventional electron-phonon coupling is not able to account for superconductivity in IBS (138) and different electron-electron pairing mechanisms were proposed. (139; 140) It is commonly believed that the fluctuations of the leading order parameter of the nematic phase, would also be the most probable candidate as the pairing glue for superconductivity in these materials. Also, whether the nematic transition is driven by charge/orbital or spin fluctuations is of primary importance for understanding the superconducting state in Fe-based SCs, in that it would give important information about the symmetry of the order parameter. (18; 141)

In particular, within the IBS family, theoretical calculations by Chubukov *et al.* (142) show that, according to the size of the electron pockets at the Fermi level, in $BaFe_2As_2$ and LaFeAsO the leading instability is expected to be a spin density wave, while for FeSe it would most probably be orbital ordering. This issue is intensively studied in IBS by means of various experimental techniques. One important way to assess this is to consider the nematic fluctuations preceding the structural transition by measuring the nematic susceptibility (χ_i) connected to the main order parameter, which can be obtained by different experimental techniques. (27) As an example, the shear modulus of many IBS was measured by ultrasound and three point bending techniques, shown in Fig. 6.1.4 (a) for $Ba(Fe_{1-x}Co_x)_2As_2$, which can be related to the nematic susceptibility. The good scaling demonstrated with the relaxation rate ($1/T_1T$) probed by nuclear magnetic resonance (NMR) measurements, representing the fluctuating response of the spin system (Fig. 6.1.4 (a)), strongly supports the spin-nematic scenario for 122 systems. (143; 27) The origin of the nematic phase in FeSe is not yet settled, since different experimental probes suggest opposite scenarios. In fact, given the absence of long-range magnetic order in this compound, it seems reasonable to think that spin fluctuations are not leading the nematic phase. From NMR measurements (144; 145; 60), the absence of spin fluctuations for $T > T_\mathrm{S}$ confirmed by the Korringa scaling found above the transition, in direct contrast to 122 compounds, suggests that spin fluctuations are not responsible for the nematic order. In a more recent work by He *et al.* on FeSe (146), short-range magnetic correlations are reported from strained magnetic susceptibility and magnetostriction measurements in the *ab* plane. This study supports the idea of a spin-nematic scenario also in 11 systems, thus pointing at a common origin of the nematic phases with the 122 compounds. Following the above argument, a recent NMR work on La1111 single crystals (147), found a very similar temperature dependence above the structural transition in the $1/T_1T$ curves of Co doped La1111 and Ba122 with similar T_S, thus suggesting spin fluctuations as the leading instability for both 122 and 1111 systems.

As a matter of fact, for real materials the nematic transition (T_nem) does not change the lattice symmetry as a whole, but tends to form structural domains of opposite orientations (twinning). As a consequence, while generally local probes (e.g. STM, ARPES, NMR) are able to resolve such domains and analyze their properties, the twinning of the lattice generally hinders the use of bulk techniques for the detection of such phase. The presence of structural domains was also proven experimentally by Tananar *et al.* using X-ray diffraction studies (148). Therefore, the application of a small uniaxial stress along the crystallographic axes related to the low symmetry phase is able to polarize the structural twins, in complete analogy with the application of an external magnetic field for a ferromagnetic material (125), as demonstrated by an early study of I. R. Fisher *et al.* (149).

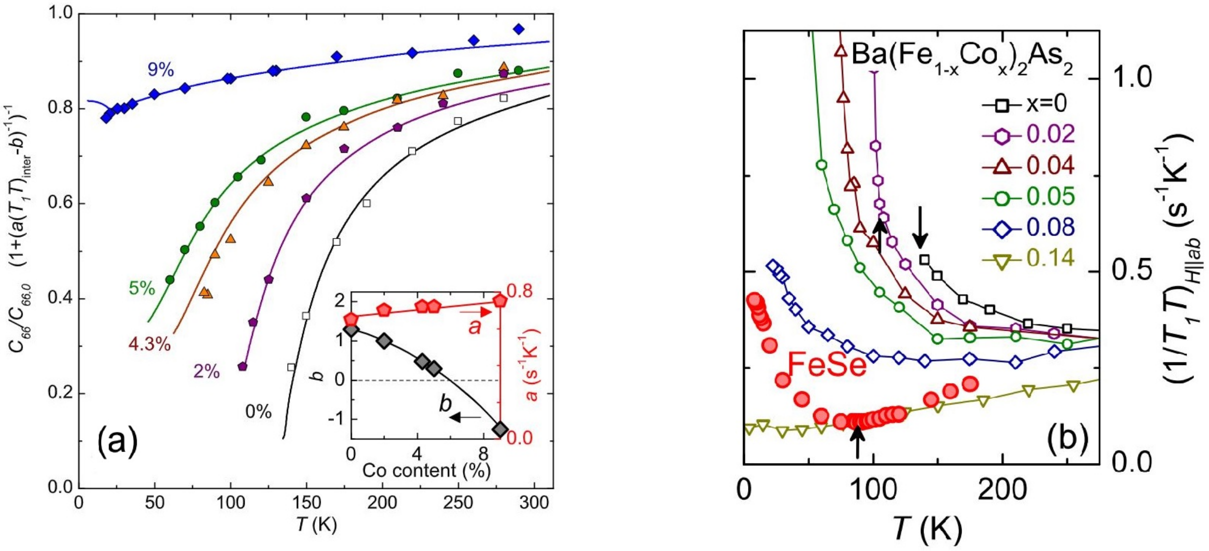

Figure 6.1.4.: (a) Scaling between normalized shear modulus ($C_{66}/C_{66,0}$) from three point bending and relaxation rate ($1/T_1T$) from NMR measurements, supporting the spin-nematic scenario for Ba(Fe$_{1-x}$Co$_x$)$_2$As$_2$. The inset shows the scaling parameters as a function of Co content. (b) Comparison between $1/T_1T$ as a function of temperature for Co doped Ba122 and FeSe. The black arrows signal the structural transitions T_S. Taken from Ref. (143).

Details on the technique used for this study are given in Section 6.3.2.

From the above considerations, it appears evident that the information about the different order parameters, being profoundly intertwined with each other, is necessary to correctly describe the behaviour of IBS. In this context, thermodynamic probes can give a comprehensive description of the macroscopic properties of these materials. In particular, by means of thermal expansion measurements, it is possible to precisely follow the temperature evolution of the orthorhombic distortion and the structural order parameter. As discussed in this section, although this order is not the leading instability, it is regarded as the hallmark of the nematic phase.

6.2. The phase diagram of 1111 systems

As already mentioned in sections 4.4 and 6.1, the precise determination of the phase diagrams of different families of IBS is of primary importance in order to investigate the nature of high-temperature superconductivity in this class of materials.

The phase diagram of electron-doped 1111 systems (e.g. Fig. 6.2.1 (a) and (b) and 6.2.2 (b)) has been extensively studied for polycrystalline samples over the past decade. (47; 150; 61; 151; 152; 153) Interestingly, this family of compounds, *RE*FeAsO

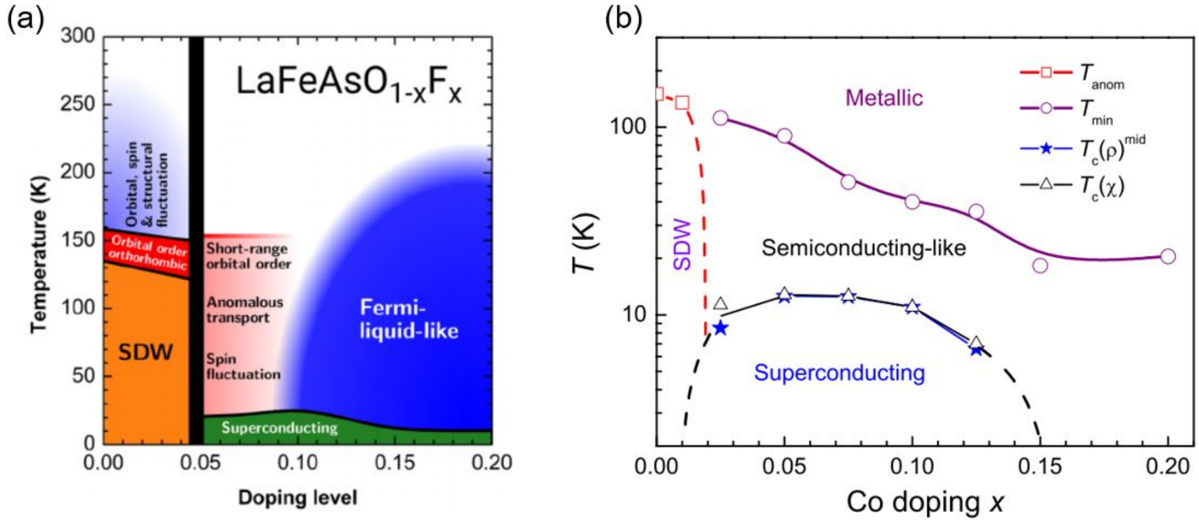

Figure 6.2.1.: (a) Phase diagram of F-doped LaFeAsO polycrystals built from different probes. Taken from Ref. (151). (b) The electronic phase diagram of $\mathrm{LaFe}_{1-x}\mathrm{Co}_x\mathrm{AsO}$. T_{anom} denotes the resistivity anomaly temperature for the SDW transition. T_{min} separates the metallic and semiconducting-like regions in the normal state of superconductors. Taken from Ref. (158).

(*RE*= La, Ce, Sm, Gd), presents all the orderings typical of the nematic phase and, different from other iron pnictides, has well separated structural and magnetic transitions, showing a broad region of electronic nematic order below ~160 K. Bulk superconductivity can be induced by a small amount of electron doping and this family constitutes the highest achieved superconducting transition temperatures (T_{c}) to date among IBS. (38; 154; 155; 156; 157) Despite the lower T_{c}, LaFeAsO proves to be particularly interesting for the study of such phenomena, because it is not influenced by an additional magnetic sublattice forming in the *RE*O layers coming from 4*f* electrons, compared to e.g., SmFeAsO. Also, compared to other *RE*1111 compounds, the nematic/orthorhombic phase is suppressed earlier and the emergence of superconductivity happens at lower doping. In fact, the magnetism of *RE* ions (e.g. Ce, Sm) is believed to stabilize the long-range SDW phase in these systems, supporting a competing interaction between magnetism and superconductivity. (159) Previous studies on La1111 polycrystals demonstrated a strong suppression of the nematic phase with increasing F doping, showing a first-order-like transition as a function of electron doping (at ~ 5%), finding a clear separation between the antiferromagnetic spin density wave (SDW) and the superconducting phase (see in Fig. 6.2.1 (a)). (159; 160; 161; 162; 163; 164; 165) This picture appears to be confirmed in the case of Co-doped LaFeAsO polycrystals, shown in Fig. 6.2.1 (b), where the SDW/nematic transitions are only observable above ~100 K and disappear already at

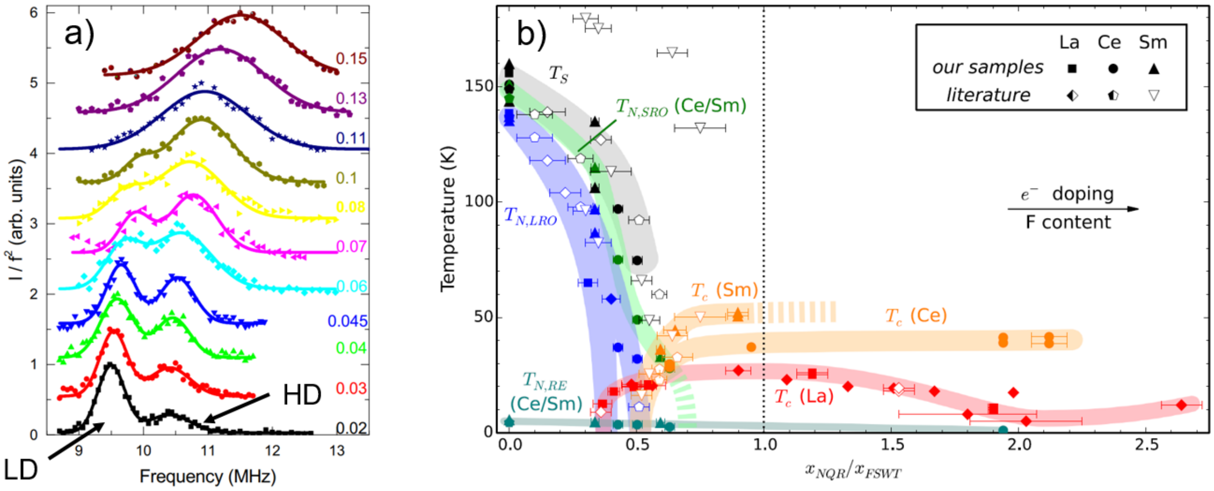

Figure 6.2.2.: (a) NQR spectra of La1111 polycrystals, showing the development of a double peaked structure upon F substitution, coming from the different electronic environments, namely high-doping-like regions (HD) at higher frequency and low-doping-like regions (LD) at lower frequencies. The lower frequency peak corresponds to the parent compound, while at higher doping levels the single peak structure is recovered, corresponding to the optimally doped composition ($x = 0.11$). Taken from Ref. (159). (b) Phase diagram of $RE\mathrm{FeAsO}_{1-x}\mathrm{F}_x$ (RE = La, Ce, Sm) as a function of $x_{\mathrm{NQR}}/x_{\mathrm{FSWT}}$, that approximate the actual electron doping level upon F substitution. The broad lines are guides for the eye. Taken from Ref. (159).

very low doping levels (< 2.5%). Superconductivity only develops above this threshold, suggesting competition between these phases. (166; 158) In this respect, the phase diagram of electron-doped La1111 seems to be rather unique with respect to other families of IBS as well as to other *RE*1111 systems. More recent nuclear magnetic resonance and nuclear quadrupolar resonance (NQR) studies (159; 160) suggest a more gradual suppression of the SDW/nematic phase in F-doped La1111 (see Fig. 6.2.2 (b)). The apparent discrepancy between these studies highlights the need of further investigations of the phase diagram of this system.

In addition, a NQR analysis of F-doped La1111 showed that for this class of compounds the electron content is not increased in a uniform way within the FeAs planes upon F doping, but instead intrinsic electronic phase separation occurs on the nanoscale, resulting in high-doping-like (HD) and low-doping-like (LD) regions. (167; 159) In fact, the NQR spectra (Fig. 6.2.2 (a)) show that, while for the parent compound a rather homogeneous electronic environment can be inferred from the single peak (LD-like) in the spectrum, as electron doping (F dopants at O sites) is introduced, one additional peak (HD-like) develops at slightly higher frequencies, signaling the simultaneous presence of two different electronic environments. With increasing doping, the spectral weight is gradually transferred to the high frequency peak, such that the full spectral transfer is then associated to the maximum in T_c (optimally doped composition). A similar behavior was recently found for Co-doped La1111 polycrystals. (168) In this way, it is necessary to estimate the actual electron transfer to the Fe sites within the *ab* plane upon $O_{1-x}F_x$ substitution, by considering the relative intensity of the HD-like peak (x_{NQR}) with respect to the value associated to the full spectral weight transfer (x_{FSWT}). It has been shown that the AFM/nematic order develops in the LD-like regions of the sample, while it is not present in the HD-like ones, which are in turn most probably hosting superconductivity. (160; 168) In this picture, the spatial prevalence of LD(HD)-like domains eventually determines the AFM (SC) ground state and it is then induced to the neighboring regions by proximity. Thus, the gradual suppression of the SDW phase and the onset of superconductivity was interpreted as related to a percolation threshold for the HD-like regions, at which bulk superconductivity can be achieved. (159) These results suggest a more complex interplay between the phases and also underline the importance of combining bulk and microscopic techniques for the study of 1111 systems.

In Section 4.4, the general phase diagrams for the 122, 11, 111 and 1111 families were introduced. It was shown in different experimental works (169; 170; 51), through the systematic comparison of many transition metal (T) substitutions in $BaFe_2As_2$, that in the 122 family of IBSs the suppression of the nematic/SDW phase is a necessary condition for the emergence of superconductivity (shown in Fig. 6.2.3 (a)). In addition, detailed thermodynamic studies of the 122 family ($Ba_{1-x}Na_xFe_2As_2$, $Sr_{1-x}Na_xFe_2As_2$, $BaFe_2(As_{1-x}P_x)_2$), revealed a multitude of new magnetic phases arising in the vicinity of the superconducting dome, thus providing further insight into the interplay of such phases with superconductivity. (171; 172; 173; 174) Therefore, in $BaFe_2As_2$-related compounds the nematic and SDW orders appear to be competing with the establishment of the superconducting phase. In fact, following the phase boundaries within the SC dome, the maximum value of T_c seems to correspond to the full suppression of the nematic order, strongly supporting the idea of nematic fluctuations as pairing glue for superconductivity. Similar approaches were successfully applied to FeSe crystals, that appear to behave differently from other Fe-based compounds and the effect of nematicity on superconductivity is still debated. As an example, in $FeSe_{1-x}S_x$ the increase of the superconducting transition temperature appears to be followed by an enhanced orthorhombic distortion, in sharp contrast to other Fe-based compounds. (60; 175; 145) Fig. 6.2.3 (b) shows the phase diagram of FeSe as a function of applied hydrostatic pressure, where interestingly the emergence of a long-range SDW ordering can be induced at $p \sim$ 1-2 GPa. In contrast, as long as a pressure induced SDW phase in stoichiometric FeSe develops (i.e. T_N increases), T_c has a plateau, while it rises

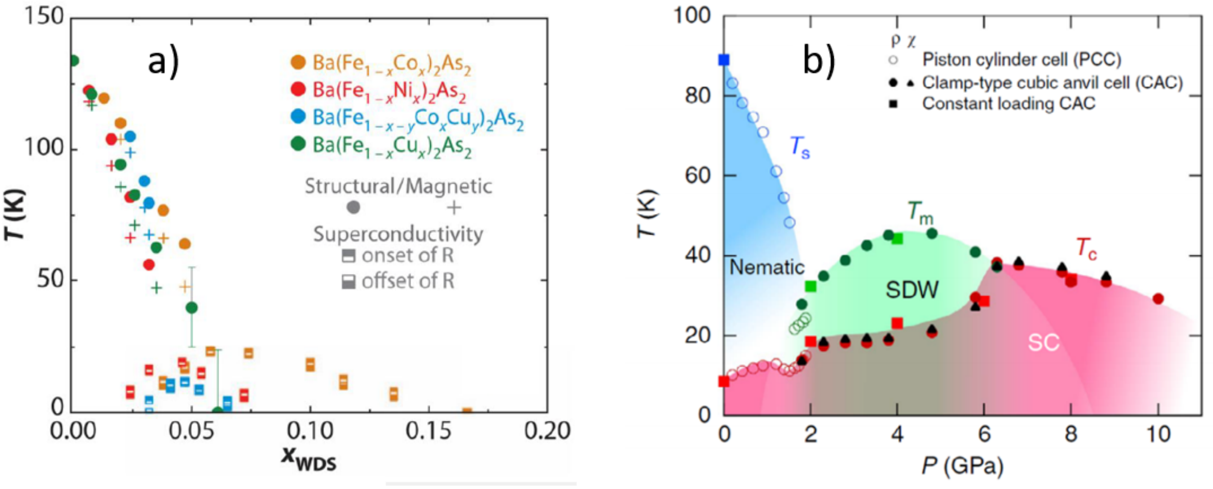

Figure 6.2.3.: General phase diagram of Ba(Fe$_{1-x}T_x$)$_2$As$_2$: (a) $T-x$ phase diagrams for Co-, Ni-, Cu-, and Cu/Co-dopings of BaFe$_2$As$_2$. Here, x represents the number of substitutional transition metal ions per Fe site. (b) $T-p$ phase diagram of FeSe as a function of applied hydrostatic pressure (p). Taken from Refs. (169; 51) and (176), respectively.

again as T_N decreases. (176) This would suggest that, while a cooperative interaction may happen between orthorhombicity and superconductivity, differently from other IBS, the latter might still compete with itinerant long-range magnetism, in accordance to what was discussed for 122 compounds. This further suggests spin fluctuations, accompanying the suppression of long range magnetism, as a possible candidate for the pairing mechanism in HTS. In this context, a precise determination of the phase diagram of 1111 systems of single crystals is highly desirable, because the understanding of the origin of nematicity and the study of its possible interplay with the magnetic and superconducting phases may give important hints on the nature of the pairing mechanism in this class of high-temperature superconductors. (171; 172; 173; 174; 60; 175; 145)

6.3. Revisiting the phase diagram of LaFe$_{1-x}$Co$_x$AsO on single crystals

In the present work, the phase diagram of Co-doped LaFeAsO was re-investigated on macroscopic faceted single crystals by means of thermodynamic probes. Magnetization and specific heat measurements were used to probe the suppression of the antiferromagnetic SDW transition as a function of nominal Co content. The direct substitution of the Fe sites by Co ions, despite inducing a higher degree of structural disorder, with respect to F doping, assures a better control on the electron doping by substituting the dopant

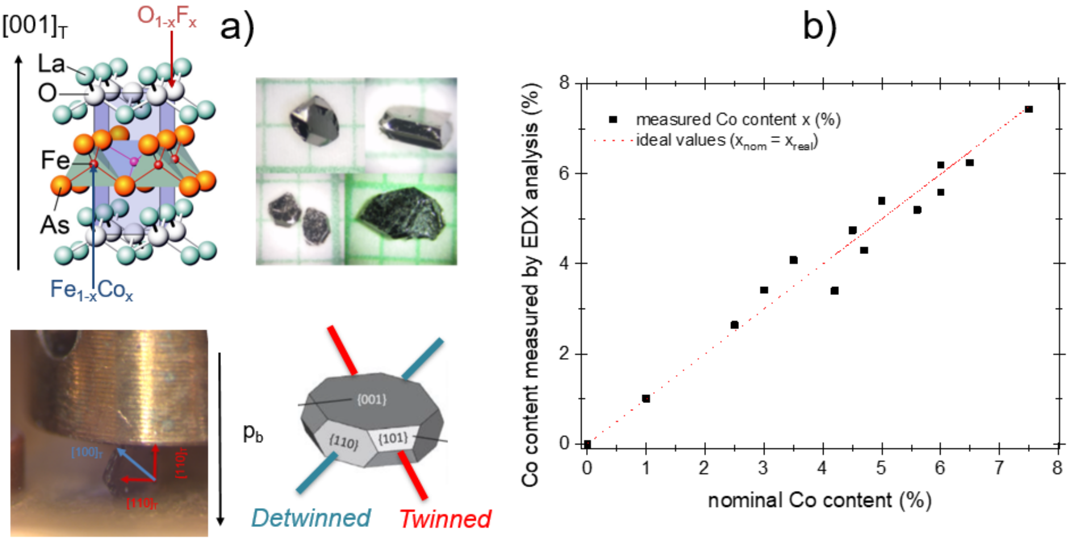

Figure 6.3.1.: (a) Crystal structure of LaFeAsO, evidencing the doping sites for in-plane Co doping and out-of-plane F doping (top-left). Images of single crystals (top-right) and crystal orientation (bottom) of the parent compound. The twinned and detwinned directions are evidenced in the picture in red and blue, respectively. Picture modified from Ref. (177). (b) Doping values determined by EDX vs nominal Co content. Taken from Ref. (178).

directly within the FeAs plane. In order to investigate the evolution of the orthorhombic distortion and to verify the presence of a long-range nematic phase particularly in the higher-doping region, the temperature dependence of the linear thermal expansion coefficient was measured in the a and b crystallographic axes for several Co doping compositions.

6.3.1. $LaFe_{1-x}Co_xAsO$ single crystals

Although LaFeAsO was the first reported compound of this class of superconducting materials, the lack of macroscopic single crystals had hindered a more comprehensive investigation of superconductivity in the 1111 family for long time. The successful growth of macroscopic faceted $LaFe_{1-x}Co_xAsO$ single crystals by Solid State Crystal Growth (SSCG) was recently reported. (177; 178) The growth process resulted in macroscopic single crystals up to a maximum size 1 x 3 x 0.4 mm^3 (shown in Fig. 6.3.1 (a) for the parent compound). As discussed in Chapter 4, most of the physical properties in IBS follow from the crystallographic structure and bonding within the FeAs planes and in particular from the Fe 3d and As 4p orbitals. Notably, one of the main difficulties encountered in studying $LaFeAsO_{1-x}F_x$ polycrystals was the precise determination of the actual electron transfer at the Fe sites as a function of nominal F substitution (see Section 6.2). Therefore, the use of in-plane $Fe_{1-x}Co_x$ substitution with respect to out-of-plane $O_{1-x}F_x$ (see Fig. 6.3.1 (a)),

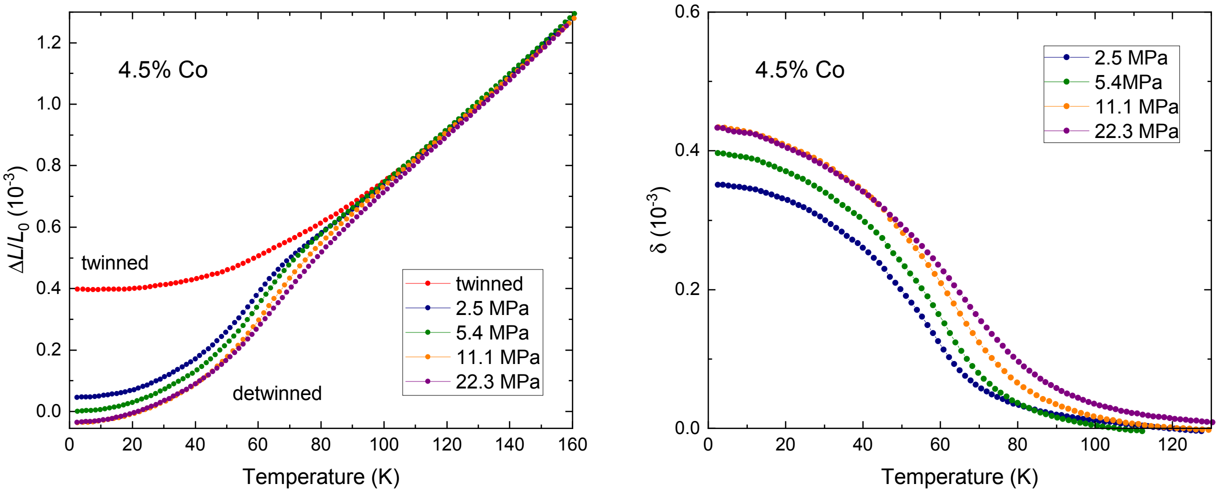

Figure 6.3.2.: (left panel) Length change of the detwinned direction ($\Delta b/b_0$) for different applied uniaxial pressures for the 4.5% Co sample. The twinned curve is plotted for comparison. (right panel) Orthorhombic order parameter (δ) calculated as a function of pressure.

although contributing to increase the in-plane disorder, assures a better control on the electron doping upon Co substitution. Co doping compositions throughout the series were measured by energy dispersive X-ray diffraction (EDX), giving a good agreement with the nominal compositions, as shown in Fig. 6.3.1 (b).

The use of single crystals is especially important for the investigation of IBSs, for which the study of the anisotropic quantities within the *ab* plane is crucial to investigate the nematic phase as a precursor to superconductivity (see Section 6.1). (179; 147; 180; 181) Fig. 6.3.1 (a) shows the orientation of LaFeAsO single crystals and the relevant orientation for thermal expansion measurements (as described in Section 3.3) are highlighted in red and blue. In particular, for the purpose of this study, the improved growth along the *c* axis with clear facets allows a more precise orientation of the crystals for thermal expansion measurements in order to resolve the small lattice distortion in the *ab* plane. Although other papers show various measurements on 1111 single crystals (182; 183; 184), a thorough investigation of the phase diagram of La1111 had not been reported in literature before.

6.3.2. Detwinning of single crystals

As discussed in Section 6.1, Fe-based materials tend order forming structural twins, therefore the detwinning of single crystals is very important in order to disentangle the anisotropic properties that characterize the magnetic/nematic phases. Due to the particular design of the dilatometer, a small uniaxial force is always applied to the sample in order to fix it to the capacitor plates. This force can be used to actively detwin the La1111 crystals, as demonstrated by previous reports for other IBSs. (172; 174; 171) By orienting the crystal in the $[110]_T$ direction in the tetragonal phase, a so-called detwinned measurement is performed yielding $\Delta b/b_0$ in the orthorhombic unit cell, while the application of a small force in the $[100]_T$ direction leads to a signal (twinned measurement) corresponding to an average of the two axes, i.e., $\frac{1}{2}\left(\frac{\Delta a}{a_0}+\frac{\Delta b}{b_0}\right)$. The length changes of the a parameter ($\Delta a/a_0$) are obtained by subtraction of the two signals (schematics of sample orientations are shown in the inset of Fig. 6.3.5 (c)). This effect can be visualized in Fig. 6.3.2, showing the length change in the detwinned direction and orthorhombic distortion as a function of pressure exemplified for the 4.5% Co sample. In fact, the overall length change for $T < T_\mathrm{S}$ increases with increasing pressure (Fig. 6.3.2 (a)). By considering the overall orthorhombic distortion, i.e. δ at $T \to 0$ (δ_0), it can be noticed that the distortion is increased with pressure, but δ_0 appears to be saturated by $p > 11$ MPa (Fig. 6.3.2 (b)). This effect can be understood as an increasing percentage of the sample is detwinned by the uniaxial pressure, while above a certain pressure value a complete detwinning is achieved.

6.3.3. Long range magnetic ordering (T_N) and superconductivity (T_c)

Fig. 6.3.3 (a)-(h) show the normalized magnetization (M/H) as function of temperature throughout the Co-doped series from the parent compound to the overdoped 7.5% Co content. The M/H curve of the parent compound LaFeAsO at $\mu_0 H = 1$ T is shown in Fig. 6.3.3 (a). At high temperatures, a linear temperature dependence is visible, well known from other families of IBSs (e.g. 122 compounds) as well as the polycrystalline samples and previously interpreted as a manifestation of short-range antiferromagnetic correlations that are still present above the nematic phase. (161) As the temperature is lowered two clear anomalies are visible in the magnetization curve below 200 K. The use of single crystals allows for an improved resolution in the measurements, while much broader transitions were observed in previous reports, as expected from the use of polycrystalline samples (161; 166; 158). The inset of Fig. 6.3.3 (a) depicts the derivative $\frac{dM/H}{dT}$, where two sharp peaks are visible at 146 K and 124 K, assigned to the structural and magnetic transitions, respectively.

Upon substituting Fe by Co atoms in the FeAs planes, the two distinct anomalies in M/H persist up to 2.5% Co content (Fig. 6.3.3 (b)), where both transition temperatures appear to be significantly lowered. It has to be noted that, while the low-temperature magnetic anomaly remains relatively sharp and clearly visible in the magnetization curve, the high-temperature structural transition appears to be progressively broadened with increasing Co content. In fact, for $0.025 < x < 0.05$ Co only one single anomaly can be discerned. Following the aforementioned observation as well as comparing with thermal expansion

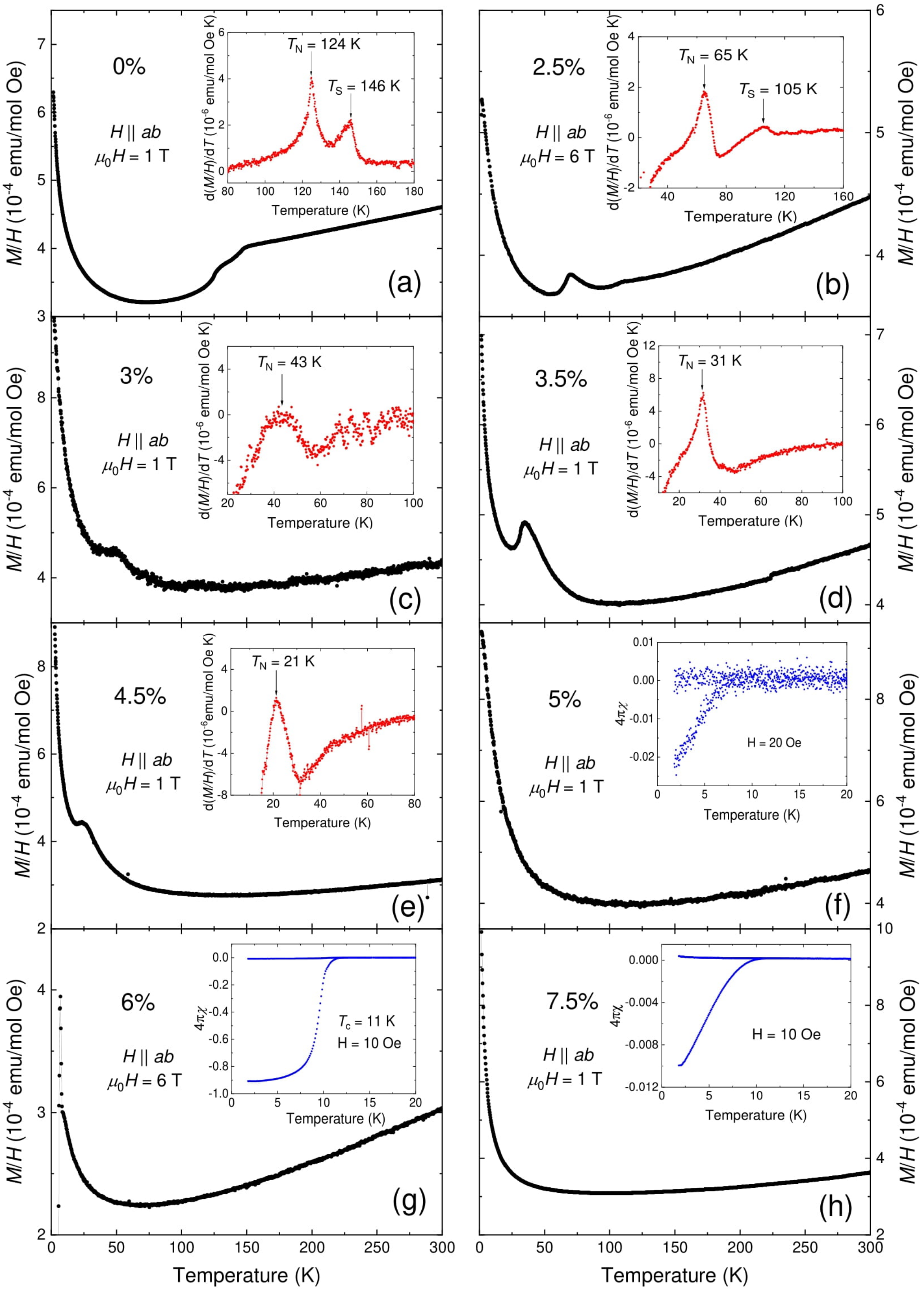

Figure 6.3.3.: Normalized magnetization M/H for the $LaFe_{1-x}Co_xAsO$ series: (a) parent compound, (b) 2.5%, (c) 3%, (d) 3.5%, (e) 4.5%, (f) 5%, (g) 6%, (h) 7.5% nominal Co content. A field of $\mu_0 H = 1$ T was applied within the *ab* plane (in some cases a field of 6 T was applied in order to improve the resolution). The insets for (a)-(e) show the temperature derivative of M/H, while for (f)-(h) the volume susceptibility is shown for $H = 10$ Oe at low temperature for both ZFC and FC measurement conditions (the higher noise level in 3% and 5% Co reflects the lower sample mass of these compositions). Taken from Ref. (185) (own publication).

measurements (see Section 6.3.4), the single peak anomalies found in the intermediate doping region have been assigned to the SDW ordering (Fig. 6.3.3 (c)-(e)). This magnetic transition temperature shows a strong and continuous lowering from ∼124 K in the parent compound to ∼21 K in the 4.5% Co doped samples, followed by a complete suppression of the anomaly for the 5% and higher Co-doped samples. These results are in good agreement with measurements of the spin–lattice relaxation rate divided by temperature ($1/\mathrm{T}_1\mathrm{T}$), which were performed on the same batch of samples (147). Notably, although T_N is gradually suppressed, the magnetic anomaly in M/H does not seem to significantly broaden with Co doping. This behavior is in agreement with the results reported by Prando *et al.* (186) for CeFeAsO, where the doping dependence of the magnetic anomaly is not changed with respect to in-plane ($\mathrm{Fe}_{1-x}\mathrm{Co}_x$) or out-of-plane ($\mathrm{O}_{1-x}\mathrm{F}_x$) substitution and the phase boundaries sit on top of each other. This suggests that the SDW instability in the 1111 family is surprisingly stable with respect to in-plane disorder.

The insets of Fig. 6.3.3 (f)-(h) show the superconducting transition for 5, 6 and 7.5% Co compositions. The transition temperatures were determined by a linear construction close to the bifurcation point between the ZFC and FC curves. Bulk superconductivity can be observed for the 6% Co sample (inset of Fig. 6.3.3 (g)), with the highest transition temperature $T_\mathrm{c} \sim 11$ K. This is in good agreement with the values previously found for polycrystalline samples. (158; 166) For the neighboring compositions a volume fraction $\lesssim 2\%$ suggests spurious superconductivity, possibly related to surface superconductivity or too small superconducting regions arising from an inhomogeneous doping distribution within the sample. The latter observation would suggests that superconductivity in Co-doped La1111 develops in a very confined doping region around 6% Co content. This scenario is supported by means of resistivity measurements as a function of temperature reported by Hong *et al.* (179) on the same batch of single crystals, suggesting a fast suppression of the superconducting phase in the immediate vicinity of the 6% composition. Also, NMR spectroscopy measurements show evidence for short-range magnetic ordering in 4.2% and 5.6% Co samples[1] , which would further support the presence of inhomogeneous behavior in this doping region. (147) It has to be noted that, while electron doping is necessary to induce superconductivity, in-plane disorder introduced by Co doping proved to be detrimental for this phase in 1111 systems with respect to out-of-plane F doping, as also demonstrated for CeFeAsO (186), showing significantly lowered critical temperatures.

Fig. 6.3.4 shows the heat capacity of some representative compositions. As introduced

---

[1] It has to be noted that in the case of 4.2% Co doping long-range magnetic ordering was also probed at lower temperature.

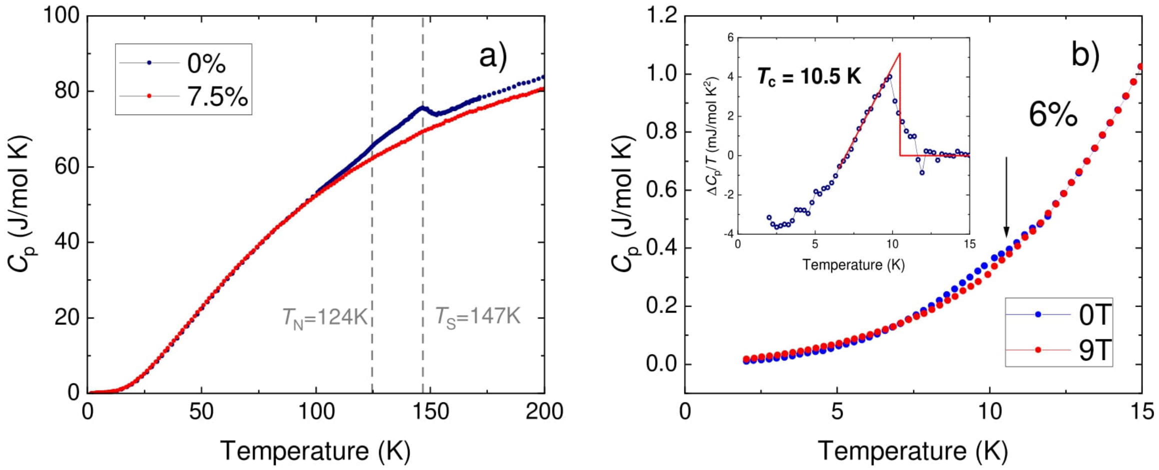

Figure 6.3.4.: Specific heat of $\mathrm{LaFe}_{1-x}\mathrm{Co}_x\mathrm{AsO}$ for (a) the parent compound and for 7.5% Co as well as (b) for 6% Co doping. The inset shows the determination of the superconducting transition temperature from the subtracted signal $\Delta C_\mathrm{p}/T = \frac{C_{\mathrm{p(0T)}} - C_{\mathrm{p(9T)}}}{T}$, approximating the specific heat contribution from the superconducting phase. Note that the offset in (a) for C_p for $T > 150$ K between the 0% and 7.5% Co is most probably due to the difference in the sample coupling at high temperature. Taken from Ref. (185) (own publication).

in Section 2.2, the total heat capacity is mainly composed of

$$C_\mathrm{p} = C_\mathrm{el} + C_\mathrm{ph} + C_\mathrm{mag}, \tag{6.3.1}$$

representing the electronic (C_el), phononic (C_ph) and magnetic (C_mag) contributions.

Fig. 6.3.4 (a) shows the heat capacity results for the parent compound and for a 7.5% Co-doped sample. The undoped LaFeAsO sample, has a clear additional contribution above the background ($C_\mathrm{el} + C_\mathrm{ph}$) for $T > 100$ K. Additional C_p contributions are mainly observed for the structural phase transition at $T_\mathrm{S} = 147$ K, while a smaller anomaly at lower temperature can be assigned to the ordering of the SDW phase at $T_\mathrm{N} = 124$ K. (177) In contrast, for the highest doped compound (7.5% Co doping), no additional entropy contributions can be recorded in C_p (see Fig. 6.3.4 (a)), signaling the suppression of the magnetic and nematic phases for 7.5% Co substitution, in agreement with the M/H measurements.

The low-temperature specific heat for the 6% Co-doped sample is shown in Fig. 6.3.4 (b) for zero field and for an external field of 9 T applied along the c axis. In order to extract the SC transition temperature, the 9 T curve was used as an approximation for the normal-state specific heat capacity for $T > 2$ K, yielding a superconducting transition temperature $T_\mathrm{c} = 10.5$ K via an entropy-conserving linear construction (see the inset of Fig. 6.3.4 (b)).

It has to be noted that an external magnetic field of 9 T shifts the superconducting transition temperature to much lower temperature $T < 2$ K, such that the electronic specific heat contribution from the superconducting phase can be neglected in the vicinity of the 0 T transition around 10 K, while the electronic and phononic terms should remain approximately unchanged by the field. The manifestation of an anomaly at T_c in the C_p studies of this composition further supports the bulk character of superconductivity. Correspondingly, the lack of a detectable anomaly in C_p for the 7.5% Co-doped sample is consistent with the very small volume fraction of SC observed in magnetization (< 2%).

6.3.4. Orthorhombic lattice distortion (T_S)

In order to probe the orthorhombic lattice distortion, thermal expansion measurements were performed on some representative compositions throughout the series, thereby extracting the relative length changes $\Delta L/L_0$ as a function of temperature, where L_0 is the sample length at 300 K. As described in Section 2.1, the linear thermal expansion coefficient can be obtained as the derivative of the length changes as

$$\alpha_i = \frac{1}{L_0}\left(\frac{\partial L_i}{\partial T}\right)_{p_i}, \tag{6.3.2}$$

where i represents the a or b crystallographic axis in the orthorhombic phase in La1111 in this work.

Fig. 6.3.5 (a) depicts $\Delta L/L_0$ for the two crystallographic directions in the ab plane. The splitting between $\Delta L/L_0$ along the a vs b directions for $T \leq T_S$ is an indicator of the nematic phase. The lattice distortion is largest for the parent compound LaFeAsO and is progressively reduced and the transition is substantially broadened by electron doping, but is still present up to 4.5% Co content. The precise determination of the transition temperatures can be obtained from the thermal expansion coefficient α (shown in Fig. 6.3.5 (b)). For the parent compound one clear anomaly can be detected at the structural transition $T_\mathrm{S} = 147$ K, followed by a smaller peak indicating long-range magnetic ordering at $T_\mathrm{N} = 124$ K. These anomalies are strongly suppressed and broadened upon Co doping, with T_S shifting from ~147 K down to ~ 60 K for samples with 4.5% Co content. In magnetization measurements (see Section 6.3.3) the structural phase transition could not be detected for $x > 2.5\%$ Co doping, pointing at a weak coupling between lattice and spin degrees of freedom together with an intrinsic broadening in temperature upon in-plane dilution with Co. In contrast, for the highly-doped 7.5% Co sample, the detwinned curve does not show any anomalous contribution above the phononic background (see Section 2.2), indicating that C_4 symmetry is maintained in the full temperature range and

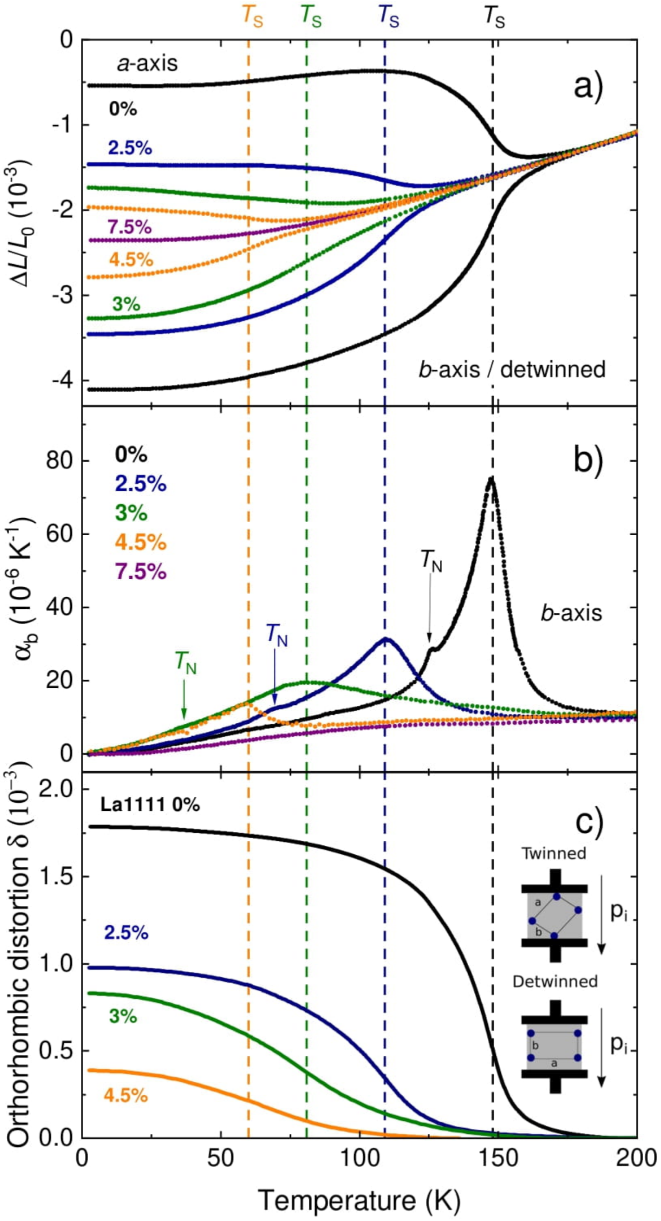

Figure 6.3.5.: Thermal expansion of the $LaFe_{1-x}Co_xAsO$ series: (a) normalized length changes $\Delta L/L_0$, (b) linear thermal expansion coefficient α_b, and (c) orthorhombic order parameter δ. The dashed lines represent the structural transition temperatures T_S for different Co contents, while the magnetic transition temperatures T_N are marked by arrows in (b). The inset of (c) shows a schematic representation of the twinned and detwinned measurement configurations. Note that the pressure applied to each crystal in the series varies due to the specific geometry and varying dimensions between sample. Taken from Ref. (185) (own publication). (2.5% and 3% Co curves measured by S. Sauerland)

that the nematic phase is completely suppressed.

Fig. 6.3.5 (c) presents the extracted orthorhombic distortion order parameter (δ). By knowing the relative length changes and the structural parameter a_0 in the tetragonal phase determined by XRD diffractometry at room temperature, the temperature evolution of the lattice parameters can be calculated. The orthorhombic order parameter is then given by

$$\delta = \frac{a-b}{a+b}, \tag{6.3.3}$$

where a and b are the in-plane lattice parameters in the orthorhombic phase. The magnitude of the distortion is progressively reduced with increasing Co content. As reported by Wang *et al.* (187), the overall distortion of 1.8 x 10^{-3} (in the limit $T \rightarrow 0$) for the parent compound is considerably smaller than the values found for other IBS. By comparing with previous works, we noted that the δ for LaFeAsO is reduced by a factor of 0.5 and 0.6 compared to $BaFe_2As_2$ (188; 171; 172) and FeSe (60; 175; 145), respectively.

Also, for all measured compositions with $x = 0$ - 4.5% Co the onset of the orthorhombic distortion happens at higher temperatures with respect to the determined T_{S} (as shown in Fig. 6.3.5 (a), (c)). In fact, for the parent compound, as shown in Fig. 6.3.5 (b), the peak associated with the structural transition in α_{b} signals T_{S}, while the transition width extends for ∼10 K above T_{S}. Such a phenomenon was also seen in polycrystalline F doped LaFeAsO samples (189; 151), interpreted as the softening of the lattice in the *ab* plane due to a precursor state of nematic fluctuations above the long-range nematic phase. In our case though, different contributions might take part in the overall broadening in temperature of the structural transition: (i) the presence of fluctuations preceeding the long-range transition, allowing a partial distortion of the tetragonal symmetry already above the transition temperature; (ii) the small uniaxial pressure applied for the thermal expansion measurement along the *b* axis used to detwin the sample[2]; (iii) ultimately, Co/Fe substitution inducing disorder in the *ab* plane. The thermal expansion coefficient was measured as a function of temperature at different applied uniaxial pressures in order to disentangle these effects as well as to verify the long-range character of the structural transition for doped compositions.

6.3.5. Pressure dependence of T_{S} and T_{N}

As discussed in Section 2.3.1, the pressure dependence of the thermal expansion coefficient in crystalline samples can be estimated making use of the intrinsic uniaxial pressure applied by the dilatometry cell. An alternative approach was presented in Section 2.3.1, in which

---

[2] Due to the sample size and geometry, the applied pressure can also vary between different compositions upon measuring.

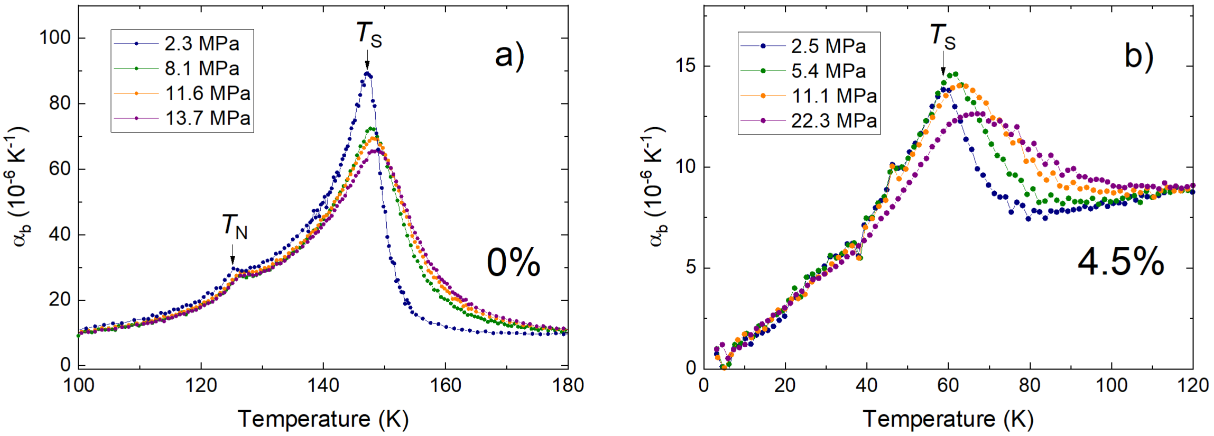

Figure 6.3.6.: Uniaxial pressure dependence of the thermal expansion coefficient in the detwinned direction (α_b) of LaFe$_{1-x}$Co$_x$AsO for (a) the parent compound and (b) 4.5% Co doping. It has to be noted that the application of increasing uniaxial pressure does not substantially increase the overall orthorhombic distortion, confirming the almost complete detwinning of the measured samples. Taken from Ref. (185) (own publication).

the pressure dependence of transition temperatures can be extracted by combining specific heat and thermal expansion measurements according to the order of the transition. In this section, the first approach will be used to qualitatively estimate the pressure dependence of T_{S}, while the Ehrenfest relation will be used for T_{N}.

Fig. 6.3.6 shows the uniaxial pressure dependence of the thermal expansion curves in the detwinned direction ($\Delta b/b_0$) for 0 and 4.5% Co doping. The structural anomaly in LaFeAsO is progressively broadened and shifted to higher temperature, as expected from the application of uniaxial pressure along the b axis. (190; 191) Notably, the same behavior can be seen for the 4.5% Co sample. In particular, by decreasing the applied uniaxial pressure (p_{b}) down to ∼2.5 MPa[3], the peak connected to the structural distortion becomes sharper, eventually resembling a λ-shaped anomaly indicative for a second-order phase transition, thus confirming the long-range character of the nematic transition in the range of 0% up to 4.5% Co doping. In order to distinguish the intrinsic behavior of the system from the external factors mentioned in the previous section (i.e. Co substitution inducing disorder and uniaxial pressure), the parent compound can be studied. This way, the effect of disorder given by Co substitution can be neglected, and the "pure" pressure dependence of α_{b} is studied. For $x = 0$, the high-T tail is strongly modified by the applied

---

[3] For 4.5% Co, the peak at the structure transition upon application of 2.5 MPa shows an artificially decreased amplitude compared to the higher pressure 5.4 MPa due to a small tilting of the sample towards the c axis, resulting from the very small uniaxial force applied. Nevertheless, for the purpose of our qualitative analysis, the curve still clearly shows distinctive features that can be correctly discussed in terms of position and width of the peak.

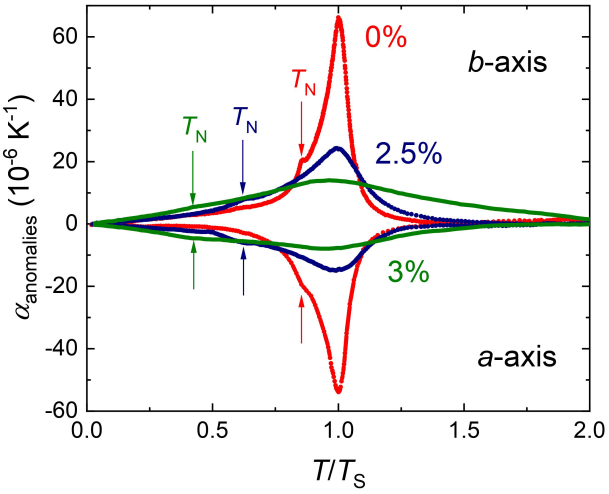

Figure 6.3.7.: Anomalies in the linear thermal expansion coefficient for the a and b axes for 0, 2.5 and 3% Co content. The non-magnetic (i.e. electronic and phononic) contribution was approximated by using the thermal expansion coefficient obtained for the overdoped 7.5% Co, which does not show any transition in any of the thermodynamic quantities under study. Taken from Ref. (185) (own publication).

uniaxial pressure as shown in Fig. 6.3.6(a), and at the lowest pressure (2.3 MPa) the tail is strongly reduced with the structural transition being considerably sharp. Therefore, the presence of a previously reported fluctuation regime above T_S cannot be unambiguously confirmed for the parent compound from this dataset. Still, as previously reported (187), the rather good qualitative agreement between the temperature dependence of δ by neutron diffraction (153) and dilatometry suggests an intrinsically broadened phase transition even for the parent compound.

As previously discussed in Section 2.3.1, the uniaxial pressure dependence of second-order phase transitions can be calculated in the limit of $p_i \to 0$ by combining specific heat and thermal expansion measurements through the Ehrenfest relation. In this case it can be applied to the magnetic transition as

$$\frac{dT_\mathrm{N}}{dp_i} = T_\mathrm{N} V_m \frac{\Delta\alpha_i}{\Delta C_p}, \tag{6.3.4}$$

where $\Delta\alpha_i$ and ΔC_p correspond to the height of the thermal expansion and the specific heat anomaly, respectively (i denotes the crystallographic direction), V_m is the molar volume, and T_N is the transition temperature into the SDW state. Fig. 6.3.7 shows a summary of the thermal expansion anomalies for the a and b axes up to 3% Co content (note that the curve for the 4.5% Co-doped sample was excluded because the magnetic anomaly found in $\chi(T)$ could not be resolved in α due to the small amplitude of the related lattice distortion).

The non-magnetic contributions (approximated by the thermal expansion curve of the 7.5% Co doped sample) were subtracted in order to obtain $\alpha_{\mathrm{anomalies}}$. In the measurements the entropy changes at the magnetic ordering temperature appear to be much smaller than at the structural transition in both C_{p} and α_i, making the determination of ΔC_{p} and $\Delta\alpha_i$ difficult on a quantitative level and subject to big uncertainties. Still, from the sign of the anomalies ($\Delta C_{\mathrm{p}} > 0$, $\Delta\alpha_a < 0$, $\Delta\alpha_b > 0$), an opposite effect can be assessed for the uniaxial pressure dependence of T_{N} in the a and b directions, i.e., $\frac{dT_{\mathrm{N}}}{dp_{\mathrm{a}}} < 0$ and $\frac{dT_{\mathrm{N}}}{dp_{\mathrm{b}}} > 0$ (see Fig. 6.3.7). Furthermore, the similar size of the magnetic anomalies in the phonon subtracted thermal expansion coefficient ($\alpha_{\mathrm{anomalies}}$) suggests that the in-plane pressure dependencies are most probably comparable in size for the a and b axis. This is in good qualitative agreement with the pressure dependence for the parent compound shown in Fig. 6.3.6, where a shift of the magnetic peak towards higher temperatures is observed with increasing pressure. Interestingly, the volume thermal expansion was previously measured on LaFeAsO polycrystals by Wang *et al.* (189), where an overall negative hydrostatic pressure dependence was determined for T_{N}.

6.3.6. Phase diagram

Fig. 6.3.8 shows the $x - T$ phase diagram of LaFe$_{1-x}$Co$_x$AsO, which summarizes the transition temperatures extracted from different thermodynamic probes, also including points extracted from NMR measurements. (147) The system proves to be very sensitive to Co doping and the transition temperatures T_{S} and T_{N} are continuously suppressed by ∼100 K up to 4.5% Co doping, while both phases are absent in the 7.5% Co-doped samples. The suppression of the magnetic SDW phase can be inferred from the disappearance of the respective anomaly in the M/H curves for $x \geq 5\%$ (Fig. 6.3.3 (f)-(h)), suggesting the full suppression of long-range magnetic order between 4.5% and 5% doping. Superconductivity was found in a small region of Co doping around 6% Co with a maximum $T_{\mathrm{c}} = 10.5$ K.

Different from our results, Wang *et al.* (158) found that in polycrystalline Co-doped La1111 the orthorhombic/SDW phase could be detected only between 0% and 2.5% Co and superconductivity develops as a separate phase for $x \geq 2.5\%$. A similar behavior was found in previous reports (61; 151) on F-doped polycrystalline samples, with a modest suppression of the long-range nematic order at (nominal) low-doping concentrations, which is lost abruptly at ∼ 5% F content in favor of a short-range nematic order and a broad superconducting dome. The apparent discrepancy with respect to our data can possibly be attributed to an increased resolution obtained by measuring single crystals directly in the ab plane, thus assessing more subtle features and anisotropies with respect to magnetic and structural changes. Also, more recent works (159; 160) reported a

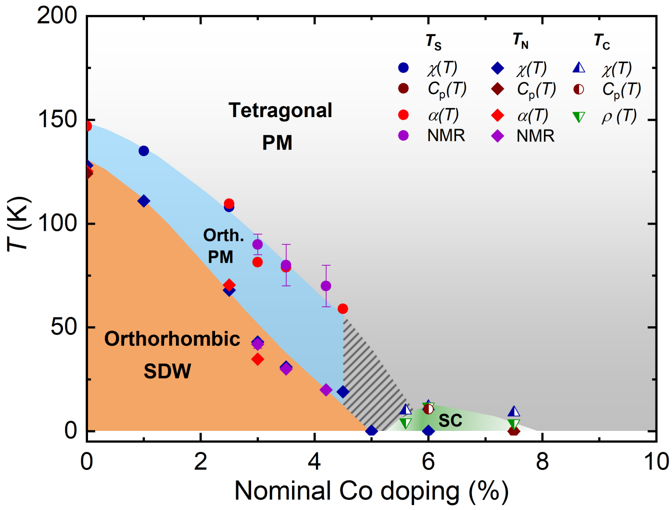

Figure 6.3.8.: Phase diagram of Co-doped LaFeAsO single crystals. Points from NMR spectroscopy and resistivity on the same series of single crystals were added from Refs. (147) and (179), respectively. The shaded area within the orthorhombic/paramagnetic phase represents the doping region (4.5 - 6% Co) where direct lattice probes are not available. The phase boundaries for the nematic state in this region are extrapolated from the data points of neighboring compositions. The color coding in the superconducting dome reflects the rapid decrease of the superconducting volume fraction estimated from magnetization measurements around the optimally doped 6% Co content, as described in Section 6.3.3. Taken from Ref. (185) (own publication).

generalized phase diagram for F-doped *RE*FeAsO polycrystals (see Fig. 6.2.1 (b)), where the actual doping content in the FeAs plane is estimated from the renormalized spectral weight transfer between different peaks in the NQR spectra. Through a careful correction of the doping content, it was shown that the SDW phase in La-based systems is actually also gradually suppressed with increasing doping. Furthermore, no coexistence between superconductivity and long-range magnetism was observed. Both of these conclusions are in good agreement with the data reported in this work.

The suppression of the magnetic SDW phase by ∼5% Co is also in agreement with a recent publication by Hong *et al.* (179) about elastoresistance (ER) measurements on the same batch of Co-doped single crystals as in this work (shown in Fig. 6.3.9 (b)). Specifically, the ER curves reveal a local maximum in the nematic susceptibility (χ_{nem}) around 4% Co content, which may be explained by enhanced fluctuations in the vicinity of a possible quantum critical point. Fig. 6.3.9 (a) shows a recent comparison between F- and Co- doped LaFeAsO phase diagrams (the latter corresponding to Fig. 6.3.8), from which it is clear that a neat separation between the long-range magnetic and the superconducting phases was determined for both substitutions.

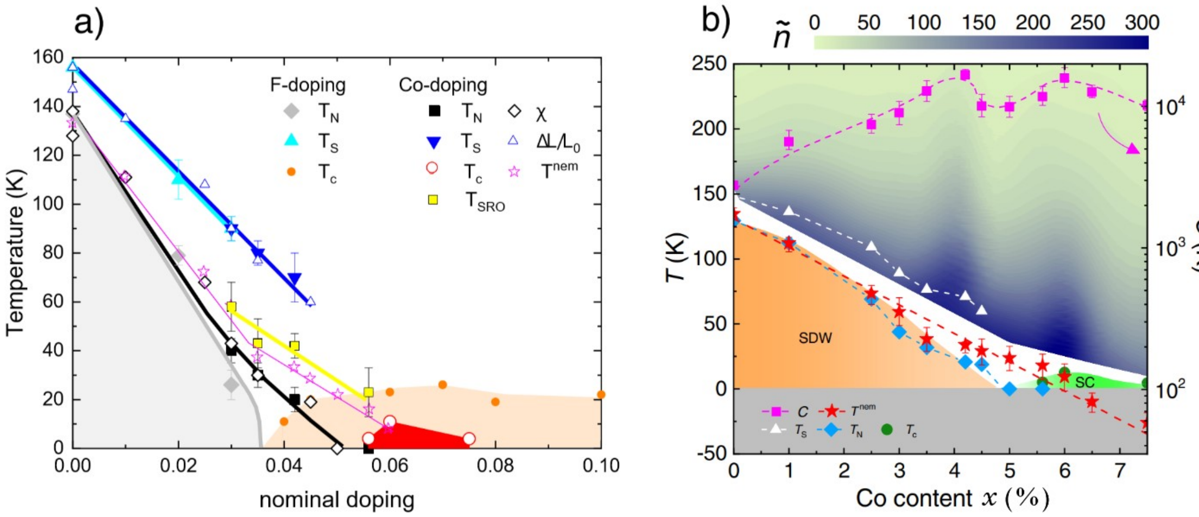

Figure 6.3.9.: (a) General phase diagram of LaFe$_{1-x}$Co$_x$AsO single crystals derived from NMR measurements. Taken from Ref. (147). (b) Nematic susceptibility ($\tilde{n}$ in the graph) as a function of temperature and Co doping obtained from measurements of elastoresistance (ER). Taken from Ref. (179). The nematic temperature (T_{nem}) extracted from ER curves is reported in both graphs in pink and red stars respectively. Points from thermodynamic probes described in this work are reported for comparison.

Thermal expansion measurements (see Sections 6.3.4 and 6.3.5) suggest that a long-range orthorhombic distortion can be clearly detected until 4.5% Co doping, while it is completely suppressed in the overdoped region at 7.5% Co doping. Nevertheless, it is still unclear if the long-range structural order can be sustained for the compositions in the vicinity of the superconducting dome, i.e. for $0.045 < x < 0.06$, and whether such lattice distortion would still be present after the suppression of the SDW order (i.e. $0.05 < x < 0.06$). As discussed in Section 6.2, NQR measurements of F- and Co-doped La1111 show an intrinsic electronic phase separation at the nanoscale into high-doping-like (HD) regions, hosting superconductivity, and low-doping-like (LD) regions, in which SDW/nematic order develops. The spatial prevalence of one type of "domain" over the other would ultimately determine the ground state of the system. In this case, sizeable crystals suitable for thermal expansion measurements are still missing for the doping region $0.045 < x < 0.075$, thus T_S could not be probed in this doping region so far. Therefore, it is still unclear if the long-range structural order can be sustained for the compositions in the vicinity of the superconducting dome around 6% Co, and whether such lattice distortion would still be present in the non-magnetic state. On basis of these results and of literature, it is probable that the long-range character of the nematic order would be lost above a certain Co concentration, corresponding to the spatial growth of the HD-like

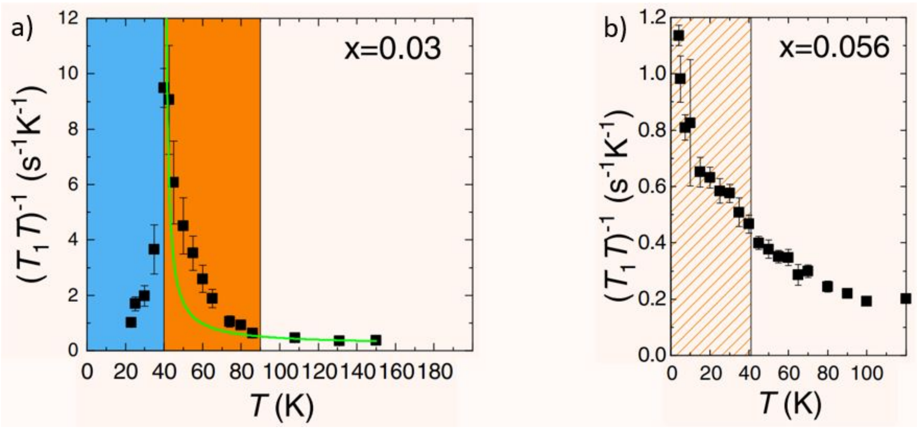

Figure 6.3.10.: NMR measurements on Co-doped single crystals for two exemplary compositions. Relaxation rate $(1/T_1T)$ for $x = 0.03$ (a) and $x = 0.056$ samples. Different colors are used to mark different phases in the plots: in the left panel, the orange area denotes the nematic/paramagnetic and the light blue one signals the temperature region where both long-range magnetism and nematicity are present; in the right panel the shaded area marks the region where only short-range correlations are possibly present. Taken from Ref. (147).

regions for $x \geq 5\%$ Co (shaded area in Fig. 6.3.8). This scenario is supported by recent NMR measurements, showing a reduction of nearly a factor 10 in the dynamic response of the spin-system between the 3% sample (Fig. 6.3.10 (a)), where long-range T_N was seen in χ and T_S via thermal expansion (see Section 6.3.3) and the 5.6% composition, where no long-range order was detected, and this was interpreted as a manifestation of short-range correlations in close proximity to the bulk superconducting composition (6% Co). (147)

Differences and similarities can be found with other families of IBS: (i) the substantial phase separation between long-range magnetism and superconductivity is in sharp contrast to a rather broad coexistence region found for 122 compounds, e.g. $Ba(Fe_{1-x}Co_x)_2As_2$ (192; 47; 193); (ii) on the other hand, although clear thermal expansion measurements in proximity to the optimally doped 6% Co sample are still missing, the phase boundaries derived for the neighboring compositions suggest an overall competing interaction between long-range nematic order and superconductivity, as also suggested by Hong *et al.* (179), in contrast to what was found for S-doped FeSe. Ultimately, the above conclusions on the LaFeAsO phase diagram, despite some clear differences (i.e. mainly related to the intrinsic nanoscopic electronic phase segregation probed by NQR), also highlight the presence of many common features (e.g. a gradual suppression of the long-range SDW/nematic phase) with other families of IBSs (e.g. $BaFe_2As_2$ and FeSe) as well as with other REFeAsO, while previous studies hinted at a rather unique and peculiar behavior of electron doped LaFeAsO with respect to other similar systems (see Section 6.2). (151)

7. Summary

This PhD dissertation focuses on the investigation of two important aspects for iron-based superconductors (IBSs), that are believed to be strictly connected with the phenomenon of high-temperature superconductivity, namely the determination of the degree of electronic correlations and the study of precursing phases in close proximity to superconductivity. The study is conducted on two of the most prominent families of Fe-based compounds (named after their stoichiometry), namely 122 systems, closely related to $BaFe_2As_2$, one of the most studied of IBS, while the second part is focused on LaFeAsO, that, despite being the first discovered compound of this class of materials, still presents some open questions regarding the evolution of the nematic and magnetic phases as a function of electron doping.

In Chapter 5, a systematic analysis of magnetic and electronic properties of a series of $\mathrm{Ba}T_2\mathrm{As}_2$ (T = Cr, Mn, Fe, Co, Ni, Cu) single crystals is presented in order to investigate the evolution of electronic correlations as a function of the $3d$ band filling. Magnetic susceptibility was used to determine the magnetic ground state of each of the compounds in the series. In particular, by the comparison with optical spectroscopy, used to assess the electronic ground state, the diamagnetic metallic nature of the end member compound $BaCu_2As_2$ was established, thus giving a rather surprising $3d^{10}$ configuration for this compound. In order to estimate the electronic correlations in the system, the Sommerfeld coefficients (γ) have been extracted from the low temperature $C_\mathrm{p}(T)$ and, by comparing the experimental γ values with calculations, the mass enhancement over band theory values was estimated for the full series. A clear decrease in $\frac{m^*}{m_b}$ can be seen for more than half-filled electronic configurations, ranging from $3d^7$ ($BaCo_2As_2$) to $3d^{10}$ ($BaCu_2As_2$), in agreement with theoretical predictions. Though not directly measurable by this method due to the semiconducting ground state of $BaMn_2As_2$ ($3d^5$), the overall trend for $n > 5$, together with the modest degree of correlations for $BaCr_2As_2$ ($3d^4$) suggests maximal correlations for the half-filled configuration ($3d^5$). Such conclusion is supported by theory but its experimental realization is still under debate. Finally, the determined trend in electronic correlation was related to the structural parameters, in particular the T-As bond length (d_{T-As}) and the As-T-As angle (α_{bond}). The bond angle (α_{bond}) is close to the perfect tetrahedral angle (109.5°) for $BaMn_2As_2$, while it progressively departs from this value for the other compositions, determining an increase of the crystal field splitting (Δ), thus reducing electronic correlations as reported by Yin *et al.* (56). Furthermore, the elongated bond distance (d_{T-As}) with respect to the covalent radius found for $BaMn_2As_2$, together with the almost perfectly tetrahedral bond angle (α_{bond}), further suggest a maximum in electronic correlations for the $3d^5$ configuration. In this context, analogous compounds for less than half-filled $3d$ bands configurations would be desirable, in order to relate the trend of experimentally extracted mass enhancement with theoretical predictions also for $n < 5$.

In Chapter 6, the phase diagram of macroscopic faceted Co-doped LaFeAsO was revisited on single crystals by thermodynamic probes. The determined phase diagram proves to be substantially different from other families of Fe-based superconductors, as well as from previously reported phase diagrams obtained by measuring polycrystalline samples. In fact, for the parent compound, clear magnetic and structural transitions can be distinguished. The long-range spin density wave phase was found to be completely suppressed for 5% Co content, while superconductivity develops in a narrow doping region around 6% Co doping, thus showing no evident coexistence between the two phases, contrary to what was observed for 122 systems. In addition, the use of single crystals allowed to assess the small orthorhombic distortion caused by the nematic ordering by means of high-resolution capacitance dilatometry. These studies reveal a continuous reduction of the structural transition temperature T_{S} upon doping up to 4.5% Co and a complete suppression for 7.5% Co doping, in contrast to previous reports on F/Co doped La1111 polycrystalline samples, where a first-order-like suppression of T_{S} and T_{N} was found. For future works, it will be interesting to investigate the behavior of the nematic phase in close proximity to the superconducting dome in single crystals of Co-doped La1111, in order to further clarify the interplay between these phases (for which this and previous studies suggest an overall competitive interaction), as well as to compare these results with other doping variants on single crystals, e.g., out-of-plane F doping in La1111. Such a comparison could also lead to a better understanding of the general pairing mechanism of superconductivity in iron-based compounds.

In conclusion, the examples presented in this thesis show that the study of the normal-state properties as well as of the precursing phases in close proximity to superconductivity is of primary importance in order to understand the origin of high-temperature superconductivity in Fe-based materials.

List of Figures

2.2.1. Schematic representation of the different C_p components as a function of temperature. The dashed line represents the low temperature linear fit of $C_\mathrm{p} \sim \gamma_\mathrm{n} + \beta\, T^2$, where the intercept is the Sommerfeld coefficient (γ_n). As typical of many materials the experimental fit deviates from the linear approximation around $T \sim 10$ K. Taken from Ref. (12). 10

2.3.1. (a) Temperature dependence of the order parameter of the Landau theory $|\psi|$ with transition temperature $T = T_\mathrm{c}$. (b) Free energy (F) as a function of the real part of the order parameter. The graph distinguishes between different values of the parameter α, from which it is clearly seen that F has minima for $|\psi| \neq 0$ only if $\alpha < 0$. Taken from Ref. (15). 15

2.4.1. $H-T$ phase diagram of a type I (a) and type II (b) superconductor. For type II superconductors the different phases are highlighted as the mixed phase (Abrikosov) for $H_\mathrm{c1} < H < H_\mathrm{c2}$ and the Meissner phase for $H < H_\mathrm{c1}$. Taken from Ref. (10). 17

2.4.2. Pairing state symmetries of Cooper pairs in the Fermi surface for (a) cuprate and (b) iron-based superconductors. In both graphs, the shown pairing refers to the spin-fluctuation based pairing, which will give a *d*-wave symmetry for cuprates and a nodeless s^{+-} symmetry for IBSs. Taken from Ref. (18). 19

3.1.1. Schematic representation of the detection system in the MPMS3 by Quantum Design connected to the SQUID sensor. The detection coils are marked as '+' or '-' to underline their opposite winding and the output voltage signal, obtained by moving the sample through all of the coils (i.e. corresponding to the DC mode described below), is shown aside. Taken from Ref. (19). 24

3.1.2. Measurement principle of the SQUID detection: (a) schematic representation of the SQUID sensor; (b) voltage vs current characteristic for a single Josephson junction (left panel), where the applied bias current (I_{B}) is chosen to be lower than the critical current of the superconductors. Voltage output of the SQUID sensor as a function of the magnetic field through the ring. Taken from Ref. (20). 25

3.2.1. Measurement principle and schematic experimental setup for measuring heat capacity through the relaxation method: (a) time evolution of the heat pulse applied to the platform and the temperature measured by the platform thermometer. The time constant τ is proportional to the specific heat of the sample. (adapted from Ref. (23)); (b) schematic representation of the measurement setup used in this thesis, where the different terms in Eq. 3.2.1 are highlighted (adapted from Ref. (23)); (c) side view of the measurement platform from Quantum Design. The different components are marked with the same colors as in (b). 28

3.2.2. Expanded view of the different components of the specific heat measurement puck for the PPMS and its connection to the Model 6000 electronics. Taken form ref. (23). 30

3.3.1. Experimental setup of the capacitance dilatometer used in this work: (a) schematic representation of the dilatometry cell, in which the applied uniaxial pressure necessary to fix the sample to the movable part of the device is highlighted (adapted from Ref. (27)); (b) 3D model of the dilatometer (Küchler - Innovative Measurement Technology) showing the different components corresponding to the upper scheme (adapted from Ref. (28)); (c) insert adapted for the dilatometer for the use in the PPMS cryostat by Quantum Design (taken from Ref. (28)). 31

3.3.2. Displacement of the movable capacitance plate (Δd) of the reference Cu sample as a function of temperature used to estimate the cell expansion background. The graph compares different Cu samples used for this work (L = 1.015 mm and L = 0.541 mm). The curves for each length are on top of each other and a feature is visible at T = 250 K, higher than the relevant temperature range for the measured samples (T < 200 K). 33

3.3.3. Schematic representation of the three terminal capacitance measurement circuit: representation of the configuration (left panel) and equivalent circuit (right panel) of the three capacitors. Taken from Ref. (32; 33). 34

3.3.4. Effect of varying the pressure exerted to the sample by the dilatometer: (a) displacement of the movable capacitance plate and applied force as a function of the measured external capacitance; (b) Force applied to the sample as a function of the displacement from which the overall spring constant was estimated as $D = 24291$ N/m. Taken from Ref. (28). 35

4.1.1. Evolution of the maximum critical temperatures (T_c) reached over the years for the main families of superconductors. Taken from Ref. (37). 40

4.2.1. (a) Crystal structures of the main families of IBS in the tetragonal unit cell. (b) The main building block is constituted by the FePn/Ch layers, denoted in red-green and red-yellow, respectively. The FePn/Ch layer is depicted from the side (upper panel) and from the top (lower panel) and the unit cell in the *ab* plane is delimited by the dashes line. The spin arrangement in the SDW phase is indicated in the lower panel, highlighting the anisotropy of the spin system. Taken from Ref. (48). 41

4.2.2. (a) Band dispersion along the Γ-M direction in the Brillouin zone calculated by LDA approximation for NaFeAs. The right panel illustrates the main orbital characters of the bands crossing the Fermi level. (b) General Fermi surface topology of iron-based compounds. A schematic 3D representation of the main bands involved is shown in the lower panel. Taken from Ref. (49). 41

4.3.1. (a) Mass enhancement $\frac{m^*}{m_b}$ of the iron $3d$ orbitals in the paramagnetic state calculated by DFT+DMFT calculations. For comparison, the low-energy effective mass enhancement obtained from optical spectroscopy experiments and angle-resolved photoemission spectroscopy experiments are added to the plot. (b) Relevant in-plane structural parameters for different iron-pnictides/chalcogenides. The green line denotes the angle corresponding to an ideal (undistorted) tetrahedral configuration. Taken from Ref. (56). . . 42

4.4.1. Phase diagrams of exemplary compositions of 122, 11 and 1111 compounds. (a) Co-doped $BaFe_2As_2$ shows gradual suppression of the orthorhombic/SDW phase and microscopic coexistence between such phase and superconductivity. Taken from Ref. (60). (b) In S-doped FeSe upon the suppression of the nematic phase T_c is lowered accordingly, suggesting a cooperative interplay between the two phases. Taken from Ref. (60). (c) Phase diagram of the F-doped LaFeAsO showing a sudden transition between the nematic/SDW and SC phase, giving rise to a broad superconducting dome. Taken from Ref. (61). 44

5.1.1. Schematic representation of the energy levels involved in the formation of a Mott-insulator from a single-band metallic system. Adapted from Ref. (62). 48

5.1.2. Color coded plot of the quasiparticle weight Z in a model with 3 orbitals, for $J_{\mathrm{H}}/U = 0.15$, as a function of the Coulomb potential, U, and the number of electrons per site, i.e. empty ($n = 0$) to full orbitals ($n = 6$). Darker regions correspond to good metals and lighter regions to bad metals. The black bars signal the Mott-insulating phases for integer filling, while the white arrows denote the expected evolution of U_{C} upon increasing J_{H}. It has to be noted that for 2 electrons (2 holes) orbital filling a bad-metal behavior is present for a wide range of U/D values, i.e. high correlations while a rather metallic ground state is preserved. Specific materials are schematically placed on the diagram and signalled by gray crosses. Taken from Ref. (64). 49

5.1.3. (a) Sketch of some of the most probable configurations in electron- and hole- doping in 122 iron-pnictide systems. Here n indicates the electronic filling normalized to the total number of electrons in $3d$ orbitals and S is the total spin. (b) Mass enhancement values calculated for different orbitals as a function of $3d$ orbital fillings, where the 0 doping represents the $3d^6$ configuration of $BaFe_2As_2$. Taken from Ref. (65) and (64), respectively. . . 50

5.1.4. The density of states for the Fe $3d_{z^2}$ (left) and $3d_{xy}$ (right) orbitals for the simulated $CsFe_2As_2$ compound with stretched a axis as a function of the on-site Coulomb repulsion U and Hund's coupling J_{H}. Taken from Ref. (65). 51

5.1.5. Coherence to incoherence crossover anomaly at T* $\sim$ 120 K from different thermodynamic probes for the highly correlated KFe_2As_2 compound: (a) Magnetic susceptibility M/H measured for H$\perp$c and H$\|$c in different magnetic fields (solid lines). The symbols shows the temperature dependence of the intrinsic susceptibilities χ_c(T) and χ_{ab}(T) derived from magnetic isotherms (Honda-Owen analysis). (b) Temperature dependence of the electronic contribution of the linear thermal expansion coefficient ($\frac{\alpha_e}{T}$), showing a similar peaked feature. (c) Low-temperature in-plane electrical resistivity ρ_{ab} as a function of T^2. The solid line is a fit to a Fermi liquid behavior, $\rho_0 + AT^2$. The inset shows the temperature dependence of $\rho_{\mathrm{ab}}(T)$ up to 300 K. Taken from Ref. (66). 52

5.2.1. Sommerfeld coefficient γ_n (blue symbols) and the residual electronic density of states, $\gamma_r = \lim_{T\to 0} \frac{C_e}{T}$, in the superconducting phase (green symbols) for $Ba_{1-x}K_xFe_2As_2$, $Ba(Fe_{1-x}Co_x)_2As_2$ and AFe_2As_2 (A = Rb and Cs). The red stars represent density functional theory+slave spin (DFT+SS) calculations for the tetragonal paramagnetic phase, while the black dots represent the DFT calculation only, which does not account for electronic correlations in the system. The magenta area indicates the loss of density of states due to the reconstruction of the Fermi surface in the SDW phase. Taken from Ref. (73). 55

5.2.2. Experimental values of mass enhancement in the vicinity of $BaFe_2As_2$ assessed by different techniques (72; 75; 76; 77; 78; 79; 80; 81; 82; 83; 84; 85; 86; 87; 88).The experimental phase diagram, including the antiferromagnetic metallic (AF) and the superconducting (SC) phases is shown as a background for comparison. The solid line is a fit of the mass enhancement determined by specific heat data. ARPES and quantum oscillation data corresponding to a given doping represent the values estimated for the different sheets of the Fermi surface, while the red squares labelled as "ARPES whole" represent the average value of the single bands (red crosses). It is clearly seen that electronic correlations increase monotonically as the filling is reduced towards the half-filled configuration and the values from different techniques spread more and more, stemming from an enhanced orbital differentiation (OSMT). Taken from Ref. (74). 56

5.2.3. Color coded map for the mass enhancement of T-pnictides as a function of Pn-T-Pn α_{bond} and electron filling of T d orbitals in the T^{2+} state. Blue lines indicate the doping compositions between two of the studied compounds: the solid lines denote the superconducting compositions while the dotted lines the non-superconducting ones. It is clearly seen that for $BaMn_2As_2$ ($3d^5$) α_{bond} is closest to the ideal tetrahedral angle of 109.5° and at the same time shows stronger electronic correlations, hinting at a non-negligible influence of the crystal structure in this respect. Correlation strength is schematically represented by the indicated color map. Taken from Ref. (93). 57

5.3.1. Selected structural parameters as a function of the d-band filling in BaT_2As$_2$: (a) The lattice parameters a, b (left axis, black), and c (right axis, blue) for the tetragonal unit cell. (b) The bond distance between transition metal T and As d(T-As) (left axis, black). For comparison, the evolution of the covalent radius (94) (right axis, blue) as a function of T is shown. (c) The angle α_{bond} in As-T-As. In (a), black and blue dashed lines are guides to the eye. Red dotted lines in a and b indicate the linear trend observed for T = Cr, Fe, Co. The uncertainty of the experimental values is of the order of the size of the data points. Lattice parameters for T = Fe are adapted from Ref (95). For literature values, see T = Cr, Co (96), T = Mn (97), T = Ni (98) and T = Cu (99). Taken from Ref. (100) (own publication). (Measurements and analysis by S. Selter and S. Wurmehl) 58

5.3.2. Magnetic susceptibility as a function of temperature and magnetization as a function of the external magnetic field within the substitution series for $BaCr_2As_2$ (a), $BaMn_2As_2$ (b), $BaFe_2As_2$ (c), $BaCo_2As_2$ (d), $BaNi_2As_2$ (e) and $BaCu_2As_2$ (f). An external magnetic field of $\mu_0 H = 1$ T was applied within the ab plane for all the compositions. Taken from Ref. (100) (own publication). 60

5.3.3. Zero field cooled (ZFC) and field cooled (FC) measurements for $BaNi_2As_2$ at 20 Oe probed down to ^{3}He temperatures (0.48-1 K). A clear superconducting transition can be seen at $T_C = 0.6$ K. Taken from Ref. (100) (own publication). 62

5.3.4. Optical reflectivity of $BaCu_2As_2$ at room temperature taken in the ab-plane of the crystal. The solid black line represents the measured data. The result of the Drude-Lorentz fit is shown as dashed red line (for details of the fit see text). In the inset the optical conductivity is shown, which results from the fit of the reflectivity data. The individual components are depicted as dashed lines: narrow (Drude 1, striped blue) and broad (Drude 2, striped grey) Drude peaks; Lorentz peaks (Lorentz 1, striped red and Lorentz 2, striped green). Taken from Ref. (100) (own publication). (Measurements and analysis by M. Knupfer *et al.*) 64

5.3.5. Zero-field specific heat as a function of temperature for $BaFe_2As_2$ (a) and $BaNi_2As_2$ (b) single crystals in the temperature range 2-160 K. Taken from Ref. (100) (own publication). 66

5.3.6. Low temperature $\frac{C_p}{T}(T^2)$ for all compounds of the BaT_2As$_2$ (T = Cr, Mn, Fe, Co, Ni, Cu) series at zero external magnetic field (full symbols) together with the linear fits used to extract γ_{exp}. It has to be noted that the linearity region found for Ni and Cu compounds is reduced with respect to the other compositions, probably due to the smaller extracted Debye temperatures, θ_D. (see table 5.3.2) Therefore, for these compositions, the higher order term (δT^5) was added to the lattice contribution, thus giving a good modeling of the data up to higher temperatures. The linear contributions for these two compositions are signaled by dashed lines for comparison. Taken from Ref. (100) (own publication). 68

5.3.7. Quasiparticle mass enhancement values extracted from specific heat measurements as function of the d-band filling n. The value for KFe$_2$As$_2$ from our previous work was added for comparison (79). The dashed line is a guide to the eye, which shows the general trend proposed in this work for $n > 5$. Taken from Ref. (100) (own publication). 69

5.3.8. Summary of the relevant parameters discussed in this work on the substitution series BaT_2As$_2$ (T = Cr, Mn, Fe, Ni, Co, Cu) as a function of the $3d$ band filling; for details see text and Figs. 5.3.1 and 5.3.7. Taken from Ref. (100) (own publication). 71

6.1.1. Schematic phase diagram of electron doped BaFe$_2$As$_2$, exemplifying the different phases for iron-pnictides and emphasizing the role played by nematic order and nematic fluctuations. SDW denotes the spin-density wave state, SC the superconducting phase, PM the paramagnetic phase, and Tet the tetragonal phase. Tetragonal symmetry is only broken below the nematic/orthorhombic transition line, but nematic fluctuations remain at higher temperatures, as discussed at the end of this section, and can be probed by shear modulus (130; 131) and resistivity anisotropy (132; 133) measurements. Taken from Ref. (127). 74

6.1.2. Schematic representation of the different order parameters involved in the nematic phase of iron-based superconductors: (a) Orthorhombic distortion (solid line) within the ab plane from the high temperature tetragonal (dashed line) symmetry. (b) In-plane anisotropy in the magnetic susceptibility $\chi_{i,j} = m_i/h_j$where m_i denotes the magnetization along the i direction induced by a magnetic field h_j applied along the j direction. (c) Splitting between the d_{xz} and the d_{yz} orbitals (orange and blue lines, respectively) shown in the lower panel, corresponding to a distortion of the Fermi surface pockets. Taken from Ref. (125). 75

6.1.3. Manifestations of orbital anisotropy in the nematic phase for $Ba(Fe_{1-x}Co_x)_2As_2$ by the application of uniaxial strain in the ab plane: (a) resisitivity anisotropy between the a and the b axes as a function of Co doping; (b) anisotropic band splitting between the d_{xz} and d_{yz} bands in twinned sample of $Ba(Fe_{0.975}Co_{0.025})_2As_2$ in the nematic phase obtained by ARPES measurements, while in the detwinned sample only one band is present for Γ-X/Y cuts of the Brillouin zone. Taken from Ref. (136) for (a) and Ref. (132) for (b). 76

6.1.4. (a) Scaling between normalized shear modulus ($C_{66}/C_{66,0}$) from three point bending and relaxation rate ($1/T_1T$) from NMR measurements, supporting the spin-nematic scenario for $Ba(Fe_{1-x}Co_x)_2As_2$. The inset shows the scaling parameters as a function of Co content. (b) Comparison between $1/T_1T$ as a function of temperature for Co doped Ba122 and FeSe. The black arrows signal the structural transitions T_S. Taken from Ref. (143). . 78

6.2.1. (a) Phase diagram of F-doped LaFeAsO polycrystals built from different probes. Taken from Ref. (151). (b) The electronic phase diagram of $LaFe_{1-x}Co_xAsO$. T_{anom} denotes the resistivity anomaly temperature for the SDW transition. T_{min} separates the metallic and semiconducting-like regions in the normal state of superconductors. Taken from Ref. (158). . . . 79

6.2.2.(a) NQR spectra of La1111 polycrystals, showing the development of a double peaked structure upon F substitution, coming from the different electronic environments, namely high-doping-like regions (HD) at higher frequency and low-doping-like regions (LD) at lower frequencies. The lower frequency peak corresponds to the parent compound, while at higher doping levels the single peak structure is recovered, corresponding to the optimally doped composition ($x = 0.11$). Taken from Ref. (159). (b) Phase diagram of REFeAsO$_{1-x}$F$_x$ (RE = La, Ce, Sm) as a function of $x_{\mathrm{NQR}}/x_{\mathrm{FSWT}}$, that approximate the actual electron doping level upon F substitution. The broad lines are guides for the eye. Taken from Ref. (159). 80

6.2.3.General phase diagram of Ba(Fe$_{1-x}T_x$)$_2$As$_2$: (a) $T - x$ phase diagrams for Co-, Ni-, Cu-, and Cu/Co-dopings of BaFe$_2$As$_2$. Here, x represents the number of substitutional transition metal ions per Fe site. (b) $T - p$ phase diagram of FeSe as a function of applied hydrostatic pressure (p). Taken from Refs. (169; 51) and (176), respectively. 82

6.3.1.(a) Crystal structure of LaFeAsO, evidencing the doping sites for in-plane Co doping and out-of-plane F doping (top-left). Images of single crystals (top-right) and crystal orientation (bottom) of the parent compound. The twinned and detwinned directions are evidenced in the picture in red and blue, respectively. Picture modified from Ref. (177). (b) Doping values determined by EDX vs nominal Co content. Taken from Ref. (178). 83

6.3.2.(left panel) Length change of the detwinned direction ($\Delta b/b_0$) for different applied uniaxial pressures for the 4.5% Co sample. The twinned curve is plotted for comparison. (right panel) Orthorhombic order parameter (δ) calculated as a function of pressure. 84

6.3.3.Normalized magnetization M/H for the LaFe$_{1-x}$Co$_x$AsO series: (a) parent compound, (b) 2.5%, (c) 3%, (d) 3.5%, (e) 4.5%, (f) 5%, (g) 6%, (h) 7.5% nominal Co content. A field of $\mu_0 H = 1$ T was applied within the ab plane (in some cases a field of 6 T was applied in order to improve the resolution). The insets for (a)-(e) show the temperature derivative of M/H, while for (f)-(h) the volume susceptibility is shown for $H = 10$ Oe at low temperature for both ZFC and FC measurement conditions (the higher noise level in 3% and 5% Co reflects the lower sample mass of these compositions). Taken from Ref. (185) (own publication). 86

6.3.4. Specific heat of $\mathrm{LaFe_{1-x}Co_xAsO}$ for (a) the parent compound and for 7.5% Co as well as (b) for 6% Co doping. The inset shows the determination of the superconducting transition temperature from the subtracted signal $\Delta C_{\mathrm{p}}/T = \frac{C_{\mathrm{p(0T)}}-C_{\mathrm{p(9T)}}}{T}$, approximating the specific heat contribution from the superconducting phase. Note that the offset in (a) for C_{p} for $T > 150$ K between the 0% and 7.5% Co is most probably due to the difference in the sample coupling at high temperature. Taken from Ref. (185) (own publication). 88

6.3.5. Thermal expansion of the $\mathrm{LaFe_{1-x}Co_xAsO}$ series: (a) normalized length changes $\Delta L/L_0$, (b) linear thermal expansion coefficient α_b, and (c) orthorhombic order parameter δ. The dashed lines represent the structural transition temperatures T_{S} for different Co contents, while the magnetic transition temperatures T_{N} are marked by arrows in (b). The inset of (c) shows a schematic representation of the twinned and detwinned measurement configurations. Note that the pressure applied to each crystal in the series varies due to the specific geometry and varying dimensions between sample. Taken from Ref. (185) (own publication). (2.5% and 3% Co curves measured by S. Sauerland) 90

6.3.6. Uniaxial pressure dependence of the thermal expansion coefficient in the detwinned direction (α_b) of $\mathrm{LaFe_{1-x}Co_xAsO}$ for (a) the parent compound and (b) 4.5% Co doping. It has to be noted that the application of increasing uniaxial pressure does not substantially increase the overall orthorhombic distortion, confirming the almost complete detwinning of the measured samples. Taken from Ref. (185) (own publication). 92

6.3.7. Anomalies in the linear thermal expansion coefficient for the a and b axes for 0, 2.5 and 3% Co content. The non-magnetic (i.e. electronic and phononic) contribution was approximated by using the thermal expansion coefficient obtained for the overdoped 7.5% Co, which does not show any transition in any of the thermodynamic quantities under study. Taken from Ref. (185) (own publication). 93

6.3.8. Phase diagram of Co-doped LaFeAsO single crystals. Points from NMR spectroscopy and resistivity on the same series of single crystals were added from Refs. (147) and (179), respectively. The shaded area within the orthorhombic/paramagnetic phase represents the doping region (4.5 - 6% Co) where direct lattice probes are not available. The phase boundaries for the nematic state in this region are extrapolated from the data points of neighboring compositions. The color coding in the superconducting dome reflects the rapid decrease of the superconducting volume fraction estimated from magnetization measurements around the optimally doped 6% Co content, as described in Section 6.3.3. Taken from Ref. (185) (own publication). . . 95

6.3.9. (a) General phase diagram of $\mathrm{LaFe}_{1-x}\mathrm{Co}_x\mathrm{AsO}$ single crystals derived from NMR measurements. Taken from Ref. (147). (b) Nematic susceptibility ($\tilde{n}$ in the graph) as a function of temperature and Co doping obtained from measurements of elastoresistance (ER). Taken from Ref. (179). The nematic temperature (T_{nem}) extracted from ER curves is reported in both graphs in pink and red stars respectively. Points from thermodynamic probes described in this work are reported for comparison. 96

6.3.10. NMR measurements on Co-doped single crystals for two exemplary compositions. Relaxation rate ($1/T_1T$) for $x = 0.03$ (a) and $x = 0.056$ samples. Different colors are used to mark different phases in the plots: in the left panel, the orange area denotes the nematic/paramagnetic and the light blue one signals the temperature region where both long-range magnetism and nematicity are present; in the right panel the shaded area marks the region where only short-range correlations are possibly present. Taken from Ref. (147). 97

List of Tables

5.3.1. Summary of the fit parameters of the Drude-Lorentz fit to the reflectivity of $BaCu_2As_2$. Two Drude-components and two Lorentz-components as well as a dielectric background ϵ_{inf} are included into the fit model. The two Drude terms model the conduction electrons while the two Lorentz terms and the background dielectric constant, ϵ_{inf}, represent the contribution of inter-band transitions in the measured energy range. Each component is represented by its oscillator strength ω_p, its energy position ω_0 ($\omega_0 = 0$ for the Drude terms), and its spectral width Γ. See Ref. (117) for details. Taken from Ref. (100) (own publication). (Measurements and analysis by M. Knupfer and M. Naumann) 64

5.3.2. Table 5.3.2 summarizes the experimental and theoretical Sommerfeld coefficients (γ_{exp} and γ_{th}, respectively) for each composition ($3d^4$ to $3d^{10}$), the Debye temperature (θ_D), the ground state (GS) and the experimental values for transition temperatures from magnetization and specific heat measurements. The magnetic ground state is indicated either as antiferromagnetic (AFM), paramagnetic (PM), superconducting (SC) or diamagnetic (DM). Taken from Ref. (100) (own publication). 67

Bibliography

[1] H. K. Onnes, in *KNAW, Proceedings*, Vol. 13 (1911) pp. 1910–1911.

[2] https://www.iter.org/ .

[3] https://www.zurich.ibm.com/st/quantum/index.html .

[4] B. Keimer, S. A. Kivelson, M. R. Norman, S. Uchida, and J. Zaanen, Nature **518**, 179 (2015).

[5] E. Snider, N. Dasenbrock-Gammon, R. McBride, M. Debessai, H. Vindana, K. Vencatasamy, K. V. Lawler, A. Salamat, and R. P. Dias, Nature **586**, 373 (2020).

[6] P. Fazekas, *Lecture Notes on Electron Correlation and Magnetism* (Series in Modern Condensed Matter Physics: Volume 5, 1999).

[7] S. Blundell, *Magnetism in condensed matter* (Oxford University Press, 2001).

[8] N. Ashcroft and N. D. Mermin, *Solid state physics* (Brooks/Cole CENGAGE learning, 1976).

[9] A. Tari, *The Specific Heat of Matter at Low Temperatures* (Imperial college press).

[10] J. F. Annett, *Superconductivity, superfluids and condensates* (Oxford University Press, 2004).

[11] R. Piazza, *Note di fisica statistica* (Springer, 2011).

[12] T. H. K. Barron and G. K. White, *Heat Capacity and Thermal Expansion at Low Temperatures* (Springer, 1999).

[13] L. D. Landau and E. M. Lifshitz, *Course of theoretical physics: Volume 5 - Statistical physics (part I and II)* (Editori Riuniti Univ. Press, 1981).

[14] P. Debye, Ann. Phys. , 789 (1912).

[15] C. Timm, Lecture notes on theoretical superconductivity (2018).

[16] J. Bardeen, L. N. Cooper, and J. R. Schrieffer, Physical Review **108**, 1175 (1957).

[17] D. N. Basov and A. V. Chubukov, Nature Physics **7**, 272 (2011).

[18] A. Chubukov, Annual Review of Condensed Matter Physics **3**, 57 (2012).

[19] Quantum Design San Diego. Magnetic Properties Measurement System: MPMS3 Users Manual. ().

[20] R. L. Fagaly, Review of Scientific Instruments **77**, 101101 (2006).

[21] B. D. Josephson, Physics Letters **1**, 251 (1962).

[22] M. Abdel-Hafiez, *Physical Properties of Iron-based Superconductors Probed by Low-Temperature Specific-Heat Measurements*, Ph.D. thesis, TU Dresden (2012).

[23] Quantum Design San Diego. PPMS: Heat Capacity Option Users Manual. ().

[24] L. Wang, *Thermal Expansion and Magnetostriction Studies on Iron Pnictides*, Ph.D. thesis, TU Dresden (2010).

[25] A. E. Böhmer, *Competing Phases in Iron-Based Superconductors Studied by High-Resolution Thermal-Expansion and Shear-Modulus Measurements*, Ph.D. thesis, Karlsruher Institut für Technologie (KIT) (2014).

[26] S. Sauerland, *Dilatometrische Studien zur elektronischen Nematizität und magnetoelastischen Kopplung in eisenbasierten Supraleitern und Magnetoelektrika*, Ph.D. thesis, Heidelberg Universität (2020).

[27] A. E. Böhmer and C. Meingast, Comptes Rendus Physique **17**, 90 (2016).

[28] R. Küchler, T. Bauer, M. Brando, and F. Steglich, Review of Scientific Instruments **83**, 095102 (2012).

[29] R. Pott and R. Schefzyk, Journal of Physics E: Scientific Instruments **16**, 444 (1983).

[30] F. R. Kroeger and C. A. Swenson, Journal of Applied Physics **48**, 853 (1977).

[31] R. H. Carr, R. D. McCammon, and G. K. White, Proceedings of the Royal Society of London. Series A. Mathematical and Physical Sciences **280**, 72 (1964).

[32] G. K. White, Cryogenics **1**, 151 (1961).

[33] B. Kundys, Y. Bukhantsev, S. Vasiliev, D. Kundys, M. Berkowski, and V. P. Dyakonov, Review of Scientific Instruments **75**, 2192 (2004).

[34] AH 2500A Capacitance Bridge User Manual .

[35] R. Küchler, C. Stingl, and P. Gegenwart, Review of Scientific Instruments **87**, 073903 (2016).

[36] M. Ikhlas, K. R. Shirer, P.-Y. Yang, A. P. Mackenzie, S. Nakatsuji, and C. W. Hicks, Applied Physics Letters **117**, 233502 (2020).

[37] https://phys.org/news/2016-08-unraveling-crystal-high-temperature-superconductor.html .

[38] Y. Kamihara, T. Watanabe, M. Hirano, and H. Hosono, Journal of the American Chemical Society **130**, 3296 (2008).

[39] G. Wu, Y. L. Xie, H. Chen, M. Zhong, R. H. Liu, B. C. Shi, Q. J. Li, X. F. Wang, T. Wu, Y. J. Yan, J. J. Ying, and X. H. Chen, Journal of Physics: Condensed Matter **21**, 142203 (2009).

[40] Q.-Y. Wang, Z. Li, W.-H. Zhang, Z.-C. Zhang, J.-S. Zhang, W. Li, H. Ding, Y.-B. Ou, P. Deng, K. Chang, J. Wen, C.-L. Song, K. He, J.-F. Jia, S.-H. Ji, Y.-Y. Wang, L.-L. Wang, X. Chen, X.-C. Ma, and Q.-K. Xue, Chinese Physics Letters **29**, 037402 (2012).

[41] J.-F. Ge, Z.-L. Liu, C. Liu, C.-L. Gao, D. Qian, Q.-K. Xue, Y. Liu, and J.-F. Jia, Nature Materials **14**, 285 (2014).

[42] D. Huang and J. E. Hoffman, Annual Review of Condensed Matter Physics **8**, 311 (2017).

[43] H. Hosono, A. Yamamoto, H. Hiramatsu, and Y. Ma, Materials Today **21**, 278 (2018).

[44] D.-H. Lee, Annual Review of Condensed Matter Physics **9**, 261 (2018).

[45] Q. Si, R. Yu, and E. Abrahams, Nature Reviews Materials **1**, 16017 (2016).

[46] D. C. Johnston, Advances in Physics **59**, 803 (2010).

[47] G. R. Stewart, Reviews of Modern Physics **83**, 1589 (2011).

[48] J. Paglione and R. L. Greene, Nature Physics **6**, 645 (2010).

[49] M. Yi, Y. Zhang, Z.-X. Shen, and D. Lu, npj Quantum Materials **2**, 57 (2017).

[50] F.-C. Hsu, J.-Y. Luo, K.-W. Yeh, T.-K. Chen, T.-W. Huang, P. M. Wu, Y.-C. Lee, Y.-L. Huang, Y.-Y. Chu, D.-C. Yan, and M.-K. Wu, Proceedings of the National Academy of Sciences **105**, 14262 (2008).

[51] P. C. Canfield and S. L. Bud'ko, Annual Review of Condensed Matter Physics **1**, 27 (2010).

[52] J. H. Tapp, Z. Tang, B. Lv, K. Sasmal, B. Lorenz, P. C. W. Chu, and A. M. Guloy, Physical Review B **78**, 060505(R) (2008).

[53] S. V. Borisenko, V. B. Zabolotnyy, D. V. Evtushinsky, T. K. Kim, I. V. Morozov, A. N. Yaresko, A. A. Kordyuk, G. Behr, A. Vasiliev, R. Follath, and B. Büchner, Physical Review Letters **105**, 067002 (2010).

[54] I. I. Mazin and V. P. Antropov, Physica C: Superconductivity **385**, 49 (2003).

[55] C. Liu, Y. Lee, A. D. Palczewski, J.-Q. Yan, T. Kondo, B. N. Harmon, R. W. McCallum, T. A. Lograsso, and A. Kaminski, Physical Review B **82**, 075135 (2010).

[56] Z. P. Yin, K. Haule, and G. Kotliar, Nature Materials **10**, 932 (2011).

[57] A. Martinelli, P. Manfrinetti, A. Provino, A. Genovese, F. Caglieris, G. Lamura, C. Ritter, and M. Putti, Physical Review Letters **118**, 055701 (2017).

[58] S. Lee, G. de la Peña, S. X.-L. Sun, M. Mitrano, Y. Fang, H. Jang, J.-S. Lee, C. Eckberg, D. Campbell, J. Collini, J. Paglione, F. M. F. de Groot, and P. Abbamonte, Physical Review Letters **122**, 147601 (2019).

[59] J. M. Guevara, *Spectroscopic imaging of novel correlated electronic phases*, Ph.D. thesis, TU Dresden (2020).

[60] A. E. Böhmer and A. Kreisel, Journal of Physics: Condensed Matter **30**, 023001 (2017).

[61] H. Luetkens, H.-H. Klauss, M. Kraken, F. J. Litterst, T. Dellmann, R. Klingeler, C. Hess, R. Khasanov, A. Amato, C. Baines, M. Kosmala, O. J. Schumann, M. Braden, J. Hamann-Borrero, N. Leps, A. Kondrat, G. Behr, J. Werner, and B. Büchner, Nature Materials **8**, 305 (2009).

[62] M. Imada, A. Fujimori, and Y. Tokura, Reviews of Modern Physics **70**, 1039 (1998).

[63] L. de' Medici, J. Mravlje, and A. Georges, Physical Review Letters **107**, 256401 (2011).

[64] A. Georges, L. de' Medici, and J. Mravlje, Annual Review of Condensed Matter Physics **4**, 137 (2013).

[65] S. Backes, H. O. Jeschke, and R. Valentí, Physical Review B **92**, 195128 (2015).

[66] F. Hardy, A. E. Böhmer, D. Aoki, P. Burger, T. Wolf, P. Schweiss, R. Heid, P. Adelmann, Y. X. Yao, G. Kotliar, J. Schmalian, and C. Meingast, Physical Review Letters **111**, 027002 (2013).

[67] M. Rotter, M. Tegel, D. Johrendt, I. Schellenberg, W. Hermes, and R. Pöttgen, Physical Review B **78**, 020503(R) (2008).

[68] A. S. Sefat, D. J. Singh, R. Jin, M. A. McGuire, B. C. Sales, F. Ronning, and D. Mandrus, Physica C: Superconductivity **469**, 350 (2009).

[69] Y. Singh, M. A. Green, Q. Huang, A. Kreyssig, R. J. McQueeney, D. C. Johnston, and A. I. Goldman, Physical Review B **80**, 100403(R) (2009).

[70] S. F. Wu, P. Richard, A. van Roekeghem, S. M. Nie, H. Miao, N. Xu, T. Qian, B. Saparov, Z. Fang, S. Biermann, A. S. Sefat, and H. Ding, Physical Review B **91**, 235109 (2015).

[71] K. A. Filsinger, W. Schnelle, P. Adler, G. H. Fecher, M. Reehuis, A. Hoser, J.-U. Hoffmann, P. Werner, M. Greenblatt, and C. Felser, Physical Review B **95**, 184414 (2017).

[72] F. Hardy, P. Burger, T. Wolf, R. A. Fisher, P. Schweiss, P. Adelmann, R. Heid, R. Fromknecht, R. Eder, D. Ernst, H. v. Löhneysen, and C. Meingast, EPL (Europhysics Letters) **91**, 47008 (2010).

[73] F. Hardy, A. E. Böhmer, L. de' Medici, M. Capone, G. Giovannetti, R. Eder, L. Wang, M. He, T. Wolf, P. Schweiss, R. Heid, A. Herbig, P. Adelmann, R. A. Fisher, and C. Meingast, Physical Review B **94**, 205113 (2016).

[74] L. de' Medici, G. Giovannetti, and M. Capone, Physical Review Letters **112**, 177001 (2014).

[75] P. Popovich, A. V. Boris, O. V. Dolgov, A. A. Golubov, D. L. Sun, C. T. Lin, R. K. Kremer, and B. Keimer, Physical Review Letters **105**, 027003 (2010).

[76] G. Mu, H. Luo, Z. Wang, L. Shan, C. Ren, and H.-H. Wen, Physical Review B **79**, 174501 (2009).

[77] A. K. Pramanik, M. Abdel-Hafiez, S. Aswartham, A. U. B. Wolter, S. Wurmehl, V. Kataev, and B. Büchner, Physical Review B **84**, 064525 (2011).

[78] J. S. Kim, E. G. Kim, G. R. Stewart, X. H. Chen, and X. F. Wang, Physical Review B **83**, 172502 (2011).

[79] M. Abdel-Hafiez, S. Aswartham, S. Wurmehl, V. Grinenko, C. Hess, S.-L. Drechsler, S. Johnston, A. U. B. Wolter, B. Büchner, H. Rosner, and L. Boeri, Physical Review B **85**, 134533 (2012).

[80] L. Degiorgi, New Journal of Physics **13**, 023011 (2011).

[81] G. Li, W. Z. Hu, J. Dong, Z. Li, P. Zheng, G. F. Chen, J. L. Luo, and N. L. Wang, Physical Review Letters **101**, 107004 (2008).

[82] J. Yang, D. Hüvonen, U. Nagel, T. Rõõm, N. Ni, P. C. Canfield, S. L. Bud'ko, J. P. Carbotte, and T. Timusk, Physical Review Letters **102**, 187003 (2009).

[83] N. L. Wang, W. Z. Hu, Z. G. Chen, R. H. Yuan, G. Li, G. F. Chen, and T. Xiang, Journal of Physics: Condensed Matter **24**, 294202 (2012).

[84] B. Mansart, E. Papalazarou, M. F. Jensen, V. Brouet, L. Petaccia, L. de' Medici, G. Sangiovanni, F. Rullier-Albenque, A. Forget, D. Colson, and M. Marsi, Physical Review B **85**, 144508 (2012).

[85] M. Yi, D. H. Lu, J. G. Analytis, J.-H. Chu, S.-K. Mo, R.-H. He, R. G. Moore, X. J. Zhou, G. F. Chen, J. L. Luo, N. L. Wang, Z. Hussain, D. J. Singh, I. R. Fisher, and Z.-X. Shen, Physical Review B **80**, 024515 (2009).

[86] T. Yoshida, S. Ideta, I. Nishi, A. Fujimori, M. Yi, R. G. Moore, S. K. Mo, D. H. Lu, Z. X. Shen, Z. Hussain, K. Kihou, P. M. Shirage, H. Kito, C. H. Lee, A. Iyo, H. Eisaki, and H. Harima, arXiv:1205.6911 1205.6911v1 .

[87] H. Ding, K. Nakayama, P. Richard, S. Souma, T. Sato, T. Takahashi, M. Neupane, Y.-M. Xu, Z.-H. Pan, A. V. Fedorov, Z. Wang, X. Dai, Z. Fang, G. F. Chen, J. L. Luo, and N. L. Wang, Journal of Physics: Condensed Matter **23**, 135701 (2011).

[88] T. Terashima, M. Kimata, N. Kurita, H. Satsukawa, A. Harada, K. Hazama, M. Imai, A. Sato, K. Kihou, C.-H. Lee, H. Kito, H. Eisaki, A. Iyo, T. Saito, H. Fukazawa, Y. Kohori, H. Harima, and S. Uji, Journal of the Physical Society of Japan **79**, 053702 (2010).

[89] Y. Singh, A. Ellern, and D. C. Johnston, Physical Review B **79**, 094519 (2009).

[90] D. C. Johnston, R. J. McQueeney, B. Lake, A. Honecker, M. E. Zhitomirsky, R. Nath, Y. Furukawa, V. P. Antropov, and Y. Singh, Physical Review B **84**, 094445 (2011).

[91] M. A. McGuire and V. O. Garlea, Physical Review B **93**, 054404 (2016).

[92] T. Hanna, S. Matsuishi, K. Kodama, T. Otomo, S.-i. Shamoto, and H. Hosono, Physical Review B **87**, 020401 (2013).

[93] M. Nakajima, S. Ishida, T. Tanaka, K. Kihou, Y. Tomioka, T. Saito, C.-H. Lee, H. Fukazawa, Y. Kohori, T. Kakeshita, A. Iyo, T. Ito, H. Eisaki, and S. ichi Uchida, Journal of the Physical Society of Japan **83**, 104703 (2014).

[94] B. Cordero, V. Gómez, A. E. Platero-Prats, M. Revés, J. Echeverría, E. Cremades, F. Barragán, and S. Alvarez, Dalton Transactions **21**, 2832 (2008).

[95] F. Rullier-Albenque, D. Colson, A. Forget, P. Thuéry, and S. Poissonnet, Physical Review B **81**, 224503 (2010).

[96] M. Pfisterer and G. Nagorsen, Zeitschrift für Naturforschung B **35**, 703 (1980).

[97] E. Brechtel, G. Cordier, and H. Schäfer, Zeitschrift für Naturforschung B **33**, 820 (1978).

[98] F. Ronning, N. Kurita, E. D. Bauer, B. L. Scott, T. Park, T. Klimczuk, R. Movshovich, and J. D. Thompson, Journal of Physics: Condensed Matter **20**, 342203 (2008).

[99] B. Saparov and A. S. Sefat, Journal of Solid State Chemistry **191**, 213 (2012).

[100] S. Selter, F. Scaravaggi, R. Kappenberger, M. Naumann, V. V. Romaka, M. Knupfer, S. Aswartham, A. U. B. Wolter, S. Wurmehl, and B. Büchner, Inorganic Chemistry **59**, 16913 (2020).

[101] K. Kitagawa, N. Katayama, K. Ohgushi, M. Yoshida, and M. Takigawa, Journal of the Physical Society of Japan **77**, 114709 (2008).

[102] S. Kitao, Y. Kobayashi, S. Higashitaniguchi, M. Saito, Y. Kamihara, M. Hirano, T. Mitsui, H. Hosono, and M. Seto, Journal of the Physical Society of Japan **77**, 103706 (2008).

[103] T. Shimojima, K. Ishizaka, Y. Ishida, N. Katayama, K. Ohgushi, T. Kiss, M. Okawa, T. Togashi, X.-Y. Wang, C.-T. Chen, S. Watanabe, R. Kadota, T. Oguchi, A. Chainani, and S. Shin, Physical Review Letters **104**, 057002 (2010).

[104] A. Khasanov, S. C. Bhargava, J. G. Stevens, J. Jiang, J. D. Weiss, E. E. Hellstrom, and A. Nath, Journal of Physics: Condensed Matter **23**, 202201 (2011).

[105] J. A. McLeod, A. Buling, R. J. Green, T. D. Boyko, N. A. Skorikov, E. Z. Kurmaev, M. Neumann, L. D. Finkelstein, N. Ni, A. Thaler, S. L. Bud'ko, P. C. Canfield, and A. Moewes, Journal of Physics: Condensed Matter **24**, 215501 (2012).

[106] K. Honda, Annalen der Physik **337**, 1027 (1910).

[107] M. Owen, Annalen der Physik **342**, 657 (1912).

[108] S. Aswartham, C. Nacke, G. Friemel, N. Leps, S. Wurmehl, N. Wizent, C. Hess, R. Klingeler, G. Behr, S. Singh, and B. Büchner, Journal of Crystal Growth **314**, 341 (2011).

[109] X. F. Wang, T. Wu, G. Wu, H. Chen, Y. L. Xie, J. J. Ying, Y. J. Yan, R. H. Liu, and X. H. Chen, Physical Review Letters **102**, 117005 (2009).

[110] S. Aswartham, M. Abdel-Hafiez, D. Bombor, M. Kumar, A. U. B. Wolter, C. Hess, D. V. Evtushinsky, V. B. Zabolotnyy, A. A. Kordyuk, T. K. Kim, S. V. Borisenko, G. Behr, B. Büchner, and S. Wurmehl, Physical Review B **85**, 224520 (2012).

[111] A. S. Sefat, D. J. Singh, R. Jin, M. A. McGuire, B. C. Sales, and D. Mandrus, Physical Review B **79**, 024512 (2009).

[112] K. Ahilan, T. Imai, A. S. Sefat, and F. Ning, Physical Review B **90**, 014520 (2014).

[113] V. Anand, D. G. Quirinale, Y. Lee, B. N. Harmon, Y. Furukawa, V. Ogloblichev, A. Huq, D. Abernathy, P. Stephens, R. J. McQueeney, *et al.*, Physical Review B **90**, 064517 (2014).

[114] A. S. Sefat, M. A. McGuire, R. Jin, B. C. Sales, D. Mandrus, F. Ronning, E. D. Bauer, and Y. Mozharivskyj, Physical Review B **79**, 094508 (2009).

[115] I. R. Shein and A. L. Ivanovskii, Physical Review B **79**, 054510 (2009).

[116] D. J. Singh, Physical Review B **79**, 153102 (2009).

[117] C. Habenicht, A. Lubk, R. Schuster, M. Knupfer, and B. Büchner, Physical Review B **101**, 155429 (2020).

[118] Z. G. Chen, G. Xu, W. Z. Hu, X. D. Zhang, P. Zheng, G. F. Chen, J. L. Luo, Z. Fang, and N. L. Wang, Physical Review B **80**, 094506 (2009).

[119] N. Ni, S. L. Bud'ko, A. Kreyssig, S. Nandi, G. E. Rustan, A. I. Goldman, S. Gupta, J. D. Corbett, A. Kracher, and P. C. Canfield, Physical Review B **78**, 014507 (2008).

[120] D. J. Singh, A. S. Sefat, M. A. McGuire, B. C. Sales, D. Mandrus, L. H. VanBebber, and V. Keppens, Physical Review B **79**, 094429 (2009).

[121] W.-L. Zhang, P. Richard, A. van Roekeghem, S.-M. Nie, N. Xu, P. Zhang, H. Miao, S.-F. Wu, J.-X. Yin, B. B. Fu, L.-Y. Kong, T. Qian, Z.-J. Wang, Z. Fang, A. S. Sefat, S. Biermann, and H. Ding, Physical Review B **94**, 155155 (2016).

[122] K. Matan, R. Morinaga, K. Iida, and T. J. Sato, Physical Review B **79**, 054526 (2009).

[123] J. Hubbard, Proceedings of the Royal Society of London. Series A. Mathematical and Physical Sciences **276**, 238 (1963).

[124] E. Fradkin, S. A. Kivelson, M. J. Lawler, J. P. Eisenstein, and A. P. Mackenzie, Annual Review of Condensed Matter Physics **1**, 153 (2010).

[125] R. M. Fernandes, A. V. Chubukov, and J. Schmalian, Nature Physics **10**, 97 (2014).

[126] R. M. Fernandes, A. V. Chubukov, J. Knolle, I. Eremin, and J. Schmalian, Physical Review B **85**, 024534 (2012).

[127] R. M. Fernandes and J. Schmalian, Superconductor Science and Technology **25**, 084005 (2012).

[128] A. V. Chubukov, R. M. Fernandes, and J. Schmalian, Physical Review B **91**, 201105(R) (2015).

[129] J. Kang, R. M. Fernandes, and A. Chubukov, Physical Review Letters **120**, 267001 (2018).

[130] R. M. Fernandes, L. H. VanBebber, S. Bhattacharya, P. Chandra, V. Keppens, D. Mandrus, M. A. McGuire, B. C. Sales, A. S. Sefat, and J. Schmalian, Physical Review Letters **105**, 157003 (2010).

[131] M. Yoshizawa, D. Kimura, T. Chiba, S. Simayi, Y. Nakanishi, K. Kihou, C.-H. Lee, A. Iyo, H. Eisaki, M. Nakajima, and S. ichi Uchida, Journal of the Physical Society of Japan **81**, 024604 (2012).

[132] J.-H. Chu, J. G. Analytis, K. D. Greve, P. L. McMahon, Z. Islam, Y. Yamamoto, and I. R. Fisher, Science **329**, 824 (2010).

[133] M. A. Tanatar, E. C. Blomberg, A. Kreyssig, M. G. Kim, N. Ni, A. Thaler, S. L. Bud'ko, P. C. Canfield, A. I. Goldman, I. I. Mazin, and R. Prozorov, Physical Review B **81**, 184508 (2010).

[134] M. G. Kim, R. M. Fernandes, A. Kreyssig, J. W. Kim, A. Thaler, S. L. Bud'ko, P. C. Canfield, R. J. McQueeney, J. Schmalian, and A. I. Goldman, Physical Review B **83**, 134522 (2011).

[135] S. Kasahara, H. J. Shi, K. Hashimoto, S. Tonegawa, Y. Mizukami, T. Shibauchi, K. Sugimoto, T. Fukuda, T. Terashima, A. H. Nevidomskyy, and Y. Matsuda, Nature **486**, 382 (2012).

[136] M. Yi, D. Lu, J.-H. Chu, J. G. Analytis, A. P. Sorini, A. F. Kemper, B. Moritz, S.-K. Mo, R. G. Moore, M. Hashimoto, W.-S. Lee, Z. Hussain, T. P. Devereaux, I. R. Fisher, and Z.-X. Shen, Proceedings of the National Academy of Sciences **108**, 6878 (2011).

[137] J.-H. Chu, H.-H. Kuo, J. G. Analytis, and I. R. Fisher, Science **337**, 710 (2012).

[138] L. Boeri, O. V. Dolgov, and A. A. Golubov, Physical Review Letters **101**, 026403 (2008).

[139] H. Kontani and S. Onari, Physical Review Letters **104**, 157001 (2010).

[140] P. J. Hirschfeld, M. M. Korshunov, and I. I. Mazin, Reports on Progress in Physics **74**, 124508 (2011).

[141] R. M. Fernandes and A. J. Millis, Physical Review Letters **111**, 127001 (2013).

[142] A. V. Chubukov, M. Khodas, and R. M. Fernandes, Physical Review X **6**, 041045 (2016).

[143] A. E. Böhmer, P. Burger, F. Hardy, T. Wolf, P. Schweiss, R. Fromknecht, M. Reinecker, W. Schranz, and C. Meingast, Physical Review Letters **112**, 047001 (2014).

[144] S.-H. Baek, D. V. Efremov, J. M. Ok, J. S. Kim, J. van den Brink, and B. Büchner, Nature Materials **14**, 210 (2014).

[145] A. E. Böhmer, T. Arai, F. Hardy, T. Hattori, T. Iye, T. Wolf, H. v. Löhneysen, K. Ishida, and C. Meingast, Physical Review Letters **114**, 027001 (2015).

[146] M. He, L. Wang, F. Hardy, L. Xu, T. Wolf, P. Adelmann, and C. Meingast, Physical Review B **97**, 104107 (2018).

[147] P. Lepucki, R. Havemann, A. P. Dioguardi, F. Scaravaggi, A. U. B. Wolter, R. Kappenberger, S. Aswartham, S. Wurmehl, B. Büchner, and H.-J. Grafe, Physical Review B **103**, L180506 (2021).

[148] M. A. Tanatar, A. Kreyssig, S. Nandi, N. Ni, S. L. Bud'ko, P. C. Canfield, A. I. Goldman, and R. Prozorov, Physical Review B **79**, 180508(R) (2009).

[149] I. R. Fisher, L. Degiorgi, and Z. X. Shen, Reports on Progress in Physics **74**, 124506 (2011).

[150] T. Nomura, S. W. Kim, Y. Kamihara, M. Hirano, P. V. Sushko, K. Kato, M. Takata, A. L. Shluger, and H. Hosono, Superconductor Science and Technology **21**, 125028 (2008).

[151] C. Hess, H. Grafe, A. Kondrat, G. Lang, F. Hammerath, L. Wang, R. Klingeler, G. Behr, and B. Büchner, Physica Status Solidi B **254**, 1600214 (2016).

[152] H. Maeter, J. E. H. Borrero, T. Goltz, J. Spehling, A. Kwadrin, A. Kondrat, L. Veyrat, G. Lang, H.-J. Grafe, C. Hess, G. Behr, B. Büchner, H. Luetkens, C. Baines, A. Amato, N. Leps, R. Klingeler, R. Feyerherm, D. Argyriou, and H.-H. Klauss, (2012), arXiv:1210.6959v1 .

[153] N. Qureshi, Y. Drees, J. Werner, S. Wurmehl, C. Hess, R. Klingeler, B. Büchner, M. T. Fernandez-Diaz, and M. Braden, Physical Review B **82**, 184521 (2010).

[154] Z.-A. Ren, G.-C. Che, X.-L. Dong, J. Yang, W. Lu, W. Yi, X.-L. Shen, Z.-C. Li, L.-L. Sun, F. Zhou, and Z.-X. Zhao, EPL (Europhysics Letters) **83**, 17002 (2008).

[155] X. H. Chen, T. Wu, G. Wu, R. H. Liu, H. Chen, and D. F. Fang, Nature **453**, 761 (2008).

[156] G. F. Chen, Z. Li, D. Wu, G. Li, W. Z. Hu, J. Dong, P. Zheng, J. L. Luo, and N. L. Wang, Physical Review Letters **100**, 247002 (2008).

[157] Z.-A. Ren, J. Yang, W. Lu, W. Yi, X.-L. Shen, Z.-C. Li, G.-C. Che, X.-L. Dong, L.-L. Sun, F. Zhou, and Z.-X. Zhao, EPL (Europhysics Letters) **82**, 57002 (2008).

[158] C. Wang, Y. K. Li, Z. W. Zhu, S. Jiang, X. Lin, Y. K. Luo, S. Chi, L. J. Li, Z. Ren, M. He, H. Chen, Y. T. Wang, Q. Tao, G. H. Cao, and Z. A. Xu, Physical Review B **79**, 054521 (2009).

[159] G. Lang, L. Veyrat, U. Gräfe, F. Hammerath, D. Paar, G. Behr, S. Wurmehl, and H.-J. Grafe, Physical Review B **94**, 014514 (2016).

[160] H.-J. Grafe, P. Lepucki, M. Witschel, A. P. Dioguardi, R. Kappenberger, S. Aswartham, S. Wurmehl, and B. Büchner, Physical Review B **101**, 054519 (2020).

[161] R. Klingeler, N. Leps, I. Hellmann, A. Popa, U. Stockert, C. Hess, V. Kataev, H.-J. Grafe, F. Hammerath, G. Lang, S. Wurmehl, G. Behr, L. Harnagea, S. Singh, and B. Büchner, Physical Review B **81**, 024506 (2010).

[162] R. Klingeler, L. Wang, U. Köhler, G. Behr, C. Hess, and B. Büchner, Journal of Physics: Conference Series **200**, 012088 (2010).

[163] H.-H. Klauss, H. Luetkens, R. Klingeler, C. Hess, F. J. Litterst, M. Kraken, M. M. Korshunov, I. Eremin, S.-L. Drechsler, R. Khasanov, A. Amato, J. Hamann-Borrero, N. Leps, A. Kondrat, G. Behr, J. Werner, and B. Büchner, Physical Review Letters **101**, 077005 (2008).

[164] M. A. McGuire, R. P. Hermann, A. S. Sefat, B. C. Sales, R. Jin, D. Mandrus, F. Grandjean, and G. J. Long, New Journal of Physics **11**, 025011 (2009).

[165] T. Shiroka, G. Lamura, S. Sanna, G. Prando, R. D. Renzi, M. Tropeano, M. R. Cimberle, A. Martinelli, C. Bernini, A. Palenzona, R. Fittipaldi, A. Vecchione, P. Carretta, A. S. Siri, C. Ferdeghini, and M. Putti, Physical Review B **84**, 195123 (2011).

[166] A. S. Sefat, A. Huq, M. A. McGuire, R. Jin, B. C. Sales, D. Mandrus, L. M. D. Cranswick, P. W. Stephens, and K. H. Stone, Physical Review B **78**, 104505 (2008).

[167] G. Lang, H.-J. Grafe, D. Paar, F. Hammerath, K. Manthey, G. Behr, J. Werner, and B. Büchner, Physical Review Letters **104**, 097001 (2010).

[168] P. Lepucki, R. Kappenberger, S. Aswartham, S. Wurmehl, A. P. Dioguardi, B. Büchner, and H.-J. Grafe, NQR measurements on Co-doped REFeAsO powders (unpublished) (2020).

[169] P. C. Canfield, S. L. Bud'ko, N. Ni, J. Q. Yan, and A. Kracher, Physical Review B **80**, 060501(R) (2009).

[170] N. Ni, A. Thaler, A. Kracher, J. Q. Yan, S. L. Bud'ko, and P. C. Canfield, Physical Review B **80**, 024511 (2009).

[171] L. Wang, F. Hardy, A. E. Böhmer, T. Wolf, P. Schweiss, and C. Meingast, Physical Review B **93**, 014514 (2016).

[172] A. E. Böhmer, P. Burger, F. Hardy, T. Wolf, P. Schweiss, R. Fromknecht, H. v. Löhneysen, C. Meingast, H. K. Mak, R. Lortz, S. Kasahara, T. Terashima, T. Shibauchi, and Y. Matsuda, Physical Review B **86**, 094521 (2012).

[173] L. Wang, M. He, D. D. Scherer, F. Hardy, P. Schweiss, T. Wolf, M. Merz, B. M. Andersen, and C. Meingast, Journal of the Physical Society of Japan **88**, 104710 (2019).

[174] A. E. Böhmer, F. Hardy, L. Wang, T. Wolf, P. Schweiss, and C. Meingast, Nature Communications **6**, 7911 (2015).

[175] K. Kothapalli, A. E. Böhmer, W. T. Jayasekara, B. G. Ueland, P. Das, A. Sapkota, V. Taufour, Y. Xiao, E. Alp, S. L. Bud'ko, P. C. Canfield, A. Kreyssig, and A. I. Goldman, Nature Communications **7**, 12728 (2016).

[176] K. Matsuura, Y. Mizukami, Y. Arai, Y. Sugimura, N. Maejima, A. Machida, T. Watanuki, T. Fukuda, T. Yajima, Z. Hiroi, K. Y. Yip, Y. C. Chan, Q. Niu, S. Hosoi, K. Ishida, K. Mukasa, S. Kasahara, J.-G. Cheng, S. K. Goh, Y. Matsuda, Y. Uwatoko, and T. Shibauchi, Nature Communications **8**, 1143 (2017).

[177] R. Kappenberger, S. Aswartham, F. Scaravaggi, C. G. F. Blum, M. I. Sturza, A. U. B. Wolter, S. Wurmehl, and B. Büchner, Journal of Crystal Growth **483**, 9 (2018).

[178] R. Kappenberger, *Das System LaFeAsO in Poly- und Einkristallen*, Ph.D. thesis, TU Dresden (2017).

[179] X. Hong, F. Caglieris, R. Kappenberger, S. Wurmehl, S. Aswartham, F. Scaravaggi, P. Lepucki, A. U. B. Wolter, H.-J. Grafe, B. Büchner, and C. Hess, Physical Review Letters **125**, 067001 (2020).

[180] C. Wuttke, F. Caglieris, F. Steckel, X. Hong, S. Sykora, S. Ran, S. Khim, Kappenberger, C. Blum, S. L. Bud'ko, P. C. Canfield, S. Wurmehl, S. Aswartham, B. Büchner, and C. Hess, Nematic fluctuations probed by Nernst effect (unpublished) (2020).

[181] F. Caglieris, C. Wuttke, X. C. Hong, S. Sykora, R. Kappenberger, S. Aswartham, S. Wurmehl, B. Büchner, and C. Hess, npj Quantum Materials **6**, 27 (2021).

[182] A. Jesche, F. Nitsche, S. Probst, T. Doert, P. Müller, and M. Ruck, Physical Review B **86**, 134511 (2012).

[183] G. Li, G. Grissonnanche, J.-Q. Yan, R. W. McCallum, T. A. Lograsso, H. D. Zhou, and L. Balicas, Physical Review B **86**, 054517 (2012).

[184] T. Shang, L. Yang, Y. Chen, N. Cornell, F. Ronning, J. L. Zhang, L. Jiao, Y. H. Chen, J. Chen, A. Howard, J. Dai, J. D. Thompson, A. Zakhidov, M. B. Salamon, and H. Q. Yuan, Physical Review B **87**, 075148 (2013).

[185] F. Scaravaggi, S. Sauerland, L. Wang, R. Kappenberger, P. Lepucki, A. P. Dioguardi, X. Hong, F. Caglieris, C. Wuttke, C. Hess, H.-J. Grafe, S. Aswartham, S. Wurmehl, R. Klingeler, A. U. B. Wolter, and B. Büchner, Physical Review B **103**, 174506 (2021).

[186] G. Prando, O. Vakaliuk, S. Sanna, G. Lamura, T. Shiroka, P. Bonfà, P. Carretta, R. D. Renzi, H.-H. Klauss, C. G. F. Blum, S. Wurmehl, C. Hess, and B. Büchner, Physical Review B **87**, 174519 (2013).

[187] L. Wang, S. Sauerland, F. Scaravaggi, R. Kappenberger, S. Aswartham, S. Wurmehl, A. U. B. Wolter, B. Büchner, and R. Klingeler, Journal of Magnetism and Magnetic Materials **482**, 50 (2019).

[188] S. Avci, O. Chmaissem, E. A. Goremychkin, S. Rosenkranz, J.-P. Castellan, D. Y. Chung, I. S. Todorov, J. A. Schlueter, H. Claus, M. G. Kanatzidis, A. Daoud-Aladine, D. Khalyavin, and R. Osborn, Physical Review B **83**, 172503 (2011).

[189] L. Wang, U. Köhler, N. Leps, A. Kondrat, M. Nale, A. Gasparini, A. de Visser, G. Behr, C. Hess, R. Klingeler, and B. Büchner, Physical Review B **80**, 094512 (2009).

[190] C. Dhital, Z. Yamani, W. Tian, J. Zeretsky, A. S. Sefat, Z. Wang, R. J. Birgeneau, and S. D. Wilson, Physical Review Letters **108**, 087001 (2012).

[191] X. Lu, K.-F. Tseng, T. Keller, W. Zhang, D. Hu, Y. Song, H. Man, J. T. Park, H. Luo, S. Li, A. H. Nevidomskyy, and P. Dai, Physical Review B **93**, 134519 (2016).

[192] E. Wiesenmayer, H. Luetkens, G. Pascua, R. Khasanov, A. Amato, H. Potts, B. Banusch, H.-H. Klauss, and D. Johrendt, Physical Review Letters **107**, 237001 (2011).

[193] S. Nandi, M. G. Kim, A. Kreyssig, R. M. Fernandes, D. K. Pratt, A. Thaler, N. Ni, S. L. Bud'ko, P. C. Canfield, J. Schmalian, R. J. McQueeney, and A. I. Goldman, Physical Review Letters **104**, 057006 (2010).

Acknowledgements

First of all, I would like to acknowledge Prof. Bernd Büchner and Dr. Anja Wolter-Giraud for giving me the opportunity to work in IFW and pursue my doctoral studies under their supervision. IFW Dresden and the Leibniz association offered many opportunities to develop this experimental work in terms of equipment, expertise and connections, particularly in the field of Fe-based superconductors.

I particularly want to acknowledge Anja for closely following my PhD work through these years, being open for discussing data and measurements and also for always being positive and supportive during my PhD journey.

I would also like to thank all the members of the "Magnetic and Thermodynamic Properties" group, that always proved to be ready to help and support each other and didn't miss a chance to contribute to create and maintain a pleasant and positive atmosphere in as well as outside our work environment. A special thank goes to Laura, who very patiently took the time to introduce me to the PPMS and contributed to supervise the last part of my PhD journey. Particularly, I would also like to thank Sebastian Gaß for his availability always helpful technical support in the lab and for the many discussions on measurements, especially for dilatometry.

I would like to acknowledge the Research training group GRK1621 for funding my PhD, and also for providing many opportunities for discussing results and report progresses within the group. In particular, I want to thank Prof. Hans-Henning Klauß and Verena Klingenhöfer for their efforts and commitment to plan and organize periodic events (workshops and conferences), giving us the chance to present our data as well as to have interesting discussions with international experts in our fields of study.

I would like to thank S. Selter and R. Kappenberger, under the supervision of S. Wurmehl and S. Aswartham, for the nice single crystals that made this work possible in the first place and for always being open for many discussions.

I would like to acknowledge the group of Prof. R. Klingeler at the Heidelberg University for the fruitful collaboration on thermodynamic measurements during this years. In particular, I would like to thank S. Sauerland and L. Wang for introducing me to dilatometry in the first place and for the many exchanges and nice discussions that lead to our common publications and this thesis.

I would also like to thank my friends and colleagues from IFW, with which I shared countless nice and funny moments, discussions, hiking trips and (succeeded or at least

attempted) sport activities during my (long) time in Dresden: Jose, Ziba, Cliò, Alex, Margarita, Richard, Adam, Matthias, Christoph, Piotr, Sebastian, Julian, Federico, Gaël, Scarlett, Basti and Toma. Thank you all for being awesome people! A special mention of honor goes to Tom and Aniruddha, with which we shared the little solar sauna that was our office in this last period.

I also want to thank all my friends at home, with which we still managed to keep in touch and gather whenever is possible, despite living far away from each other.

Infine, vorrei ringraziare particolarmente i miei genitori, che, nonostante le non poche difficoltà di questi anni, non mi hanno mai fatto mancare il loro affetto e il loro sostegno in questo importante percorso.

Erklärung

Hiermit versichere ich, dass ich die vorliegende Arbeit ohne unzulässige Hilfe Dritter und ohne Benutzung anderer als der angegebenen Hilfsmittel angefertigt habe. Die aus fremden Quellen direkt oder indirekt übernommenen Gedanken sind als solche kenntlich gemacht. Die Arbeit wurde bisher weder im Inland noch im Ausland in gleicher oder ähnlicher Form einer anderen Prüfungsbehörde vorgelegt.

Diese Arbeit wurde unter Betreuung von Prof. Büchner am Institut für Festkörperforschung (IFF) des Institutes für Festkörper- und Werkstoffforschung Dresden e.V. (IFW Dresden) angefertigt. Es haben keine früheren erfolglosen Promotionsverfahren stattgefunden.

Ich erkenne hiermit die Promotionsordnung der Fakultät Mathematik und Naturwissenschaften der Technischen Universität Dresden vom 23.02.2011 an.

Francesco Scaravaggi
Dresden, Juli 2021

List of publications

1. M. Valldor, R. Yadav, L. Hozoi, J. van den Brink, A. Maljuk, J. Werner, **F. Scaravaggi**, A. U. B. Wolter and B. Büchner, *"Swedenborgite $CaBa(Mn_2Fe_2)O_7$ with spin ordering on a geometrically frustrated, polar, non-centrosymmetric $S = 5/2$ lattice"*, *Z. Anorg. Allg. Chem.* **643**, 1543-1550 (2017).

2. R. Kappenberger, S. Aswartham, **F. Scaravaggi**, C. G. Blum, M. I. Sturza, A. U. B. Wolter and B. Büchner, *"Solid state single crystal growth of three-dimensional faceted LaFeAsO crystals"*, *Journal of Crystal Growth* **483**, 9-15 (2018).

3. M. Vogl, L. T. Corredor, T. Dey, R. Morrow, **F. Scaravaggi**, A. U. B. Wolter, S. Aswartham, S. Wurmehl and B. Büchner, *"Interplay of 3d- and 5d-sublattice magnetism in the double perovskite substitution series $La_2Zn_{1-x}Co_xIrO_6$"*, *Phys. Rev. B* **97**, 035155 (2018).

4. C. Wuttke, F. Caglieris, S. Sykora, **F. Scaravaggi**, A. U. B. Wolter, K. Manna, V. Süss, C. Shekhar, C. Felser, B. Büchner and C. Hess, *"Berry curvature unravelled by the anomalous Nernst effect in Mn_3Ge"*, *Phys. Rev. B* **100**, 085111 (2019).

5. A. Zeugner, F. Nietschke, A. U. B. Wolter, S. Gaß, R. C. Vidal, T. R. F. Peixoto, D. Pohl, C. Damm, A. Lubk, R. Hentrich, S. K. Moser, C. Fornari, C. H. Min, S. Schatz, K. Kißner, M. Ünzelmann, M. Kaiser, **F. Scaravaggi**, B. Rellinghaus, K. Nielsch, C. Hess, B. Büchner, F. Reinert, H. Bentmann, O. Oeckler, T. Doert, M. Ruck and A. Isaeva, *"Chemical Aspects of the Candidate Antiferromagnetic Topological Insulator $MnBi_2Te_4$"*, *Chemistry of Materials* **31 (8)**, 2795-2806 (2019).

6. L. Wang, S. Sauerland, **F. Scaravaggi**, R. Kappenberger, S. Aswartham, S. Wurmehl, A. U. B. Wolter, B. Büchner and R. Klingeler, *"Nematicity and structure in $LaFe_{1-x}Co_xAsO$"*, *Journal of Magnetism and Magnetic Materials* **482**, 50 (2019).

7. X. Hong, F. Caglieris, R. Kappenberger, S. Wurmehl, S. Aswartham, **F. Scaravaggi**, P. Lepucki, A. U. B. Wolter, H.-J. Grafe, B. Büchner and C. Hess, *"Evolution of the nematic susceptibility in* $LaFe_{1-x}Co_xAsO$*"*, *Physical Review Letters* **125**, 067001 (2020).

8. S. Selter*, **F. Scaravaggi***, R. Kappenberger, M. Naumann, M. Knupfer, S. Wurmehl, S. Aswartham, A. U. B. Wolter and B. Büchner, *"Structural modifications and electronic correlations in the series* BaT_2As_2 *(T = Cr, Mn, Fe, Co, Ni, Cu) single crystals"*, *Inorganic Chemistry* **59**, 16913–16923 (2020).

9. **F. Scaravaggi**, S. Sauerland, L. Wang, R. Kappenberger, P. Lepucki, A. P. Dioguardi, X. Hong, F. Caglieris, C. Wuttke, C. Hess, H.-J. Grafe, S. Aswartham, S. Wurmehl, R. Klingeler, A. U. B. Wolter and B. Büchner, *"Revisiting the phase diagram of* $LaFe_{1-x}Co_xAsO$ *in single crystals probed by thermodynamic methods"*, *Phys. Rev. B* **103**, 174506 (2021).

10. P. Lepucki, R. Havemann, A. P. Dioguardi, **F. Scaravaggi**, A. U. B. Wolter, R. Kappenberger, S. Aswartham, S. Wurmehl, B. Büchner and H.-J. Grafe, *"Mapping out the spin fluctuations in Co-doped LaFeAsO single crystals"*, *Phys. Rev. B* **103**, L180506 (2021).